Metrology of band topology via resonant inelastic x-ray scattering

Sangjin Lee,[1,2] Kyung-Hwan Jin,[2] Byungmin Kang,[3] B. J. Kim,[4,2,*] and Gil Young Cho[4,2,1,†]

[1]*Asia Pacific Center for Theoretical Physics, Pohang 37673, Republic of Korea*

[2]*Center for Artificial Low Dimensional Electronic Systems, Institute for Basic Science (IBS), Pohang 37673, Republic of Korea*

[3]*School of Physics, Korea Institute for Advanced Study, Seoul 02455, Korea*

[4]*Department of Physics, Pohang University of Science and Technology (POSTECH), Pohang 37673, Republic of Korea*

(Received 30 August 2021; revised 3 April 2022; accepted 10 January 2023; published 20 January 2023)

Topology is a central notion in the classification of band insulators and the characterization of entangled many-body quantum states. In some cases, it manifests as quantized observables such as quantum Hall conductance. However, being inherently a global property depending on the entirety of the system, its direct measurement has remained elusive to local experimental probes in many cases. Here, we demonstrate that various topological band indices can be directly probed by resonant inelastic x-ray scattering. Specifically, we show that the crystalline symmetry eigenvalues at the high-symmetry momentum points, which determine the band topology, lead to distinct scattering intensity for particular momentum and energy. Our approach can be explicitly demonstrated in several examples such as 1D Su-Schrieffer-Heeger chain, 2D quadrupole insulator, 3D topological band insulator, and chiral hinge insulator. Our result establishes an incisive bulk probe for the measurement of band topology.

DOI: 10.1103/PhysRevB.107.045129

I. INTRODUCTION

In condensed matter system, scattering techniques generally measure two-point correlators of physical quantities that determine the transport and dissipation of energy and momentum through collective excitations of constituent nuclei and electrons. In resonant inelastic x-ray scattering (RIXS) [1,2], sensitivity to valence electrons is greatly amplified by resonant processes when the incident x-ray is tuned to the binding energy of a core electron. Besides detection of otherwise vanishingly small signal associated with subtle electronic orders [3,4], RIXS sometimes provides additional valuable information on the electronic wave functions; prominent examples include the detection of pseudospin structure in spin-orbit Mott insulators and the bonding/antibonding nature of quasimolecular [5] orbitals in quantum dimers [6–12]. The method relies on the coherent interference [8] among different intermediate states, whose phase differences encode information beyond that contained in the correlation functions.

In this work, we investigate the possibility of exploiting RIXS for probing the topology of an electronic band structure, which is classified by a topological band index [13–15]. We note that the band topology is difficult to directly access through bulk energy spectrum as two topologically distinct phases can share the same spectrum, but its change can be detected at their interface. Hence, much of the previous experimental efforts focused on detecting the topological boundary modes via, e.g., photoemission spectroscopy [16–20] and tunneling probes [21–26]. However, the topological boundary states are not always easily accessible in experiment, for example, when the topological boundary states are buried deep inside the bulk states. Thus it is desirable to establish a *bulk probe* that can directly diagnose the nontrivial band topology.

To this end, we will show that the band topology manifests in RIXS spectral intensity at high-symmetry momentum. More precisely, we will prove that from the momentum dependence of the RIXS intensity, one can directly infer their crystalline symmetry eigenvalues of the reflection, inversion, and rotational symmetries, which constitute several important topological band indices [27–31]. We will explicitly demonstrate our protocol on a few, most important examples of topological insulators: 1D Su-Schrieffer-Heeger (SSH) chain [32] relevant for $A_2W_6X_6$ (A = Rb, Cs; X = S, Se) [33–36], 3D topological band insulators (TBI) for $Bi_{1-x}Sb_x$ [30,37,38], and also 2,3D higher order topological insulators (HOTI) [27,28,31] with material candidates XY (X = Ge; Y = S, Se) [39].

The organization of this paper is as follow. In Sec. VIII, we briefly review the formalism of (non-spin-flip) RIXS, which will be mainly considered in our paper. In following sections, we present the application of this formalism to the topological band insulators. In Sec. III, we will consider the 1D Su-Schrieffer-Heeger (SSH) model and show that RIXS intensity can indeed be used to diagnose the band topology. In Sec. IV, we generalize this to the prototypical time-reversal symmetric topological band insulators and show that the $\mathbb{Z}_2$ invariant can be read off unambiguously. Finally, we apply our theory to the higher order topological insulators in Secs. V and VII, which are on the RIXS intensity of the 2D quadrupole insulator model, C_4-symmetric higher order topological insulator and a 3D chiral hinge insulator.

*bjkim6@postech.ac.kr

†gilyoungcho@postech.ac.kr

II. BRIEF INTRODUCTION TO RIXS

We first review the formalism for RIXS in the fast collision approximation [1,40–42]. The RIXS spectral intensity is $\mathcal{I}(\boldsymbol{q},\omega)=\sum_f|\mathcal{A}_f(\boldsymbol{q},\omega)|^2\delta(E_f-E_{\rm GS}-\omega)$ with the quantum amplitude

$$\mathcal{A}_f(\boldsymbol{q},\omega)=\langle f|\hat{T}(\boldsymbol{q},\omega)|{\rm GS}\rangle. \tag{1}$$

Here $|{\rm GS}\rangle$ and $|f\rangle$ are the many-electron states (the ground state and an excited, final state) and $\hat{T}(\boldsymbol{q},\omega)$ is the scattering matrix describing the RIXS process.

In the fast collision limit, $\hat{T}(\boldsymbol{q},\omega)$ describes the creation of a local electron-hole pair at each atomic sites [1,40–42]. In this work, we focus on the non-spin-flip RIXS [43] (see Appendix A for a brief review),

$$\hat{T}(\boldsymbol{q},\omega)=\mathcal{C}(\omega)\sum_{\boldsymbol{r},\sigma}c_{\boldsymbol{r},\sigma}c^\dagger_{\boldsymbol{r},\sigma}e^{i\boldsymbol{q}\cdot\boldsymbol{r}}, \tag{2}$$

which can be achieved by appropriately selecting edges (e.g., Bi $2s\to 6p$ transition) or polarizations of photons. Here, $\mathcal{C}(\omega)$ is a constant containing the information of atomic details, e.g., dipole matrix elements, polarization of (incident and outgoing) photons, and lifetime of the intermediate virtual states. $c^\dagger_{\boldsymbol{r},\sigma}$ ($c_{\boldsymbol{r},\sigma}$) is a creation (annihilation) operator of low-energy spin-σ electrons of an atom at $\boldsymbol{r}$. More discussion on $\hat{T}(\boldsymbol{q},\omega)$ is in Appendix A.

Inserting Eq. (2) to Eq. (1), we can recast Eq. (1) in terms of Bloch functions $\psi_{c/v}(\boldsymbol{k})$ (which depend on spin for strongly spin-orbit coupled systems):

$$\mathcal{A}_f(\boldsymbol{q},\omega)=\mathcal{C}(\omega)\,\psi^\dagger_c(\boldsymbol{k}+\boldsymbol{q})\cdot\hat{\mathcal{M}}_{\boldsymbol{k}+\boldsymbol{q},\boldsymbol{k}}\cdot\psi_v(\boldsymbol{k}), \tag{3}$$

where $E_c(\boldsymbol{k}+\boldsymbol{q})-E_v(\boldsymbol{k})=\omega$. Here "$c$" and "$v$" represent the conduction and valence bands. $\hat{\mathcal{M}}_{\boldsymbol{q}+\boldsymbol{k},\boldsymbol{k}}$ contains the information of the sublattice structure. The final expression (3) can be summarized as [Fig. 1(a)], where an electron is pulled from the valence band to the conduction band. The momentum and energy of this excited state is fixed by those of the photons involved in RIXS.

In following sections, we present our central results by applying Eq. (3) to various topological insulators: 1D SSH chain, 3D TBI, and 2,3D HOTI [28,30–32].

III. SSH CHAIN

A. Main result

The SSH model [32] is the simplest reflection-symmetric 1D band insulator, which exhibits a quantized electric polarization. Within each unit cell labeled by $x\in\mathbb{Z}$, there are two sublattices $\alpha=1,2$, at the position $x+d_\alpha$ with $d_\alpha=(-1)^\alpha d$ [Fig. 1(b)]. We assume $d<1/4$ without losing generality, because the dimerization of the SSH model accompanies structural deformation in real materials [33–36], which pushes d away from 1/4. The Hamiltonian is

$$H(k)=-(t_1+t_2\cos k)\sigma^x\otimes s^0-t_2\sin k\sigma^y\otimes s^0. \tag{4}$$

Here, σ^a is the Pauli matrix acting on the sublattice index and s^b is that on the spin index. We set $t_1>0, t_2>0$. The model is spin-rotational symmetric and hence only the identity operator $s^0={\rm Id}_{2\times2}$ appears in Eq. (4). The topological invariant, i.e., polarization $\mathcal{P}$, can be written as [44,45]

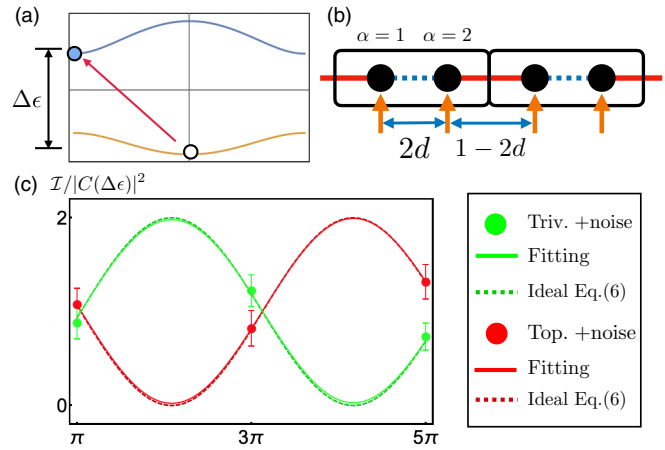

FIG. 1. (a) RIXS process Eq. (3). RIXS induces a transition from the ground state to an excited state with an electron-hole pair. Here, an empty circles represents the hole in the valence band and the filled circle represents the created electron in the conduction band. (b) SSH model. The black box represents a unit cell, which consists of the two sublattices $\{1,2\}$ (black circles). They are physically separated each other by "$2d$" within the unit cell and "$1-2d$" between the unit cell. (c) RIXS intensity of SSH model. Here, the error bars for the data (filled circles) are due to the noise that we included in our simulation.

$$\exp(2\pi i\mathcal{P})=\mathcal{R}_v(\Gamma)\mathcal{R}_v(X), \tag{5}$$

where $\mathcal{R}_v(k)$ is the reflection eigenvalue of the valence band at k. Γ (X) represents $k=0$ ($k=\pi$). The reflection symmetry is $\hat{\mathcal{R}}=\sigma^x$ with $k\to-k$. Many aspects of the model have been well known in literature [28]. Here we only need to know that there are two phases: the nontrivial phase $\mathcal{P}=1/2$ mod 1 for $t_1<t_2$ and the trivial one $\mathcal{P}=0$ mod 1 for $t_1>t_2$.

To grasp $\mathcal{P}$ via RIXS, one would naturally consider the scattering between X and Γ because of Eq. (5), which involves the symmetry data at those momentum points. Indeed, $\mathcal{P}$ directly manifests in the intensity

$$\mathcal{I}[q_n,\Delta\epsilon]=2|\mathcal{C}(\Delta\epsilon)|^2\sin^2(q_nd+\mathcal{P}\pi), \tag{6}$$

where $q_n=(2n+1)\pi, n\in\mathbb{Z}$ is precisely the momentum connecting X and Γ. $\Delta\epsilon$ is the energy difference between the valence band at Γ and the conduction band at X. This fixes the scattering process as [Fig. 1(a)]. Remarkably, the intensity Eq. (6) is largely independent of the hopping parameters of the SSH model [except the overall coefficient $\mathcal{C}(\Delta\epsilon)$]. Even more, its oscillation in momentum is entirely fixed by the topology $\mathcal{P}$. This allows us to apply Eq. (6) irrespective of the detailed parameters of the Hamiltonian.

B. Proof of Eq. (6)

To prove Eq. (6), our starting point is the non-spin-flip RIXS quantum amplitude,

$$\mathcal{A}_f(q)=\mathcal{C}(\omega)\sum_{x\in\mathbb{Z},\alpha,s=\{\uparrow,\downarrow\}}\langle f|c_{x,\alpha,s}c^\dagger_{x,\alpha,s}e^{iqx_\alpha}|{\rm GS}\rangle,$$

where α is the sublattice index, and s is the spin. On this, we plug $c_{x,\alpha,s=\uparrow,\downarrow} = \sum_{k,\eta} U^\dagger_{\alpha\eta}\gamma_{\eta,s}(k)e^{ikx}$ where

$$U^\dagger = [\psi_c(k)|\psi_v(k)] \tag{7}$$

and $\psi_{c,v}(k)$ are the Bloch functions (see Appendix B for the details of notations), to find

$$\mathcal{A}_f(q) = \mathcal{C}(\omega)\sum_{k,s}\langle f|(k)\hat{\mathcal{M}}_{k+q,k}U^\dagger(k+q))_{\nu\mu} \times \gamma_{\mu,s}(k+q)\gamma^\dagger_{\nu,s}(k)|g\rangle. \tag{8}$$

We have introduced a diagonal matrix $\hat{\mathcal{M}}_{k+q,k}$ whose αth component is $e^{-iqd_{\alpha=1,2}}$ [Fig. 1(b)], i.e.,

$$\hat{\mathcal{M}}_{k+q,k} = \begin{pmatrix} e^{iqd} & 0 \\ 0 & e^{-iqd} \end{pmatrix}. \tag{9}$$

Up to the U(1) phase factor, this matrix depends solely on the real space distance between the two sublattices, but not on the Hamiltonians. Note that there is a gauge dependence of $\hat{\mathcal{M}}_{k+q,k}$. $\hat{\mathcal{M}}_{k+q,k}$ depends on our gauge choice of the Bloch functions. For example, the matrix itself is not invariant under the U(1) phase rotation of the Bloch functions. This is because it is not the quantum amplitude $\mathcal{A}_f$ but the spectral intensity $\mathcal{I} \sim |\mathcal{A}_f|^2$, which is actually measured in experiment.

From this, the RIXS intensity is

$$\mathcal{I}(q,\omega) = 2|\mathcal{C}(\omega)|^2 {\sum_f}' |\psi^\dagger_c(k+q)\hat{\mathcal{M}}_{k+q,q}\psi_v(k)|^2.$$

Here $\sum'$ represents a sum over the final states that satisfy the energy-momentum conservation and the factor of 2 comes from the spin degeneracy.

If we further specify the energy and momentum transfer of the RIXS as $\Delta\epsilon{=}\epsilon_c(X){-}\epsilon_v(\Gamma)$ and $q_n{=}(2n{+}1)\pi$ $(n \in \mathbb{Z})$, (see [Fig. 1(a)]), the RIXS amplitude is

$$\mathcal{I}(q_n,\Delta\epsilon) = 2|\mathcal{C}(\Delta\epsilon)|^2|\psi^\dagger_c(X)\hat{\mathcal{M}}_{q_n,0}\psi_v(\Gamma)|^2,$$

where $\hat{\mathcal{M}}_{q_n,0}$ is obtained from Eq. (9).

$$\hat{\mathcal{M}}_{k+q_n,\pi} = \begin{pmatrix} e^{iq_nd} & 0 \\ 0 & e^{-iq_nd} \end{pmatrix} = \cos q_nd + i\sin q_nd\cdot\hat{\Pi}, \tag{10}$$

where $\hat{\Pi}\cdot\hat{\mathcal{M}}_{q_n}\cdot\hat{\Pi} = \hat{\mathcal{M}}_{q_n}$, where $\hat{\Pi} = \sigma^3$ is the chiral symmetry operator. Note that although the chiral symmetry operator appears in the discussion, we do not assume that the Hamiltonians respect the chiral symmetry.

The corresponding RIXS amplitude (per spin) is then

$$\frac{\mathcal{A}_f(q_n,\Delta\epsilon)}{\mathcal{C}(\Delta\epsilon)} = \psi^\dagger_c(X)\psi_v(\Gamma)\cos q_nd + i\psi^\dagger_c(X)\hat{\Pi}\psi_v(\Gamma)\sin q_nd.$$

The corresponding RIXS intensity is

$$\frac{\mathcal{I}_f(q_n,\Delta\epsilon)}{|\mathcal{C}(\Delta\epsilon)|^2} = |\psi^\dagger_c(X)\psi_v(\Gamma)\cos q_nd + i\psi^\dagger_c(X)\hat{\Pi}\psi_v(\Gamma)\sin q_nd|^2.$$

The full RIXS intensity is simply the twice of the above, because of the spin states, i.e., $s = \uparrow, \downarrow$.

Our goal is to show the following two. First,

$$\text{if } \mathcal{P}=0,\ |\psi^\dagger_c(X)\hat{\Pi}\psi_v(\Gamma)|^2 = 1,\ |\psi^\dagger_c(X)\psi_v(\Gamma)|^2 = 0, \tag{11}$$

which trivially implies $\mathcal{I}_f(q_n,\Delta\epsilon) = 2|\mathcal{C}(\Delta\epsilon)|^2\sin^2 q_nd$. Second,

$$\text{if } \mathcal{P}=\tfrac{1}{2},\ |\psi^\dagger_c(X)\hat{\Pi}\psi_v(\Gamma)|^2 = 0,\ |\psi^\dagger_c(X)\psi_v(\Gamma)|^2 = 1, \tag{12}$$

which implies $\mathcal{I}_f(q_n,\Delta\epsilon) = 2|\mathcal{C}(\Delta\epsilon)|^2\cos^2 q_nd$ These two are equivalent to Eq. (6).

To present the proof, we need a few preliminaries. First, we prove $\psi^\dagger_{\eta=c/v}(k_*)\hat{\Pi}\psi_\eta(k_*) = 0$ for $k_* = X, \Gamma$. This can be shown as

$$\begin{aligned}
\psi^\dagger_\eta(k_*)\hat{\Pi}\psi_\eta(k_*) &= \psi^\dagger_\eta(k_*)\hat{\Pi}\hat{\mathcal{R}}^\dagger\hat{\mathcal{R}}\psi_\eta(k_*),\\
&= \mathcal{R}_\eta(k_*)\psi^\dagger_\eta(k_*)\hat{\Pi}\hat{\mathcal{R}}\psi_\eta(k_*),\\
&= -\mathcal{R}_\eta(k_*)\psi^\dagger_\eta(k_*)\hat{\mathcal{R}}\hat{\Pi}\psi_\eta(k_*),\\
&= -\mathcal{R}^2_\eta(k_*)\psi^\dagger_\eta(k_*)\hat{\Pi}\psi_\eta(k_*),\\
&= -\psi^\dagger_\eta(k_*)\hat{\Pi}\psi_\eta(k_*).
\end{aligned}$$

In the third line, we used $\{\hat{\Pi},\hat{\mathcal{R}}\} = 0$. This implies $\psi_{c/v}(k_*) \perp \hat{\Pi}\psi_{c/v}(k_*)$. Note that the above does not require the Hamiltonian to be chiral symmetric. Combining this with the fact that $\{\psi_c(k_*), \psi_v(k_*)\}$ forms an orthonormal basis for the two-dimensional complex plane, we conclude

$$\psi_{c/v}(k_*) \perp \hat{\Pi}\psi_{c/v}(k_*) \Rightarrow \psi_{v/c}(k_*) \parallel \hat{\Pi}\psi_{c/v}(k_*). \tag{13}$$

That is, $\hat{\Pi}\psi_{c/v}(k_*)$ is identical to $\psi_{v/c}(k_*)$ up to a phase. This immediately implies $\mathcal{R}_c(k_*) = -\mathcal{R}_v(k_*)$. This follows from $\psi_c(k_*) = c\hat{\Pi}\psi_v(k_*)$ (with a complex phase factor $|c| = 1$) and $\{\hat{\Pi},\hat{\mathcal{R}}\} = 0$. Another useful fact is that if $|\Psi^\dagger\psi_v(k_*)|^2 = 1$ for a normalized vector Ψ, then $|\Psi^\dagger\hat{\Pi}\psi_v(k_*)|^2 = 0$. This is because $\{\psi_v(k_*), \hat{\Pi}\psi_v(k_*)\}$ is an orthonormal basis for the two-dimensional complex vector space. Similarly, if $|\Psi^\dagger\psi_v(k_*)|^2 = 0$ for a normalized vector Ψ, then $|\Psi^\dagger\hat{\Pi}\psi_v(k_*)|^2 = 1$.

We now prove the first claim that $|\psi^\dagger_c(X)\psi_v(\Gamma)| = 0$ and $|\psi^\dagger_c(X)\hat{\Pi}\psi_v(\Gamma)| = 1$ for $\mathcal{P} = 0$. This is because

$$\begin{aligned}
\psi^\dagger_c(X)\psi_v(\Gamma) &= \psi^\dagger_c(X)\hat{\mathcal{R}}^\dagger\hat{\mathcal{R}}\psi_v(\Gamma),\\
&= \mathcal{R}_v(\Gamma)\mathcal{R}_c(X)\psi^\dagger_c(X)\psi_v(\Gamma),\\
&= -e^{2\pi i\mathcal{P}}\psi^\dagger_c(X)\psi_v(\Gamma).
\end{aligned}$$

where we have used $\mathcal{R}_c(k_*) = -\mathcal{R}_v(k_*)$ since $\{\hat{\mathcal{R}},\hat{\Pi}\} = 0$ and $\mathcal{R}_v(\Gamma)\mathcal{R}_v(X) = \exp(2\pi i\mathcal{P})$. Plugging $\mathcal{P} = 0$, we find $\psi^\dagger_c(X)\psi_v(\Gamma) = 0$. Since $\{\psi_v(\Gamma), \Pi\psi_v(\Gamma)\}$ forms an orthonormal basis, we see $|\psi^\dagger_c(X)\hat{\Pi}\psi_v(\Gamma)| = 1$. This completes the proof Eq. (11).

For the second claim, we show that $\psi^\dagger_c(X)\hat{\Pi}\psi_v(\Gamma) = 0$ for $\mathcal{P} = 1/2$,

$$\begin{aligned}
\psi^\dagger_c(X)\hat{\Pi}\psi_v(\Gamma) &= \psi^\dagger_c(X)\hat{\Pi}\hat{\mathcal{R}}^\dagger\hat{\mathcal{R}}\psi_v(\Gamma)\\
&= -\psi^\dagger_c(X)\hat{\mathcal{R}}^\dagger\hat{\Pi}\hat{\mathcal{R}}\psi_v(\Gamma)\\
&= -\mathcal{R}_v(\Gamma)\mathcal{R}_c(X)\psi^\dagger_c(X)\hat{\Pi}\psi_v(\Gamma)\\
&= \mathcal{R}_v(\Gamma)\mathcal{R}_v(X)\psi^\dagger_c(X)\hat{\Pi}\psi_v(\Gamma)\\
&= e^{2\pi i\mathcal{P}}\psi^\dagger_c(X)\hat{\Pi}\psi_v(\Gamma),
\end{aligned}$$

where we have used sequentially $\{\hat{\mathcal{R}}, \hat{\Pi}\} = 0$, $\mathcal{R}_c(k_*) = -\mathcal{R}_v(k_*)$, and $\mathcal{R}_v(\Gamma)\mathcal{R}_v(X) = \exp(2\pi i\mathcal{P})$. Plugging $\mathcal{P} = 1/2$, we see $\psi_c^\dagger(X)\hat{\Pi}\psi_v(\Gamma) = 0$. Because $\{\psi_v(\Gamma), \Pi\psi_v(\Gamma)\}$ forms an orthonormal basis, we also find $|\psi_c^\dagger(X)\psi_v(\Gamma)|^2 = 1$. This completes our proof for the second one.

Note that in deriving the above, we used only the symmetries. One obvious consequence of this is that the precise positions of the states in energy is not important in obtaining the above formula (6).

C. Numerical simulations

Here, we numerically demonstrate that Eq. (6) indeed allows us to decipher $\mathcal{P}$ from the RIXS intensity. For this, we first numerically generated the RIXS intensity data for both the topological and trivial states of the SSH model (with $d = 0.24$), and we attempted to fit the data with Eq. (6). The data, which are represented as the filled circles in Fig. 1(c), consist of the simulated signals from the clean SSH chain and white noises (added to mimic the experimental situations),

$$\mathcal{I}(q_n, \omega) = \mathcal{I}_0(q_n, \omega) + \delta\mathcal{I}_{\text{random}},$$

where $\mathcal{I}_0(q_n, \omega)$ is the RIXS intensity from the clean system, and $\delta\mathcal{I}_{\text{random}}$ is the random noise. $\delta\mathcal{I}_{\text{random}}$ is drawn from the uniform distribution $[-0.2, 0.2] \times |\mathcal{C}(\Delta\epsilon)|^2$ (which is rather large). Hence, $\mathcal{I}_0(q_n, \omega)$ agrees well with the idealistic, perfect RIXS signal Eq. (6). For the topological case $\mathcal{P} = 1/2$ (red circles), the parameters of the SSH Hamiltonian were $t_1 = 0.1$ and $t_2 = 1$. For the trivial case $\mathcal{P} = 0$, the parameters were $t_1 = 1$ and $t_2 = 0.1$ (so that $\Delta\epsilon$ is the same for the both cases). We set $d = 0.24$ for both the cases.

We attempted to fit these data with $\mathcal{I}(q_n)/|\mathcal{C}(\Delta\epsilon)|^2 = A\sin^2(q_nB + P) + C$, where (A, B, C, P) are the fitting parameters (we have restricted $B \in [0, 1/4]$ without losing the generality). See the solid lines in Fig. 1(c), which are obtained from the fitting. The results excellently agree with the dotted lines, which are the ideal ones Eq. (6). For the ideal, noiseless signal of trivial case (without the noise $\delta\mathcal{I}_{\text{random}}$), we expect to find

$$A = 2, B = 0.24, C = 0, P = 0, \tag{14}$$

which is the dotted green line in Fig. 1(c). As the result of the fitting (the solid green line), we found

$$A = 1.98,\ B = 0.24,\ C = 0.02,\ \text{and } P = 0.00, \tag{15}$$

which are pretty close to the ideal values (14). More importantly, we succesfully diagnose the band topology $\mathcal{P} = P/\pi = 0$. For the ideal, noiseless signal of trivial case (without the noise $\delta\mathcal{I}_{\text{random}}$), we expect to find

$$A = 2,\ B = 0.24,\ C = 0,\ \text{and } P = 1.58, \tag{16}$$

which is the dotted red line in Fig. 1(c). As the result of the fitting (the red solid line), we found

$$A = 1.99,\ B = 0.23,\ C = -0.04,\ \text{and } P = 1.58, \tag{17}$$

which are pretty close to the ideal values (16). More importantly, we succesfully diagnose the band topology $\mathcal{P} = P/\pi = 1/2$.

Our theory can be tested in 3D bulk materials $A_2W_6X_6$ (A = Rb, Cs; X = S, Se), which realize the quasi-1D SSH chains [33–36]. We append their DFT band structures and some information on these materials in Appendix B 4, showing that they indeed have $\mathcal{P} = 1/2$. In these materials, one can use W $2p \to 5d$ transition to perform RIXS experiments to test our theory.

Finally, we remark that the above can be easily generalized to the multiband models, which explicitly lack the chiral symmetry. For example, in Appendix B 3, we consider the four-band model which explicitly breaks the chiral symmetry and demonstrate that we can read off the polarization per each filled band.

IV. 3D TOPOLOGICAL BAND INSULATORS

Our theory is not restricted to 1D and applies equally well to the 3D TBI [30,46]. Some detail of the model can be found in Appendix. E. Here, we focus on showing that the $\mathbb{Z}_2$ topological band index ν_0 [46] can be completely determined from RIXS intensity.

A. Main result

We consider the realistic, four-band model $H_{\text{TBI}}(\boldsymbol{k}) = \sum_{i=0}^{5} d_i(\boldsymbol{k})\Gamma_i$ [30] describing Bi_{1-x} Sb_x [30,37,38]. The specific form of $H_{\text{TBI}}(\boldsymbol{k})$ is not important for now and can be found in Appendix E. The $\mathbb{Z}_2$ index ν_0 is determined by a product of the inversion eigenvalues $I_v(k_*)$ of the valence bands at the time-reversal invariant momentum (TRIM) points k_* [30]

$$(-1)^{\nu_0} = \prod_{\boldsymbol{k}_* \in \text{TRIM}} I_v(\boldsymbol{k}_*).$$

If $\nu_0 = 1$ mod 2, then the insulator is topological with a single surface Dirac cone [46]. Otherwise, it is trivial.

Our key observation here is that the RIXS intensity connecting arbitrary two TRIM points, say $\boldsymbol{k}_*$ and Γ, allows us to determine the product $\mathcal{I}_v(\boldsymbol{k}_*)\mathcal{I}_v(\Gamma)$. This is because $\mathcal{I}_v(\boldsymbol{k}_*)\mathcal{I}_v(\Gamma)$ manifests in the intensity:

$$\mathcal{I}(\boldsymbol{q}_n, \Delta\epsilon_{\boldsymbol{k}_*}) = 2|\mathcal{C}(\Delta\epsilon_{\boldsymbol{k}_*})|^2 \sin^2\left(\boldsymbol{q}_n \cdot \boldsymbol{d} + \tfrac{1}{2}\nu_{k_*}\pi\right), \tag{18}$$

with $\boldsymbol{d} = \frac{1}{8}(1, 1, 1)$ and $\nu_{k_*} = \frac{1}{2}(\mathcal{I}_v(\boldsymbol{k}_*)\mathcal{I}_v(\Gamma) - 1)$. Here, we have tuned the momentum transfer as $\boldsymbol{q}_n = \boldsymbol{k}_* + \sum_{i=1,2,3} n_i\boldsymbol{G}_i$, $n_i \in \mathbb{Z}$ where $\boldsymbol{G}_i$ is a primitive reciprocal vector. The energy transfer $\Delta\epsilon_{\boldsymbol{k}_*}$ is tuned to the energy difference between the valence band at Γ and the conduction band at $\boldsymbol{k}_*$. See Fig. 2(a) for the RIXS process, when $\boldsymbol{k}_* = X$.

B. Proof of Eq. (18)

To prove Eq. (18), we will use the fact that each of conduction and valence bands in the model are twofold degenerate at TRIM points because of the time reversal symmetry, and they have the same inversion eigenvalues. Our starting point is the non-spin-flip RIXS quantum amplitude,

$$\mathcal{A}_f(\boldsymbol{q}) = \mathcal{C}(\omega) \sum_{\boldsymbol{r},\alpha,s=\{\uparrow,\downarrow\}} \langle f|c_{\boldsymbol{r},\alpha,s}c^\dagger_{\boldsymbol{r},\alpha,s}e^{i\boldsymbol{q}\cdot\boldsymbol{r}_\alpha}|g\rangle, \tag{19}$$

where α is the sublattice index, and s is the spin. On this, we plug $c_{\boldsymbol{r},\alpha,s} = \sum_{\boldsymbol{k},\eta} U^\dagger_{\alpha\eta}\gamma_{\eta,s}(\boldsymbol{k})e^{i\boldsymbol{k}\cdot\boldsymbol{x}}$ (see Appendix E for nota-

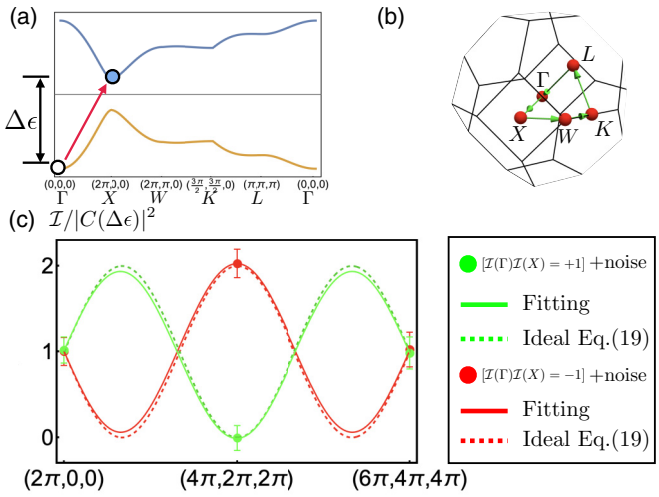

FIG. 2. (a) Band structure of the 3D TBI along a momentum cut [Fig. 2(b)] connecting the high-symmetry points in the diamond lattice. The example in the main text considers the momentum transfer $\boldsymbol{q}_n = X - \Gamma$. This excites a valence electron at Γ to the conduction band at X. (b) Momentum space of the diamond lattice. Here, the arrows represent the momentum cut along which the band structure is obtained in Fig. 2(a). (c) RIXS intensity of 3D TBI for the momentum transfer $\boldsymbol{q}_n = X - \Gamma$. As in the SSH case, the error bars for the data (filled circles) are due to the noise that we included in our simulation.

tions) with

$$U^\dagger = \left[\psi_{c,\mu}(\boldsymbol{k})|\psi_{c,\nu}(\boldsymbol{k})|\psi_{v,\mu}(\boldsymbol{k})|\psi_{v,\nu}(\boldsymbol{k})\right]$$

gives

$$\mathcal{A}_f(\boldsymbol{q}) = \mathcal{C}(\omega)\sum_{k,s}\langle f|(U(\boldsymbol{k})\hat{\mathcal{M}}_{\boldsymbol{k}+\boldsymbol{q},\boldsymbol{k}}U^\dagger \times (\boldsymbol{k}+\boldsymbol{q}))_{\nu\mu}\gamma_{\mu,s}(\boldsymbol{k}+\boldsymbol{q})\gamma^\dagger_{\nu,s}(\boldsymbol{k})|g\rangle, \quad (20)$$

where $\psi_{c/v,\mu}(\boldsymbol{k})$ is an eigenstate of $h_{\rm TBI}(\boldsymbol{k})$ with a degeneracy index $\mu = \pm 1$ (due to the time-reversal symmetry), and $\hat{\mathcal{M}}_{\boldsymbol{q}}$ is

$$\hat{\mathcal{M}}_{\boldsymbol{q}} = \begin{pmatrix} e^{i\boldsymbol{q}\cdot\boldsymbol{d}} & 0 & 0 & 0 \\ 0 & e^{i\boldsymbol{q}\cdot\boldsymbol{d}} & 0 & 0 \\ 0 & 0 & e^{-i\boldsymbol{q}\cdot\boldsymbol{d}} & 0 \\ 0 & 0 & 0 & e^{-i\boldsymbol{q}\cdot\boldsymbol{d}} \end{pmatrix} = \cos(\boldsymbol{q}\cdot\boldsymbol{d})1_{4\times4} + i\sin(\boldsymbol{q}\cdot\boldsymbol{d})\hat{\Pi},$$

with $\boldsymbol{d} = \frac{1}{8}(1,1,1)$. Here $\hat{\Pi}$ can be written as $\Gamma^{12} = [\Gamma^1, \Gamma^2]/2i$. The RIXS quantum amplitude is given by

$$\mathcal{A}_f^{\mu,\nu}(\boldsymbol{q}_n, \Delta\epsilon) = \mathcal{C}(\Delta\epsilon)(\cos(\boldsymbol{q}_n\cdot\boldsymbol{d})\psi^\dagger_{c,\mu}(\boldsymbol{k}+\boldsymbol{q}_n)\psi_{v,\nu}(\boldsymbol{k}) + i\sin(\boldsymbol{q}_n\cdot\boldsymbol{d})\psi^\dagger_{c,\mu}(\boldsymbol{k}+\boldsymbol{q}_n)\hat{\Pi}\psi_{v,\nu}(\boldsymbol{k})). \quad (21)$$

Below, we would like to prove Eq. (18) from Eq. (21) by applying appropriate symmetries. The first step of our proof is to show $\psi^\dagger_{\eta=c/v,\mu}(\boldsymbol{k})\hat{\Pi}\psi_{\eta,\nu}(\boldsymbol{k}) = 0$ where $\boldsymbol{k} \in$ TRIM,

$$\begin{aligned}\psi^\dagger_{\eta,\mu}(\boldsymbol{k})\hat{\Pi}\psi_{\eta,\nu}(\boldsymbol{k}) &= \psi^\dagger_{\eta,\mu}(\boldsymbol{k})\hat{\Pi}\hat{\mathcal{I}}^\dagger\hat{\mathcal{I}}\psi_{\eta,\nu}(\boldsymbol{k}),\\ &= \mathcal{I}_v(\boldsymbol{k})\psi^\dagger_{\eta,\mu}(\boldsymbol{k})\hat{\Pi}\hat{\mathcal{I}}\psi_{\eta,\nu}(\boldsymbol{k}),\\ &= -\mathcal{I}_v(\boldsymbol{k})\psi^\dagger_{\eta,\mu}(\boldsymbol{k})\hat{\mathcal{I}}\hat{\Pi}\psi_{\eta,\nu}(\boldsymbol{k}),\\ &= -\psi^\dagger_{\eta,\mu}(\boldsymbol{k})\hat{\Pi}\psi_{\eta,\nu}(\boldsymbol{k}),\end{aligned}$$

where we used $\{\hat{\mathcal{I}}, \hat{\Pi}\} = 0$. See Appendix E for the detailed algebra. This implies that $\hat{\Pi}\psi_{c/v,\mu}(\boldsymbol{k})$ is orthogonal to $\psi_{c/v,\nu}(\boldsymbol{k})$. Therefore $\hat{\Pi}\psi_{c/v,\mu}(\boldsymbol{k})$ belongs to the space spanned by $\psi_{v/c,\nu}(\boldsymbol{k})$. Similarly, if $\hat{\mathcal{I}}\psi_{v,\mu}(\boldsymbol{k}) = \mathcal{I}_v(\boldsymbol{k})\psi_{v,\mu}(\boldsymbol{k})$, then

$$\begin{aligned}\hat{\Pi}\hat{\mathcal{I}}\psi_{v,\mu}(\boldsymbol{k}) &= \mathcal{I}_v(\boldsymbol{k})\hat{\Pi}\psi_{v,\mu}(\boldsymbol{k}) \Rightarrow \hat{\mathcal{I}}(\hat{\Pi}\psi_{v,\mu}(\boldsymbol{k}))\\ &= -\mathcal{I}_v(\boldsymbol{k})(\hat{\Pi}\psi_{v,\mu}(\boldsymbol{k})),\end{aligned}$$

which means that $\mathcal{I}_c(\boldsymbol{k}) = -\mathcal{I}_v(\boldsymbol{k})$.

To proceed, we choose the convenient orthnormal basis at $\boldsymbol{k}, \boldsymbol{k}+\boldsymbol{q}_n \in$ TRIM as follows:

$$\{\psi_{v,1}(\boldsymbol{k}), \psi_{v,2}(\boldsymbol{k}), \psi_{c,1}(\boldsymbol{k}), \psi_{c,2}(\boldsymbol{k})\},$$

where $\psi_{c,\mu}(\boldsymbol{k}) = \hat{\Pi}\psi_{v,\mu}(\boldsymbol{k})$. Similary, for the reciprocal momentum $\boldsymbol{q}_n$, we define

$$\{\psi_{v,1}(\boldsymbol{k}+\boldsymbol{q}_n), \psi_{v,2}(\boldsymbol{k}+\boldsymbol{q}_n), \psi_{c,1}(\boldsymbol{k}+\boldsymbol{q}_n), \psi_{c,2}(\boldsymbol{k}+\boldsymbol{q}_n)\},$$

such that $\psi^\dagger_{c,\mu}(\boldsymbol{k}+\boldsymbol{q}_n)\psi_{v,\nu\neq\mu}(\boldsymbol{k})=0$ and $\psi^\dagger_{c,\mu}(\boldsymbol{k}+\boldsymbol{q}_n)\psi_{c,\nu\neq\mu}(\boldsymbol{k}) = 0$. *This choice allows us to forget about the degeneracy index* (μ, ν) *because the amplitude is diagonal in this index.* With this, Eq. (21) becomes

$$\mathcal{A}_f^{\mu\nu}(\boldsymbol{q}_n, \Delta\epsilon) = \delta^{\mu\nu}\mathcal{C}(\Delta\epsilon)(\cos(\boldsymbol{q}_n\cdot\boldsymbol{d})\psi^\dagger_{c,\mu}(\boldsymbol{k}+\boldsymbol{q}_n)\psi_{v,\mu}(\boldsymbol{k}) + i\sin(\boldsymbol{q}_n\cdot\boldsymbol{d})\psi^\dagger_{c,\mu}(\boldsymbol{k}+\boldsymbol{q}_n)\hat{\Pi}\psi_{v,\mu}(\boldsymbol{k})). \quad (22)$$

We now look for the symmetry constraints on the terms in (21). For example, we can apply the inversion symmetry

$$\begin{aligned}\psi^\dagger_{c,\mu}(\boldsymbol{k}+\boldsymbol{q}_n)\psi_{v,\mu}(\boldsymbol{k}) &= \psi^\dagger_{c,\mu}(\boldsymbol{k}+\boldsymbol{q}_n)\hat{\mathcal{I}}^\dagger\hat{\mathcal{I}}\psi_{v,\mu}(\boldsymbol{k})\\ &= -\mathcal{I}_v(\boldsymbol{k}+\boldsymbol{q}_n)\mathcal{I}_v(\boldsymbol{k})\psi^\dagger_{c,\mu}(\boldsymbol{k}+\boldsymbol{q}_n)\\ &\quad\times\psi_{v,\mu}(\boldsymbol{k}). \quad (23)\end{aligned}$$

Therefore we find that if $\mathcal{I}_v(\boldsymbol{k}+\boldsymbol{q}_n)\mathcal{I}_v(\boldsymbol{k}) = 1$, then $\psi^\dagger_{c,\mu}(\boldsymbol{k}+\boldsymbol{q}_n)\psi_{v,\mu}(\boldsymbol{k}) = 0$. At the same time, we automatically find $|\psi^\dagger_{c,\mu}(\boldsymbol{k}+\boldsymbol{q}_n)\hat{\Pi}\psi_{v,\mu}(\boldsymbol{k})| = 1$ since $\psi^\dagger_{v,\mu}(\boldsymbol{k})\hat{\Pi}\psi_{v,\mu}(\boldsymbol{k}) = 0$ and $\psi^\dagger_{v,\mu}(\boldsymbol{k}+\boldsymbol{q}_n)\psi_{c/v,\nu\neq\mu}(\boldsymbol{k}) = 0$. Hence, Eq. (22) becomes $\mathcal{A}_f^{\mu\nu}(\boldsymbol{q}_n, \Delta\epsilon) = \delta^{\mu\nu}\mathcal{C}(\Delta\epsilon)i\sin(\boldsymbol{q}_n\cdot\boldsymbol{d})$, which leads to $\mathcal{I} = 2|\mathcal{C}(\Delta\epsilon)|^2\sin^2(\boldsymbol{q}_n\cdot\boldsymbol{d})$.

Similarly, because of

$$\psi^\dagger_{c,\mu}(\boldsymbol{k}+\boldsymbol{q_n})\hat{\Pi}\psi_{v,\mu}(\boldsymbol{k}) = \psi^\dagger_{c,\mu}(\boldsymbol{k}+\boldsymbol{q_n})\hat{\mathcal{I}}^\dagger\hat{\mathcal{I}}\hat{\Pi}\psi_{v,\mu}(\boldsymbol{k}) = \mathcal{I}_v(\boldsymbol{k}+\boldsymbol{q_n})\mathcal{I}_v(\boldsymbol{k})\psi^\dagger_{c,\mu}(\boldsymbol{k}+\boldsymbol{q_n}) \times \hat{\Pi}\psi_{v,\mu}(\boldsymbol{k}), \quad (24)$$

we find that if $\mathcal{I}_v(\boldsymbol{k}+\boldsymbol{q_n})\mathcal{I}_v(\boldsymbol{k}) = -1$, then $\psi^\dagger_{c,\mu}(\boldsymbol{k}+\boldsymbol{q_n})\hat{\Pi}\psi_{v,\mu}(\boldsymbol{k}) = 0$. This enforces $|\psi^\dagger_{c,\mu}(\boldsymbol{k}+\boldsymbol{q_n})\psi_{v,\mu}(\boldsymbol{k})| = 1$. Hence, Eq. (22) becomes $\mathcal{A}^{\mu\nu}_f(\boldsymbol{q}_n, \Delta\epsilon) = \delta^{\mu\nu}\mathcal{C}(\Delta\epsilon)\cos(\boldsymbol{q}_n\cdot\boldsymbol{d})$, which leads to $\mathcal{I} = 2|\mathcal{C}(\Delta\epsilon)|^2\cos^2(\boldsymbol{q}_n\cdot\boldsymbol{d})$. This completes our proof.

We note that the intensity (18) is largely independent of the hopping parameters of the model [except the overall coefficient $\mathcal{C}(\Delta\epsilon)$]. Moreover, its oscillation in momentum is fixed solely by $\mathcal{I}_v(\boldsymbol{k}_*)\mathcal{I}_v(\Gamma)$. We will see later that this allows us to deduce $\mathcal{I}_v(\boldsymbol{k}_*)\mathcal{I}_v(\Gamma)$ from the intensity. Hence, if we repeat the RIXS experiment on all the TRIM $\boldsymbol{k}_*$, we can derive $\mathcal{I}_v(\boldsymbol{k}_*)\mathcal{I}_v(\Gamma)$ for all the $\boldsymbol{k}_*$. This allows us to determine ν_0 because

$$(-1)^{\nu_0} = \prod_{\boldsymbol{k}_*\neq\Gamma}[\mathcal{I}_v(\boldsymbol{k}_*)\mathcal{I}_v(\Gamma)]. \quad (25)$$

C. Numerical simulations

Next, we explicitly demonstrate the utility of Eq. (18) in determining the topology. For this, we remind that to correctly infer the band topology of $H_{\rm TBI}(\boldsymbol{k})$, the inversion eigenvalue at $\boldsymbol{k}_* = X$, i.e., $\mathcal{I}_v(X)$, needs to be carefully determined. (There are three symmetrically-equivalent X's [Fig. 2(b)], but we will take one below.) This is because the band inversion occurs at $\boldsymbol{k}_* = X$, which controls the phase transition between $\nu_0 = 0$ and 1 [30,46]. Hence, below we will focus on $\boldsymbol{k}_* = X$ [Fig. 2(a)] and demonstrate that we can deduce $\mathcal{I}_v(X)\mathcal{I}_v(\Gamma)$ via Eq. (18) from the RIXS intensity.

We first numerically generate the RIXS intensity data,

$$\mathcal{I}(\boldsymbol{q}_n, \Delta\epsilon) = \mathcal{I}_0(\boldsymbol{q}_n, \Delta\epsilon) + \delta\mathcal{I}_{\rm random}, \quad (26)$$

where $\mathcal{I}_0(\boldsymbol{q}_n, \Delta\epsilon)$ the ideal RIXS intensity [Eq. (18)] and $\delta\mathcal{I}_{\rm random}$ is the random noise. $\delta\mathcal{I}_{\rm random}$ is drawn from the uniform distribution $[-0.3, 0.3]\times|\mathcal{C}(\Delta\epsilon)|^2$. The parameters in $H_{\rm TBI}(\boldsymbol{k})$ allow us to access both the cases $\mathcal{I}_v(X)\mathcal{I}_v(\Gamma) = \pm 1$. The RIXS intensity data of these two cases are represented as the filled circles in Fig. 2(c). Green (red) circles represent the data of the system with $\mathcal{I}_v(X)\mathcal{I}_v(\Gamma) = 1$ ($\mathcal{I}_v(X)\mathcal{I}_v(\Gamma) = -1$). As in the SSH chain, we have included white noises to the data to mimic the experimental situations.

Next, we attempted to fit these simulated data with $\mathcal{I}(\boldsymbol{q}_n, \Delta\epsilon)/|\mathcal{C}(\Delta\epsilon_{\boldsymbol{k}_*})|^2 = A\sin^2(\boldsymbol{q}_n\cdot\boldsymbol{d}+B)+C$, where (A, B, C) are the fitting parameters. The solid lines in Fig. 2(c) are the results of the fitting. They agree well with the dotted lines, which are the ideal ones Eq. (18). These dotted lines exactly agree with the simulated data when the noise is removed, and the small discrepancy between the ideal ones (dotted lines) and the fitting (solid lines) is due to the white noise. In particular, we found that the fitted parameter B correctly determines $\mathcal{I}_v(X)\mathcal{I}_v(\Gamma)$.

The RIXS intensity data [the filled circles in Fig. 2(c)] with momentum transfer $\boldsymbol{q}_n = (2\pi, 0, 0) + n(2\pi, 2\pi, 2\pi)$ [which connects $\Gamma \to X(2\pi, 0, 0)$] are generated by adding the two contributions (26). Red circles correspond to the $\mathcal{I}_v(\Gamma)\mathcal{I}_v(X) = -1$ case and green circles correspond to the $\mathcal{I}_v(\Gamma)\mathcal{I}_v(X) = 1$ case. Note that in the fitting form, $\mathcal{I}(\boldsymbol{q}_n, \Delta\epsilon)/|\mathcal{C}(\Delta\epsilon)|^2 = A\sin^2(\boldsymbol{q}_n\cdot\boldsymbol{d}+B)+C$, B is the diagnostics of the band topology, because we expect $B = \frac{1}{4}(\mathcal{I}_v(\boldsymbol{q}_n)\mathcal{I}_v(\boldsymbol{k}) - 1)\pi$ if the fitting works well enough.

For the ideal, clean signal of $\mathcal{I}_v(\Gamma)\mathcal{I}_v(X) = 1$ case (without the noise $\delta\mathcal{I}_{\rm random}$), we expect to find

$$A = 2.00,\ B = 0.00,\ \text{and}\ C = 0.00, \quad (27)$$

which is the dotted green line in Fig. 2(c). As the result of the fitting [the solid green line in Fig. 2(c)], we found

$$A = 1.96,\ B = 0.01,\ \text{and}\ C = 0.00, \quad (28)$$

which agrees excellently with the exact values Eq. (27). In particular, from B, we can correctly infer $\mathcal{I}_v(\boldsymbol{q}_n)\mathcal{I}_v(\boldsymbol{k}) = 4B/\pi + 1 \approx 1$.

For the perfect, ideal signal of $\mathcal{I}_v(\Gamma)\mathcal{I}_v(X) = -1$ case (without the noise $\delta\mathcal{I}_{\rm random}$), we expect to find

$$A = 2.00,\ B = 1.58,\ \text{and}\ C = 0.00, \quad (29)$$

which is the dotted red line in Fig. 2(c). As the result of the fitting (the solid red line in Fig. 2(c)], we found

$$A = 1.96,\ B = 1.58,\ \text{and}\ C = 0.00, \quad (30)$$

which are pretty close to the exact result (29). In particular, from $B \approx \pi/2$, we can correctly infer $\mathcal{I}_v(\boldsymbol{q}_n)\mathcal{I}_v(\boldsymbol{k}) \approx -1$. Hence, we conclude that we can successfully diagnose $\mathcal{I}_v(X)\mathcal{I}_v(\Gamma)$ via RIXS. Here, although we have focused only on X points, the procedure can be repeated for all the TRIM points. This will determine all the $\mathcal{I}_v(\boldsymbol{k}_*)\mathcal{I}_v(\Gamma)$ for any TRIM $\boldsymbol{k}_*$ and thus ν_0 via Eq. (25). In real experiments, we note that our theory can be tested in RIXS experiments on the standard topological insulator $Bi_{1-x}Sb_x$, where Bi $2s \to 6p$ transition can be used.

This is not restricted to the prototypical four-band model. For example, in Appendix E 3, we have considered eight-band model and shown that we can easily read off the band topology in this case, too.

V. 2D QUADRUPOLAR INSULATORS

We will apply our theory to the higher order topological insulators, i.e., quadrupole insulator (QI) [27,28], which is defined on the square lattice. Some details on the model can be found in Appendix C.

A. Main result

The QI is a C_4-symmetric, four-band insulator, which can support the quantized quadrupolar moment $\mathcal{Q}_{xy}$ mod 1 [27,28]. When C_4 symmetry is imposed, $\mathcal{Q}_{xy}$ can take only the discrete values, either $\mathcal{Q}_{xy} = 1/2$ (topological) or $\mathcal{Q}_{xy} = 0$ (trivial). This quadrupole moment can be related with the C_4-symmetry eigenvalues of valence bands at Γ and $M = (\pi, \pi)$ [27,28]

$$\exp(2\pi i\mathcal{Q}_{xy}) = r_4(M)r_4^*(\Gamma), \quad (31)$$

where $r_4(\boldsymbol{k}_*)$ represents the eigenvalue of the C_4 symmetry at the C_4-symmetric $\boldsymbol{k}_*$ such that $(r_4(\boldsymbol{k}))^2 = i$.

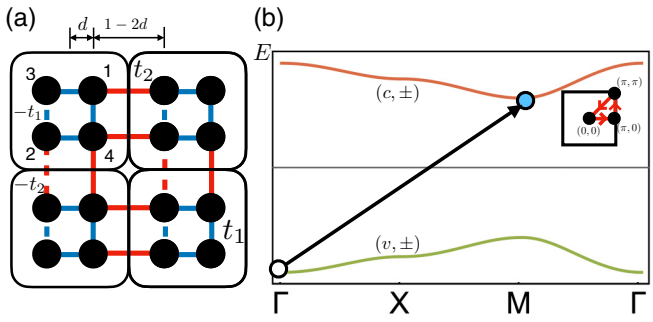

FIG. 3. (a) Hopping pattern of QI model. $t_2(t_1)$ is the intersite(intrasite) hopping parameter and dotted lines represents different sign of hopping parameter (so that there are π flux for all the plaquettes). We present intersite(intrasite) hopping as a red (blue) line. When $t_2 > t_1$, $H_{\rm QI}$ hosts a topologically nontrivial phase. Otherwise, it is trivial. (b) Along the high-symmetry points, we plot the band structure of $H_{\rm QI}$. Each bands are twofold degenerate (degeneracy index $\pm$). At the half filling, $H_{\rm QI}$ is an insulator. We consider the RIXS transition from $\Gamma \to M$. An empty circle represents the hole in the valence band and the filled circles presents the created electron.

From Eq. (31), we are naturally led to consider the RIXS intensity between Γ and M to grasp $\mathcal{Q}_{xy}$. Indeed, we find that the intensity depends on $\mathcal{Q}_{xy}$

$$I[\boldsymbol{q}_n, \Delta\epsilon] = 4|\mathcal{C}(\Delta\epsilon)|^2 \sin^2[(2n+1)\pi d + \mathcal{Q}_{xy}\pi], \quad (32)$$

with $\boldsymbol{q}_n = (2n+1)(\pi,\pi)$, $n \in \mathbb{Z}$. Here, "d" is the half of the real-space distance (in unit of the lattice constant) between the sublattices within a unit cell [Fig. 3(a)]. Thus the topological index $\mathcal{Q}_{xy}$ can be deduced from the RIXS intensity.

B. Proof of Eq. (32)

As in the previous cases, our starting point is the Bloch state $c_{\boldsymbol{r},\alpha,s=\uparrow,\downarrow} = \sum_{\boldsymbol{k},\eta} U^\dagger_{\alpha\eta}\gamma_{\eta,s}(\boldsymbol{k})e^{i\mathbf{k}\cdot\mathbf{r}_\alpha}$ (see Appendix C for notations), which we insert into the formula for the non-spin-flip RIXS quantum amplitude,

$$\mathcal{A}_{fi}(\boldsymbol{q},\omega) = \mathcal{C}(\omega)\sum_{\boldsymbol{k},s}\langle f|(U(\boldsymbol{k})\hat{\mathcal{M}}_{\boldsymbol{k}+\boldsymbol{q},\boldsymbol{k}}U^\dagger \times (\boldsymbol{k}+\boldsymbol{q}))_{\nu\mu}\gamma_{\mu,s}(\boldsymbol{k}+\boldsymbol{q})\gamma^\dagger_{\nu,s}(\boldsymbol{k})|g\rangle,$$

TABLE I. C_4 eigenvalues at symmetric points. We denote a C_4 eigenvalue of a band($\eta = c, v$). Here, ($\xi = \pm$) represents the index for the degenerate states at $\boldsymbol{k}^* = \Gamma, M$ as $r^{\xi=\pm}_{4,\eta=c,v}(\boldsymbol{k}^*)$. When $|t_2| > |t_1|$, $\mathcal{Q}_{xy} = 1/2$ mod 1 and otherwise 0 mod 1.

Bands	$\Gamma(\boldsymbol{q}=(0,0))$	$M(\boldsymbol{q}=(\pi,\pi))$
$(v,-)$	$\mathrm{sign}(t_1+t_2)e^{-i\frac{3}{4}\pi}$	$\mathrm{sign}(t_1+t_2)e^{2\pi i\mathcal{Q}_{xy}}e^{-i\frac{3}{4}\pi}$
$(v,+)$	$\mathrm{sign}(t_1+t_2)e^{+i\frac{3}{4}\pi}$	$\mathrm{sign}(t_1+t_2)e^{2\pi i\mathcal{Q}_{xy}}e^{+i\frac{3}{4}\pi}$
$(c,-)$	$-\mathrm{sign}(t_1+t_2)e^{-i\frac{3}{4}\pi}$	$-\mathrm{sign}(t_1+t_2)e^{2\pi i\mathcal{Q}_{xy}}e^{-i\frac{3}{4}\pi}$
$(c,+)$	$-\mathrm{sign}(t_1+t_2)e^{+i\frac{3}{4}\pi}$	$-\mathrm{sign}(t_1+t_2)e^{2\pi i\mathcal{Q}_{xy}}e^{+i\frac{3}{4}\pi}$

where

$$\hat{\mathcal{M}}_{\boldsymbol{k}+\boldsymbol{q},\boldsymbol{k}} = \begin{pmatrix} e^{i(q_x+q_y)d} & 0 & 0 & 0 \\ 0 & e^{-i(q_x+q_y)d} & 0 & 0 \\ 0 & 0 & e^{i(-q_x+q_y)d} & 0 \\ 0 & 0 & 0 & e^{i(q_x-q_y)d} \end{pmatrix}.$$

The corresponding RIXS intensity of the QI model is

$$\mathcal{I}(\boldsymbol{q},\Delta\epsilon) = 2|\mathcal{C}(\Delta\epsilon)|^2 \sum_f{}' |\psi^\dagger_c(\boldsymbol{k}+\boldsymbol{q})\hat{\mathcal{M}}_{\boldsymbol{k}+q,q}\psi_v(\boldsymbol{k})|^2,$$

where factor 2 came from the double degeneracy of the spin. Here, we consider $\boldsymbol{q}_n = (2n+1)(\pi,\pi)$, $n \in \mathbb{Z}$, and $\Delta\epsilon = \epsilon_c(M) - \epsilon_v(\Gamma)$. This fixes the RIXS channel as $\Gamma \to M$

$$\mathcal{I}(\boldsymbol{q}_n,\Delta\epsilon) = 2|\mathcal{C}(\Delta\epsilon)|^2 \sum_{\eta,\eta'=\pm} |\psi^\dagger_{c,\eta}(M)\hat{\mathcal{M}}_{\mathbf{0}+\boldsymbol{q}_n,\mathbf{0}}\psi_{v,\eta'}(\Gamma)|^2.$$

To proceed, we note that $\psi_{\xi=c/v,\eta}(\boldsymbol{k}^* = \Gamma, M)$ is an eigenstate of C_4 rotation with the eigenvalue $r^\xi_{4,\eta}(\boldsymbol{k}^*)$. This in fact fixes the wave function up to a complex phase factor:

$$\psi^T_{\xi,\eta}(\boldsymbol{k}^*) = \tfrac{1}{2}\big(1, -r^\xi_{4,\eta}(\boldsymbol{k}^*)^2, r^\xi_{4,\eta}(\boldsymbol{k}^*), -r^\xi_{4,\eta}(\boldsymbol{k}^*)^3\big), \quad (33)$$

where $r^\xi_{4,\eta}(\boldsymbol{k}^*)$ is a C_4 eigenvalue of the wavefunction at $\boldsymbol{k}^* = \Gamma, M$. See Table I, for example. We insert this into $\mathcal{I}(\boldsymbol{q}_n,\Delta\epsilon)$ to finally find

$$\mathcal{I}(\boldsymbol{q}_n,\Delta\epsilon) = |\mathcal{C}(\Delta\epsilon)|^2 \times \{|(\cos 2(2n+1)\pi d - e^{2\pi i\mathcal{Q}_{xy}})|^2 + \sin^2(2(2n+1)\pi d)\},$$

$$= 4|\mathcal{C}(\Delta\epsilon)|^2 \sin^2(((2n+1)d + \mathcal{Q}_{xy})\pi) = \begin{cases} 4|\mathcal{C}(\Delta\epsilon)|^2 \sin^2(2n+1)\pi d & \text{for } |t_1| > |t_2| \ (\mathcal{Q}_{xy} = 0), \\ 4|\mathcal{C}(\Delta\epsilon)|^2 \cos^2(2n+1)\pi d & \text{for } |t_1| < |t_2| \ \left(\mathcal{Q}_{xy} = \frac{1}{2}\right). \end{cases} \quad (34)$$

C. Numerical simulations

As in previous examples, we simulated RIXS intensity data. The RIXS intensity data with momentum transfer $\boldsymbol{q}_n = (2n+1)(\pi,\pi)$ are generated by adding the two contributions (Fig. 4):

$$\mathcal{I}(\boldsymbol{q}_n,\Delta\epsilon) = \mathcal{I}_0(\boldsymbol{q}_n,\Delta\epsilon) + \delta\mathcal{I}_{\rm random}, \quad (35)$$

where $\mathcal{I}_0(\boldsymbol{q}_n,\Delta\epsilon)$ is the RIXS intensity obtained by applying Eq. (34), and $\delta\mathcal{I}_{\rm random}$ is the random noise. $\delta\mathcal{I}_{\rm random}$ is drawn from the uniform distribution $[-0.5, 0.5] \times |\mathcal{C}(\Delta\epsilon)|^2$. Hence, $\mathcal{I}_0(\boldsymbol{q}_n,\Delta\epsilon)$ is the analytic, perfect RIXS signal on the clean QI model. For the topological case $\mathcal{Q}_{xy} = 1/2$ (red circles), the parameters of the QI model were $t_1 = 0.1$ and $t_2 = 1$. For the trivial case $\mathcal{Q}_{xy} = 0$, the parameters were $t_1 = 1$ and $t_2 = 0.1$ (so that $\Delta\epsilon$ is the same for the both cases). We set $d = 0.24$

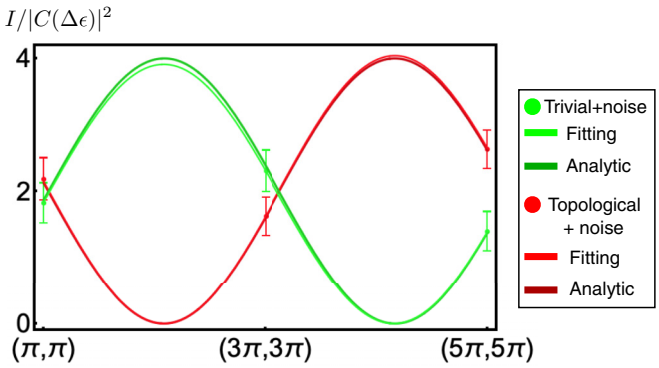

FIG. 4. RIXS intensity of QI model for the momentum transfer $\boldsymbol{q}_n = (2n+1)(\pi,\pi)$ and fitting. As in the previous examples, the error bars for the data (filled circles) are due to the noise that we included in our simulation.

for both the cases [47]. The error bars are due to the noises $\delta\mathcal{I}_{\text{random}}$ that we included.

We have attempted to fit the data with $\mathcal{I}(\boldsymbol{q}_n,\Delta\epsilon)/|C(\Delta\epsilon)|^2 = A\sin^2((2n+1)\pi B+Q)+C$, [cf. Eq. (34)]. Note that the topological index $\mathcal{Q}_{xy}$ is given as Q/π. See the result of the fitting in Fig. 4.

For the ideal, noiseless signal of the trivial case (without the noise $\delta\mathcal{I}_{\text{random}}$), we expect to find

$$A=4,\ B=0.24,\ C=0,\ \text{and}\ Q=0, \tag{36}$$

which is the darker green line in Fig. 4. As the result of the fitting (the light green line in Fig. 4), we found

$$A=3.89,\ B=0.23,\ C=0.04,\ \text{and}\ Q=0.00, \tag{37}$$

which are pretty close to the ideal values (36). In particular, the fitting gives us the correct quadrupole moment $\mathcal{Q}_{xy} = Q/\pi = 0$.

For the ideal, noiseless signal of the topological case (without the noise $\delta\mathcal{I}_{\text{random}}$), we expect to find

$$A=4,\ B=0.24,\ C=0,\ \text{and}\ Q=1.58, \tag{38}$$

which is the darker red line in Fig. 4. As the result of the fitting (the light red line in Fig. 4), we found

$$A=3.99,\ B=0.24,\ C=0.03,\ \text{and}\ Q=1.56, \tag{39}$$

which are pretty close to the ideal values (38). In particular, the fitting results in the almost correct quadrupole moment $\mathcal{Q}_{xy} = Q/\pi \approx 0.49$. If one remembers that the quadrupole moment should be quantized, one can confidently infer $\mathcal{Q}_{xy} = 1/2$ from the fitting.

This can be tested in candidate materials for QI such as XY (X = Ge; Y = S, Se) [39] where Ge $1s \to 4p$ transition is available for the RIXS experiment. In Appendix C, we generalize the above to another class of nondegenerate multiband C_4-symmetric insulator $H^{(4)}_{1b}$ of Refs. [28,48].

VI. 2D C_4 SYMMETRIC HOTI

A. Main result

We also apply our RIXS intensity to another C_4-symmetric higher order insulator $H^{(4)}_{1b}$ [48]. Its topological invariant $\mathcal{C}$ mod 1 is equal to either 1/2 (topological) or 0 (trivial) which can be determined by the relative C_4 rotation eigenvalues at Γ and M,

$$\exp(2\pi i\mathcal{C}) = r_4(M)r_4^*(\Gamma)$$

with $r_4(\boldsymbol{k}_{\in\{\Gamma,M\}})^4 = 1$. Details of $H^{(4)}_{1b}$ can be found in Appendix D such as its symmetry and topology.

As in the QI case, we find RIXS intensity connecting Γ and M encodes the information of topological invariant,

$$\mathcal{I}[\boldsymbol{q}_n,\Delta\epsilon] = 2|\mathcal{C}(\Delta\epsilon)|^2\sin^4[((2n+1)d+\mathcal{C})\pi], \tag{40}$$

with $\boldsymbol{q}_n = (2n+1)(\pi,\pi) = M-\Gamma$ ($n\in\mathbb{Z}$), and $2d$ is the distance between sublattices in the unit cell [Fig. 5(a)]. The overall factor 2 came from the spin degeneracy. We are going to prove that from RIXS intensity $\mathcal{C}$ can be read off by proving Eq. (40).

B. Proof of Eq. (40)

We prove the RIXS intensity of 2D C_4 symmetric higher order topological insulator Eq. (40) for diagnosing the band topology. Essential process of the proof is parallel to QI model. The RIXS quantum amplitude is written as

$$\mathcal{A}_{fi}(\boldsymbol{q}_n,\Delta\epsilon) = \mathcal{C}(\Delta\epsilon)\sum_{s=\{\uparrow,\downarrow\}}\psi^*_{c,1,s}(M)\hat{\mathcal{M}}_{\boldsymbol{0}+\boldsymbol{q}_n,\boldsymbol{0}}\psi_{v,1,s}(\Gamma),$$

with

$$\hat{\mathcal{M}}_{\boldsymbol{k}+\boldsymbol{q},\boldsymbol{k}} = \begin{pmatrix} e^{i(q_x+q_y)d} & 0 & 0 & 0\\ 0 & e^{-i(q_x+q_y)d} & 0 & 0\\ 0 & 0 & e^{i(-q_x+q_y)d} & 0\\ 0 & 0 & 0 & e^{i(q_x-q_y)d}\end{pmatrix}.$$

Therefore the RIXS intensity of the C_4 symmetric higher order topological insulator is

$$\mathcal{I}(\boldsymbol{q}_n,\Delta\epsilon) = 2|\mathcal{C}(\Delta\epsilon)|^2|\psi^\dagger_{c,1}(M)\hat{\mathcal{M}}_{0+\boldsymbol{q}_n,0}\psi_{v,1}(\Gamma)|^2, \tag{41}$$

where the overall factor 2 comes from spin degrees of freedom. Following the same calculation of QI model, the wave functions at the high symmetric points $\boldsymbol{k}_* = \Gamma, M$ are fixed by the C_4 symmetry (up to a complex phase), which gives

$$\psi_{c/v,1}(\boldsymbol{k}_*=\Gamma,M) \propto \tfrac{1}{2}\big(1, r^2_{4,c/v}(\boldsymbol{k}_*), r_{4,c/v}(\boldsymbol{k}_*), r^3_{4,c/v}(\boldsymbol{k}_*)\big),$$

TABLE II. C_4 eigenvalue tables at high symmetric points. We summarize rotation eigenvalues of $(c/v,1)$ bands which is relevant band in the quarter filling. See the band dispersion [Fig. 5(b)]. When $|t_1|>|t_2|$, $\mathcal{C}=0$ which is the trivial phase. When $|t_1|<|t_2|$, $\mathcal{C}=\frac{1}{2}$ and $H^{(4)}_{1b}$ is in the topological phase.

C_4	$\Gamma(\boldsymbol{q}=(0,0))$	$M(\boldsymbol{q}=(\pi,\pi))$
v	$\text{sign}(t_1+t_2)$	$\text{sign}(t_1+t_2)\,e^{2\pi i\mathcal{C}}$
c	$-\text{sign}(t_1+t_2)$	$-\text{sign}(t_1+t_2)\,e^{2\pi i\mathcal{C}}$

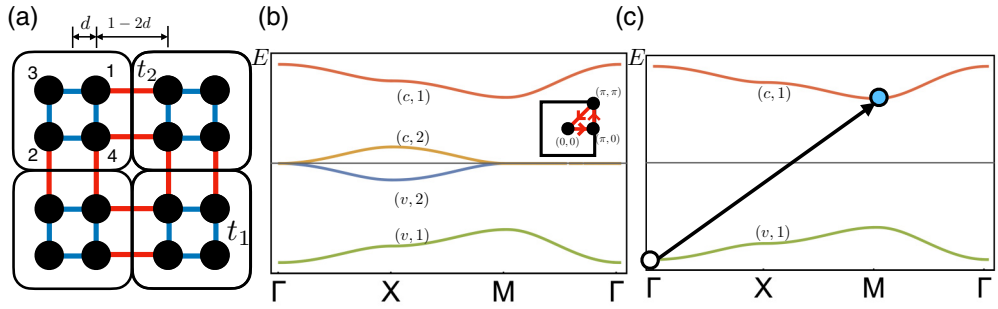

FIG. 5. (a) Hopping pattern of $H^{(4)}_{1b}$ model. $t_2(t_1)$ is the intersite(intrasite) hopping parameter. We present intersite(intrasite) hopping as a red(blue) line. When $t_2 > t_1$, $H^{(4)}_{1b}$ hosts a topological phase. Otherwise, it is trivial. (b) Along the high-symmetry points, we plot the band structure of $H^{(4)}_{1b}$. At the quarter filling, $H^{(4)}_{1b}$ is an insulator. (c) RIXS process. We consider the RIXS transition from $\Gamma \to M$. An empty circle represents the hole in the valence band and the filled circles presents the created electron.

where $r^4_{4,c/v}(\boldsymbol{k}_*) = 1$. Inserting them into the RIXS quantum amplitude with the C_4 eigenvalues in Table II, we obtain

$$\begin{aligned}\mathcal{I}(\boldsymbol{q}_n, \Delta\epsilon) &= \tfrac{1}{2}|\mathcal{C}(\Delta\epsilon)|^2|\cos 2(2n+1)\pi d - e^{2\pi i\mathcal{C}}|^2,\\ &= 2|\mathcal{C}(\Delta\epsilon)|^2 \sin^4(((2n+1)d+\mathcal{C})\pi)\\ &= \begin{cases} 2|\mathcal{C}(\Delta\epsilon)|^2 \sin^4(2n+1)\pi d & \text{for } |t_2| > |t_1| \ (\mathcal{C}=0),\\ 2|\mathcal{C}(\Delta\epsilon)|^2 \cos^4(2n+1)\pi d & \text{for } |t_2| < |t_1| \ \left(\mathcal{C}=\tfrac{1}{2}\right).\end{cases}\end{aligned} \tag{42}$$

C. Numerical simulation

The RIXS intensity data (Fig. 6) with momentum transfer $\boldsymbol{q}_n = (2n+1)(\pi,\pi)$ are generated by adding the two contributions:

$$\mathcal{I}(\boldsymbol{q}_n, \omega) = \mathcal{I}_0(\boldsymbol{q}_n, \omega) + \delta\mathcal{I}_{\text{random}}, \tag{43}$$

where $\mathcal{I}_0(\boldsymbol{q}_n, \omega)$ is the RIXS intensity from the insulator, and $\delta\mathcal{I}_{\text{random}}$ is the random noise. Essentially, $\mathcal{I}_0(\boldsymbol{q}_n, \omega)$ is the analytic, perfect RIXS signal on the clean $H^{(1)}_{4b}$ model. On the other hand, $\delta\mathcal{I}_{\text{random}}$ is the white noise drawn from the uniform distribution $[-0.3, 0.3] \times |\mathcal{C}(\Delta\epsilon)|^2$. For the topological case $\mathcal{C} = 1/2$ (red circles in Fig. 6), the parameters of the $H^{(1)}_{4b}$ model were $t_1 = 0.1$ and $t_2 = 1$. For the trivial case $\mathcal{C} = 0$ (green circles in Fig. 6), the parameters were $t_1 = 1$ and $t_2 = 0.1$ (so that $\Delta\epsilon$ is the same for the both cases). We set $d = 0.24$ for both the cases.

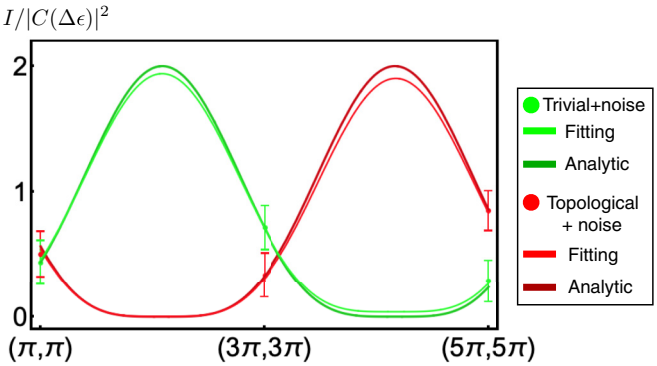

FIG. 6. RIXS intensity of $H^{(4)}_{1b}$ model with momentum transfer $\boldsymbol{q}_n = (2n+1)(\pi,\pi)$ and energy transfer $\omega = \Delta\epsilon = \epsilon_{c,1}(M) - \epsilon_{v,1}(\Gamma)$. See the band dispersion [Fig. 5(b)].

As before, we have attempted to fit the data with $\mathcal{I}(\boldsymbol{q}_n)/|C(\Delta\epsilon)|^2 = A\sin^4((2n+1)\pi B + Q) + C$ [cf. Eq. (40)]. Here Q will be the diagnostics of the band topology, i.e., $\mathcal{C} = Q/\pi$ is the band index.

For the idealistic, perfect signal of the trivial case (without the noise $\delta\mathcal{I}_{\text{random}}$), we expect to find

$$A = 2,\ B = 0.24,\ C = 0,\ \text{and } Q = 0, \tag{44}$$

which is the darker green line in Fig. 6. As the result of the fitting (the light green line in Fig. 6), we found

$$A = 1.90,\ B = 0.23,\ C = 0.04,\ \text{and } Q = 0.00, \tag{45}$$

which are pretty close to the exact values (44). In particular, this correctly determines $\mathcal{C} = Q/\pi = 0.00$.

For the idealistic, perfect signal of topological case (without the noise $\delta\mathcal{I}_{\text{random}}$), we expect to find

$$A = 2,\ B = 0.24,\ C = 0,\ \text{and } Q = 1.58, \tag{46}$$

which is the darker red line in Fig. 6.

As the result of the fitting (the lighter red line in Fig. 6), we found

$$A = 1.90,\ B = 0.23,\ C = 0.00,\ \text{and } Q = 1.57, \tag{47}$$

which are pretty close to the exact values (46). In particular, this correctly determines $\mathcal{C} = Q/\pi = 0.5$.

VII. 3D CHIRAL HINGE INSULATORS

A. Main result

The above discussions can be generalized to 3D CHI [31] (see Appendix F for a review), which hosts a chiral 1D mode at the hinges. The insulator is classified by another $\mathbb{Z}_2$ topological band index $\nu' \in \{0, 1\}$, which can be determined by

the inversion eigenvalues $\mathcal{I}(\boldsymbol{k}_*)$ at $C_{4z}\mathcal{I}$-symmetric points $\boldsymbol{k}_*$, or rotoinversion symmetric points (RISP)

$$(-1)^{\nu'} = \prod_{C_{4z}\mathcal{I}\cdot\boldsymbol{k}_*=\boldsymbol{k}_*} \mathcal{I}(\boldsymbol{k}_*).$$

Similar to the 3D TBI, this $\mathbb{Z}_2$ index for the CHI can be reformulated in terms of the product of $\mathcal{I}(\boldsymbol{k}_*)$ between the two high-symmetric points, e.g., $\mathcal{I}(\boldsymbol{k}_*)\mathcal{I}(\Gamma)$ Hence, the topology of the CHI can be diagnosed in the exactly same fashion as we did for the 3D TBI.

As in the 3D TBI case, we consider the RIXS intensity from a reference point, say Γ, to other RISP $\boldsymbol{k}_*$. That is, we select the momentum transfer: $\boldsymbol{q}_n = \boldsymbol{k}_* + \sum_{i=1}^{3} n_i \boldsymbol{G}_i$ with $\boldsymbol{G}_i$ being a primitive reciprocal vector. The RIXS intensity can be expanded as

$$\frac{I(\boldsymbol{q}_n, \Delta\epsilon)}{|\mathcal{C}(\Delta\epsilon)|^2} = 2\sin^2\left(\boldsymbol{q}_n\cdot\boldsymbol{d} + \frac{1}{4}(\mathcal{I}_v(\boldsymbol{k}_*)\mathcal{I}_v(\Gamma) - 1)\pi\right), \quad (48)$$

where $\boldsymbol{q}_n = \boldsymbol{k}_* + \sum_{i=1,2,3} n_i\boldsymbol{G}_i$, $(n_i \in \mathbb{Z})$ with $\boldsymbol{G}_i$ is a reciprocal lattice vector and $\boldsymbol{d} = (0, 0, d)$ is a sublattice vector. Obtained RIXS intensity manifests the RIXS intensity encodes a product of inversion eigenvalues of $\boldsymbol{k}_*$ and Γ, which implies topological band index can be constructed.

B. Proof of Eq. (48)

To prove Eq. (48), we start with the RIXS intensity which can be expanded in terms of eigenstates of $h_{\mathrm{CHI}}(\boldsymbol{k})$ as in the 3D topological band insulator case

$$\frac{I(\boldsymbol{q}_n, \Delta\epsilon)}{|\mathcal{C}(\Delta\epsilon)|^2} = \sum_{\mu,\nu} |\psi^\dagger_{c,\mu}(\boldsymbol{k}_*)\hat{\mathcal{M}}_{\boldsymbol{q}_n}\psi_{v,\nu}(\Gamma)|^2, \quad (49)$$

where $\psi_{c/v,\mu}(\boldsymbol{k})$ is an eigenstate of $h_{\mathrm{CHI}}(\boldsymbol{k})$ with a degeneracy index μ. See Appendix F for notations. Here, $\hat{\mathcal{M}}_{\boldsymbol{q}_n}$ contains sublattice information,

$$\hat{\mathcal{M}}_{\boldsymbol{q}_n} = \cos(\boldsymbol{q}_n\cdot\boldsymbol{d}) + i\sin(\boldsymbol{q}_n\cdot\boldsymbol{d})\hat{\Pi}, \quad (50)$$

with $\hat{\Pi} = \tau_3\sigma_0$. By plugging $\hat{\Pi}$ into the RIXS intensity, we obtain

$$\frac{I(\boldsymbol{q}_n, \Delta\epsilon)}{|\mathcal{C}(\Delta\epsilon)|^2} = \sum_{\mu,\nu} |\cos(\boldsymbol{q}_n\cdot\boldsymbol{d})\psi^\dagger_{c,\mu}(\boldsymbol{k}_*)\psi_{v,\nu}(\Gamma) + i\sin(\boldsymbol{q}_n\cdot\boldsymbol{d})\psi^\dagger_{c,\mu}(\boldsymbol{k}_*)\hat{\Pi}\psi_{v,\nu}(\Gamma)|^2.$$

We first note that the $\hat{C}_4^z\hat{I}$ eigenvalues of $\{\psi_{v,\mu}(\boldsymbol{k}_*), \psi_{v,\bar{\mu}\neq\mu}(\Gamma)\}$ can be ordered to be $\{\mathcal{I}_v(\boldsymbol{k}_*)e^{\pm i\frac{\pi}{4}}, \mathcal{I}_v(\Gamma)e^{\mp i\frac{\pi}{4}}\}$ from symmetry algebra (details of algebras can be found in Appendix F). This implies $\psi^\dagger_{c,\mu}(\boldsymbol{k}_*)\psi_{v,\bar{\mu}\neq\mu}(\Gamma) = 0$ where $\psi_{c,\mu}(\boldsymbol{k}_*) = \hat{\Pi}\psi_{v,\mu}(\boldsymbol{k}_*)$, because

$$\begin{aligned}\psi^\dagger_{c,\mu}(\boldsymbol{k}_*)\psi_{v,\bar{\mu}}(\Gamma) &= \psi^\dagger_{c,\mu}(\boldsymbol{k}_*)(\hat{C}_4^z\hat{I})^\dagger(\hat{C}_4^z\hat{I})\psi_{v,\bar{\mu}}(\Gamma)\\ &= -\mathcal{I}_v(\boldsymbol{k}_*)e^{\pm i\pi/4}\mathcal{I}_v(\Gamma)e^{\pm i\pi/4}\psi^\dagger_{c,\mu}(\boldsymbol{k}_*)\\ &\quad\times\ \psi_{v,\bar{\mu}}(\Gamma),\\ &= \mp i\mathcal{I}_v(\boldsymbol{k}_*)\mathcal{I}_v(\Gamma)\psi^\dagger_{c,\mu}(\boldsymbol{k}_*)\psi_{v,\bar{\mu}}(\Gamma).\end{aligned}$$

In the second line, we have used $\mathcal{I}_v(\boldsymbol{k}_*) = -\mathcal{I}_c(\boldsymbol{k}_*)$ from $\{\hat{C}_4^z\hat{I}, \hat{\Pi}\} = 0$ for $\boldsymbol{k}_* \in$ RISP. Similarly,

$$\begin{aligned}\psi^\dagger_{c,\mu}(\boldsymbol{k}_*)\hat{\Pi}\psi_{v,\bar{\mu}}(\Gamma) &= \psi^\dagger_{c,\mu}(\boldsymbol{k}_*)(\hat{C}_4^z\hat{I})^\dagger(\hat{C}_4^z\hat{I})\hat{\Pi}\psi_{v,\bar{\mu}}(\Gamma),\\ &= \mathcal{I}_v(\boldsymbol{k}_*)e^{\pm i\pi/4}\mathcal{I}_v(\Gamma)e^{\pm i\pi/4}\psi^\dagger_{c,\mu}(\boldsymbol{k}_*)\\ &\quad\times\ \hat{\Pi}\psi_{v,\bar{\mu}}(\Gamma),\\ &= \pm i\mathcal{I}_v(\boldsymbol{k}_*)\mathcal{I}_v(\Gamma)\psi^\dagger_{c,\mu}(\boldsymbol{k}_*)\hat{\Pi}\psi_{v,\bar{\mu}}(\Gamma).\end{aligned}$$

so, $\psi^\dagger_{c,\mu}(\boldsymbol{k}_*)\hat{\Pi}\psi_{v,\bar{\mu}}(\Gamma) = 0$. Therefore the RIXS intensity for this case is diagonal in the degeneracy index, and is reduced to

$$\frac{I(\boldsymbol{q}_n, \Delta\epsilon)}{|\mathcal{C}(\Delta\epsilon)|^2} = \sum_{\mu} |\cos(\boldsymbol{q}_n\cdot\boldsymbol{d})\psi^\dagger_{c,\mu}(\boldsymbol{k}_*)\psi_{v,\mu}(\Gamma) + i\sin(\boldsymbol{q}_n\cdot\boldsymbol{d})\psi^\dagger_{c,\mu}(\boldsymbol{k}_*)\hat{\Pi}\psi_{v,\mu}(\Gamma)|^2.$$

For this case, we want to prove that

$$\begin{cases}\text{if } \mathcal{I}_v(\boldsymbol{k}_*)\mathcal{I}_v(\Gamma) = -1, & \text{then } |\psi^\dagger_{c,\mu}(\boldsymbol{k}_*)\psi_{v,\mu}(\Gamma)|^2 = 1, \quad |\psi^\dagger_{c,\mu}(\boldsymbol{k}_*)\hat{\Pi}\psi_{v,\mu}(\Gamma)|^2 = 0,\\ \text{if } \mathcal{I}_v(\boldsymbol{k}_*)\mathcal{I}_v(\Gamma) = 1, & \text{then } |\psi^\dagger_{c,\mu}(\boldsymbol{k}_*)\psi_{v,\mu}(\Gamma)|^2 = 0, \quad |\psi^\dagger_{c,\mu}(\boldsymbol{k}_*)\hat{\Pi}\psi_{v,\mu}(\Gamma)|^2 = 1,\end{cases} \quad (51)$$

which gives Eq. (48). To prove Eq. (51), we consider $\psi^\dagger_{c,\mu}(\boldsymbol{k}_*)\psi_{v,\mu}(\Gamma)$, where we insert an identity, $(\hat{C}_4^z\hat{I})^\dagger(\hat{C}_4^z\hat{I})$,

$$\begin{aligned}&\psi^\dagger_{c,\mu}(\boldsymbol{k}_*)\psi_{v,\mu}(\Gamma)\\ &= \psi^\dagger_{c,\mu}(\boldsymbol{k}_*)(\hat{C}_4^z\hat{I})^\dagger(\hat{C}_4^z\hat{I})\psi_{v,\mu}(\Gamma),\\ &= -\mathcal{I}_v(\boldsymbol{k}_*)e^{\pm i\pi/4}\mathcal{I}_v(\Gamma)e^{\mp i\pi/4}\psi^\dagger_{c,\mu}(\boldsymbol{k}_*)\psi_{v,\mu}(\Gamma),\\ &= -\mathcal{I}_v(\boldsymbol{k}_*)\mathcal{I}_v(\Gamma)\psi^\dagger_{c,\mu}(\boldsymbol{k}_*)\psi_{v,\mu}(\Gamma).\end{aligned}$$

Therefore, if $\mathcal{I}_v(\boldsymbol{k}_*)\mathcal{I}_v(\Gamma) = 1$, then $\psi^\dagger_{c,\mu}(\boldsymbol{k}_*)\psi_{v,\mu}(\Gamma) = 0$. At the same time, we have $\psi^\dagger_{c,\mu}(\boldsymbol{k}_*)\psi_{v,\bar{\mu}}(\Gamma) = 0$, $\psi^\dagger_{c,\mu}(\boldsymbol{k}_*)\hat{\Pi}\psi_{v,\bar{\mu}}(\Gamma) = 0$ for $\bar{\mu} \neq \mu$. They together imply $|\psi^\dagger_{c,\mu}(\boldsymbol{k}_*)\hat{\Pi}\psi_{v,\mu}(\Gamma)| = 1$. For $\mathcal{I}_v(\boldsymbol{k}_*)\mathcal{I}_v(\Gamma) = -1$ case, one can similary show that if $\psi^\dagger_{c,\mu}(\boldsymbol{k}_*)\hat{\Pi}\psi_{v,\mu}(\Gamma) = 0$ and $|\psi^\dagger_{c,\mu}(\boldsymbol{k}_*)\psi_{v,\mu}(\Gamma)| = 1$ since $\{\hat{C}_4^z\hat{I}, \hat{\Pi}\} = 0$, which completes our proof.

C. Numerical simulations

Next, we numerically demonstrate how we can read off the topological band index from RIXS intensities. The RIXS intensity data (Fig. 7) with momentum transfer $\boldsymbol{q}_n = (2n + 1)(0, 0, \pi)$ and energy transfer $\Delta\epsilon = \epsilon_c(Z) - \epsilon_v(\Gamma)$ are generated by adding the two contributions

$$\mathcal{I}(\boldsymbol{q}_n, \Delta\epsilon) = \mathcal{I}_0(\boldsymbol{q}_n, \Delta\epsilon) + \delta\mathcal{I}_{\mathrm{random}}, \quad (52)$$

where $\mathcal{I}_0(\boldsymbol{q}_n, \Delta\epsilon)$ is the RIXS intensity from the insulator, and $\delta\mathcal{I}_{\mathrm{random}}$ is the random noise. Essentially, $\mathcal{I}_0(\boldsymbol{q}_n, \Delta\epsilon)$ is the analytic, perfect RIXS signal on the clean H_{CHI} model.

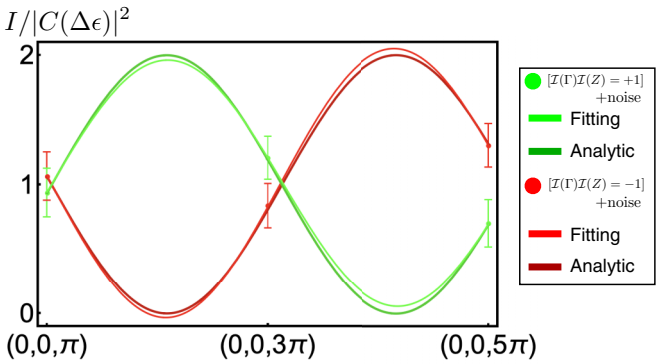

FIG. 7. RIXS intensity of H_{CHI} model with momentum transfer $\boldsymbol{q}_n = (2n+1)(0,0,\pi)$ and energy transfer $\omega{=}\Delta\epsilon{=}\epsilon_c(Z) - \epsilon_v(\Gamma)$. As in the previous examples, the error bars for the data (filled circles) are due to the noise that we included in our simulation.

On the other hand, $\delta\mathcal{I}_{\mathrm{random}}$ is the white noise drawn from the uniform distribution $[-0.3, 0.3] \times |\mathcal{C}(\Delta\epsilon)|^2$.

For the topological case $\nu = 1 \bmod 2$, i.e., $\mathcal{I}(\Gamma)\mathcal{I}(Z) = +1$, (red circles in Fig. 7), the parameter of the H_{CHI} model is $M/t = -2.9$ (see Appendix F for the parameters). For the trivial case $\nu = 0 \bmod 2$, i.e., $\mathcal{I}(\Gamma)\mathcal{I}(Z) = -1$ (green circles in Fig. 7), the parameter is $M/t = -3.1$ (so that $\Delta\epsilon$ is the same for the both cases). We set $d = 0.24$ for both the cases.

We have attempted to fit the data with $\mathcal{I}(\boldsymbol{q}_n, \Delta\epsilon)/|C(\Delta\epsilon)|^2 = A\sin^2((2n+1)\pi B + I) + C$, [cf. Eq. (48)]. Here $I \in [-\pi, 0]$ will be the diagnostics of the band topology, i.e., $I = \frac{\pi}{4}(\mathcal{I}_v(Z)\mathcal{I}_v(\Gamma) - 1)$. For the idealistic, perfect signal of the trivial case (without the noise $\delta\mathcal{I}_{\mathrm{random}}$), we expect to find

$$A = 2,\ B = 0.24,\ C = 0,\ \text{and}\ I = 0, \tag{53}$$

which is the darker green line in Fig. 7. As the result of the fitting (the light green line in Fig. 7), we found

$$A = 1.90,\ B = 0.23,\ C = 0.05,\ \text{and}\ I = 0.00, \tag{54}$$

which are pretty close to the exact values (53). In particular, this correctly determines $\mathcal{I}_v(Z)\mathcal{I}_v(\Gamma) = 1.00$.

For the idealistic, perfect signal of topological case (without the noise $\delta\mathcal{I}_{\mathrm{random}}$), we expect to find

$$A = 2,\ B = 0.24,\ C = 0,\ \text{and}\ I = -1.58, \tag{55}$$

which is the darker red line in Fig. 7. As the result of the fitting (the lighter red line in Fig. 7), we found

$$A = 2.08,\ B = 0.24,\ C = -0.03,\ \text{and}\ I = -1.57, \tag{56}$$

which are pretty close to the exact values (55). In particular, this correctly determines $\mathcal{I}_v(Z)\mathcal{I}_v(\Gamma) = -0.99$. Therefore one can read off $\mathcal{I}_v(\Gamma)\mathcal{I}_v(Z)$ from this RIXS intensity, from which one can infer the topological band index.

VIII. CONCLUSION

In this work, we have shown that the RIXS intensity directly reflects the band topology of various insulators in different spatial dimensions. Essentially, the RIXS intensity is strongly constrained by the crystalline symmetry eigenvalues and this allows one to reconstruct the topological band indices. We have explicitly demonstrated this strategy in 1D SSH chain, 2D quadrupolar insulator, 2D C_4-symmetric higher order topological insulator, 3D topological band insulator, and also higher order chiral hinge insulators. From these examples, it is not difficult to anticipate that a broader class of topology [48–53] of band insulators and superconductors (beyond the examples discussed in this work) may as well be manifested in RIXS. We leave the generalization to the future research.

ACKNOWLEDGMENTS

We thank J. Ahn and Y.K. Kim for the helpful discussions. G.Y.C. acknowledges the support of the National Research Foundation of Korea (NRF) funded by the Korean Government (Grants No. 2020R1C1C1006048 and No. 2020R1A4A3079707), as well as Grant No. IBS-R014-D1. G.Y.C. is also supported by the Air Force Office of Scientific Research under Awards No. FA2386-20-1-4029 and No. FA2386-22-1-4061. G.Y.C. acknowledges Samsung Science and Technology Foundation under Project Number SSTF-BA2002-05. B.J.K. was supported by IBS-R014-A2. S.J.L. was supported by an appointment to the JRG/YST Program at the APCTP through the Science and Technology Promotion Fund and Lottery Fund of the Korean Government. This was also supported by the Korean Local Governments-Gyeongsangbuk-do Province and Pohang City. S.J.L. is also supported by IBS-R014-D1. B.K. is supported by KIAS individual Grant PG069402 at Korea Institute for Advanced Study and the National Research Foundation of Korea (NRF) grant funded by the Korea government (MSIT) (No. 2020R1F1A1075569). K.-H.J. is supported by the Institute for Basic Science (Grant No. IBS-R014-Y1).

APPENDICES

Since the Appendix is rather long, here we summarize the organization of the Appendix. In Appendix A, we provide more information on RIXS formalism. This is basically the expansion of the section . In Appendix B, we review the basic physics of the SSH model focusing on its symmetry and band topology. We also provide a four-band generalization of the SSH model, on which our proposal is not restricted to the two-band systems. Even more, we show that we can read off the band-wise polarization. Note that in Appendix B 4, we provide our DFT data and its details on the candidate SSH materials $A_2M_2X_6$. In Appendix C, we review the physics of the 2D quadrupole insulator models, on which we focus on their symmetry and topology. In Appendix D, we present the physics of the 2D C_4-symmetric higher order topological insulator. As similar in the previous models, we mainly consider the symmetry and band topology of the model. In Appendix E, we review the physics of 3D inversion symmetric topological insulator model on the diamond lattice. We particularly focus on the inversion and time-reversal symmetries as well as the $\mathbb{Z}_2$ band index. In Appendix F, we finally review the basics of the 3D chiral hinge insulator model.

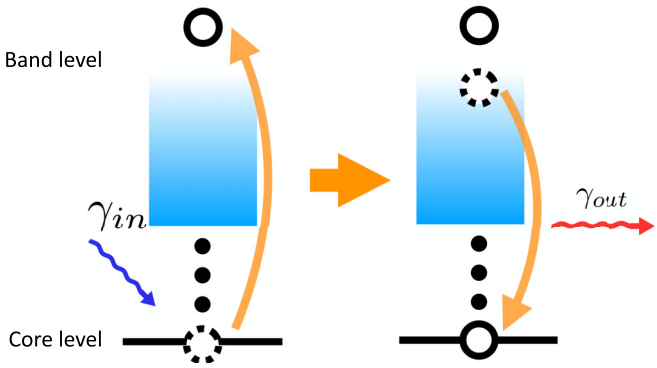

FIG. 8. RIXS process. An incident photon transfers the core electron to an empty state, which leaves a core hole and an electron excitation. This configuration decays rather quickly and the core hole is filled back by another electron. This leaves an electron-hole pair excitation.

APPENDIX A: RIXS INTENSITY

Here we present a brief review of the theoretical formulation of the RIXS spectral intensity [1]. Our starting point is the RIXS sepctral intensity formula with momentum transfer $\boldsymbol{q}$ and energy transfer $\Delta\omega$.

$$\mathcal{I}(\Delta\boldsymbol{q},\Delta\omega) = \sum_f |\mathcal{A}_{fi}(\boldsymbol{k}_f-\boldsymbol{k}_i=\Delta\boldsymbol{q},\omega_f-\omega_i = \Delta\omega,\boldsymbol{\epsilon}_i,\boldsymbol{\epsilon}_f)|^2\delta(E_f-E_i-\Delta\omega), \quad \text{(A1)}$$

which sums over allowed states f. Here $\mathcal{A}_{fi}$ is a RIXS quantum amplitude which is a function of incident (outgoing) photon momentum $\boldsymbol{k}_{i(f)}$ with energy $\omega_{i(f)}$ and polarization $\boldsymbol{\epsilon}_{i(f)}$. Next, E_i and E_f are the energy of many-electron states before and after the scattering process.

1. RIXS quantum amplitude

Formally, the quantum amplitude $\mathcal{A}_{fi}$ is determined by internal processes (see Fig. 8).

$$\mathcal{A}_{fi} = \langle f|\hat{D}(\boldsymbol{k}_f,\epsilon_f)\,\hat{G}_{\text{core-hole}}(\omega)\,\hat{D}^\dagger(\boldsymbol{k}_i,\epsilon_i)|g\rangle, \quad \text{(A2)}$$

where $\hat{D}$ is a transition operator that transits a core electron to an empty state, i.e., a state in the conduction band. Here $\hat{G}_{\text{core-hole}}(\omega)$ is the green's function of the whole system with a core hole and the excited electron. It is instructive to perform the spectral decomposition of $\hat{G}_{\text{core-hole}}(\omega)$:

$$\hat{G}_{\text{core-hole}}(\omega) = \sum_n \frac{|n\rangle\langle n|}{\omega - E_n + i\Gamma_n}, \quad \text{(A3)}$$

where E_n is the energy of an intermediate state with a core hole and an excited electron, and Γ_n is an inverse of the lifetime of the intermediate state. We assume that the core-hole lifetime is very short, e.g., it is roughly $O(1)$ fs in $4d/5d$ materials [54,55] which makes the excitation remain at the same site during the scattering. Near the resonant condition, we can effectively take all the Γ_n as a single number Γ, i.e., $\Gamma_n \approx \Gamma \gg |\omega - E_n|$ which is known as the fast collision approximation [1,40–42]

$$\hat{G}_{\text{core-hole}}(\omega) \simeq \sum_n \frac{|n\rangle\langle n|}{\omega - E_n + i\Gamma}. \quad \text{(A4)}$$

Here, $\hat{G}_{\text{core-hole}}(\omega)$ as written above can incorporate nontrivial dynamics of the intermediate states, for example, the excitonic effect (interaction between the core hole and excited electron) [41,43,56,57].

Next we identify the dipole transition operator $\hat{D}$. In general, we have

$$\hat{D}(\boldsymbol{k},\hat{\epsilon}) = \sum_{\boldsymbol{R},\ell,\ell',\sigma,\sigma'} e^{i\boldsymbol{k}\cdot\boldsymbol{R}}\langle c;\ell,\sigma|\hat{\epsilon}\cdot\vec{r}|d;\ell',\sigma'\rangle c_{\boldsymbol{R},\ell,\sigma}d^\dagger_{\boldsymbol{R},\ell',\sigma'} + \text{H.c.}, \quad \text{(A5)}$$

which transits a core electron $c_{\boldsymbol{R},\ell,\sigma}$ to another valence state ($d_{\boldsymbol{R},\ell',\sigma'}$), where ℓ represents the orbital of the relevant electronic states and σ represents the electronic spins. Here, $d_{\boldsymbol{R},\ell,\sigma}$ are the fermions which forms the basis for the tight-binding models whose topology we wish to investigate in the main text. Note that the information encoded in this operator $\hat{D}(\boldsymbol{k},\hat{\epsilon})$ is atomic, which is in principle independent to the detailed values of the hopping integrals of the low-energy tight-binding models.

Plugging Eqs. (A4) and (A5) into Eq. (A2), we obtain

$$\mathcal{A}_{fi} = \sum_{\boldsymbol{R}}\sum_n \sum_{(\ell,\sigma),(\ell',\sigma')} g_n(\omega)M_{\hat{\epsilon}_i,\hat{\epsilon}_f,n;(\ell'\sigma'),(\ell,\sigma)} \times \langle f|d_{\boldsymbol{R},\ell',\sigma'}d^\dagger_{\boldsymbol{R},\ell,\sigma}e^{i\boldsymbol{q}\cdot\boldsymbol{R}}|g\rangle, \quad \text{(A6)}$$

where $g_n^{-1}(\omega) = \omega - E_n + i\Gamma$ and $\boldsymbol{q} = \boldsymbol{k}_f - \boldsymbol{k}_i$. Depending on the matrix elements of $M_{\hat{\epsilon}_i,\hat{\epsilon}_f,n,\sigma,\sigma'}$, one can access either the non-spin-flip RIXS (which allows only the transition between the electronic states of $\sigma = \sigma'$) or the spin-flip RIXS (which allows the transitions between the states $\sigma \neq \sigma'$).

When the polarizations of the photons are carefully chosen, or when the RIXS transition itself does not allow the spin flip (e.g., Bi $2s \to 6p$ transition), we can access the non-spin-flip RIXS [43], i.e., $M_{\hat{\epsilon}_i,\hat{\epsilon}_f,n;(\ell',\sigma'),(\ell,\sigma)} = M_{\hat{\epsilon}_i,\hat{\epsilon}_f,n;\ell}\delta_{\sigma,\sigma'}$. Thus we find

$$\mathcal{A}_{fi} = \sum_{\boldsymbol{R}}\sum_n\sum_\sigma g_n(\omega)M_{\hat{\epsilon}_i,\hat{\epsilon}_f,n}\cdot\langle f|d_{\boldsymbol{R},\sigma}d^\dagger_{\boldsymbol{R},\sigma}e^{i\boldsymbol{q}\cdot\boldsymbol{R}}|g\rangle = \mathcal{C}(\omega)\sum_\sigma\sum_{\boldsymbol{R}}\langle f|d_{\boldsymbol{R},\sigma}d^\dagger_{\boldsymbol{R},\sigma}e^{i\boldsymbol{q}\cdot\boldsymbol{R}}|g\rangle \quad \text{(A7)}$$

In the above, we have suppressed notating ℓ because we have assumed that there is one particular ℓ, e.g., $5d_{xz}$, which is relevant both in a particular RIXS edge (that we would like to utilize) and selected polarizations of the photons. Here, let us emphasize that $d_{\boldsymbol{R},\ell,\sigma}$ has nothing to do with the Wannier states of certain bands. This is obvious because $d_{\boldsymbol{R},\ell,\sigma}$, which is atomic and localized in real space, is clearly not an eigenstate of generic Hamiltonian. Thus it is not the real-space representation of certain band. Nevertheless, to have a desired transition, it is certainly needed to require $d_{\boldsymbol{R},\ell,\sigma}$ to have a finite overlap with the target states included in the transition. Here, $\mathcal{C}(\omega) = \sum_n g_n(\omega)M_{\hat{\epsilon}_i,\hat{\epsilon}_f,n}$ which depends on the details such as $g_n(\omega)$ and also the polarizations of photons $(\hat{\epsilon}_i,\hat{\epsilon}_f)$. The RHS of Eq. (A7) is Eq. (2) in our main text. In the

following section, we will work out $M_{\hat{\epsilon}_i,\hat{\epsilon}_f,n;(\ell'\sigma'),(\ell,\sigma)}$ for the transition $2p \to 5d$, which are relevant for the W-based SSH materials $A_2W_6S_6$ (see Appendix B 4). There, we will also show that in principle, the spin-flip and non-spin-flip RIXS can be selected by appropriately choosing the polarizations of incident and scattered photons.

2. Example: $2p \to 5d_{xz}$ transition

As a concrete example, we will work out the details of the RIXS transition $2p \to 5d_{xz}$, which may be relevant for $A_2W_6S_6$ (Appendix B 4) with $5d$ element W. We will also discuss the effect of the polarizations of the photons.

Let us start with the core-hole state. In the $5d$ elements, the core-hole spin-orbit coupling can be strong. Because of this spin-orbit coupling, the core-hole states are splitted into the two different angular-momentum sectors $J = 3/2$ and $1/2$, which are energetically separated. We will focus on the $J = 3/2$ states below, although the discussion can be easily generalized to the case with $J = 1/2$.

Within the dipole approximation, we will need the following matrix element to calculate the RIXS amplitude:

$$\langle 5d_{xz}|\hat{\epsilon}\cdot\vec{r}|2p_{i=x,y,z},\sigma = \uparrow,\downarrow\rangle, \tag{A8}$$

where $\hat{\epsilon}$ is the polarization of the photon involved in the transition. We introduce the following polarization basis for the convenience:

$$|m=0\rangle = |2p_z\rangle, \quad |m=\pm1\rangle = \frac{1}{\sqrt{2}}\big(|2p_x\rangle \pm i|2p_y\rangle\big),$$
$$\hat{r}_{\pm1} = \frac{1}{\sqrt{2}}(\hat{x}\pm i\hat{y}), \quad \hat{r}_0 = \hat{z}.$$

During the RIXS process, the total angular momentum is conserved even in the strong spin-orbit coupled systems. Hence, we use the total angular momentum basis

$$\left|J=\frac{3}{2},m_J=\frac{3}{2}\right\rangle = |m=1,\uparrow\rangle,$$
$$\left|J=\frac{3}{2},m_J=\frac{1}{2}\right\rangle = \sqrt{\frac{1}{3}}|m=1,\downarrow\rangle + \sqrt{\frac{2}{3}}|m=0,\uparrow\rangle,$$
$$\left|J=\frac{3}{2},m_J=-\frac{1}{2}\right\rangle = \sqrt{\frac{2}{3}}|m=0,\downarrow\rangle + \sqrt{\frac{1}{3}}|m=-1,\uparrow\rangle,$$
$$\left|J=\frac{3}{2},m_J=-\frac{3}{2}\right\rangle = |m=-1,\downarrow\rangle,$$
$$\left|J=\frac{1}{2},m_J=\frac{1}{2}\right\rangle = -\sqrt{\frac{1}{3}}|m=0,\uparrow\rangle + \sqrt{\frac{2}{3}}|m=1,\downarrow\rangle,$$
$$\left|J=\frac{1}{2},m_J=-\frac{1}{2}\right\rangle = \sqrt{\frac{1}{3}}|m=0,\downarrow\rangle - \sqrt{\frac{2}{3}}|m=-1,\uparrow\rangle.$$

Using this basis, we will compute relevant matrix elements associated with $2p \to 5d_{xz}$, which are

$$\langle 5d_{xz}|\hat{\epsilon}\cdot\vec{r}|m=\ell\rangle = M_\ell \hat{\epsilon}\cdot\hat{r}_\ell, \tag{A9}$$

where

$$M_{\pm1} = M_{xz} = \frac{1}{\sqrt{2}}\langle 5d_{xz}|r_x|2p_z\rangle,$$
$$M_0 = M_{zx} = \langle 5d_{xz}|r_z|2p_x\rangle. \tag{A10}$$

Plugging these, we find the dipole transition operator

$$\hat{D}(\boldsymbol{q}) = \sum_{\boldsymbol{R},\ell,\sigma} e^{-i\boldsymbol{q}\cdot\boldsymbol{R}} M_\ell \hat{\epsilon}\cdot\hat{r}_\ell d^\dagger_{\boldsymbol{R},\sigma} p_{\boldsymbol{R},\ell,\sigma},$$
$$= M_{xz}\sum_{\boldsymbol{R}} e^{-i\boldsymbol{q}\cdot\boldsymbol{R}}\hat{\epsilon}\cdot\left(\hat{r}_1\left(d^\dagger_{\boldsymbol{R},\uparrow}p_{\boldsymbol{R},m_J=\frac{3}{2}} + \sqrt{\frac{1}{3}}d^\dagger_{\boldsymbol{R},\downarrow}p_{i,m_J=\frac{1}{2}}\right) + \hat{r}_{-1}\left(d^\dagger_{\boldsymbol{R},\downarrow}p_{\boldsymbol{R},m_J=-\frac{3}{2}} + \sqrt{\frac{1}{3}}d^\dagger_{\boldsymbol{R},\uparrow}p_{\boldsymbol{R},m_J=-\frac{1}{2}}\right)\right)$$
$$+ \sqrt{\frac{2}{3}}M_{zx}\sum_i e^{-i\boldsymbol{q}\cdot\boldsymbol{R}}\hat{\epsilon}\cdot\hat{r}_0\big(d^\dagger_{\boldsymbol{R},\uparrow}p_{\boldsymbol{R},m_J=\frac{1}{2}} + d^\dagger_{\boldsymbol{R},\downarrow}p_{\boldsymbol{R},m_J=-\frac{1}{2}}\big). \tag{A11}$$

Inserting this to the RIXS amplitude (whose energy transfer ω is tuned to induce the transition between $2p$ and $5d_{xy}$), we find

$$\mathcal{A}_{fi}(\boldsymbol{q},\omega) = \sum_{\boldsymbol{R}}\sum_{\alpha,\beta=\{\uparrow,\downarrow\}} g(\omega)\chi_{\alpha\beta}\langle f|d_{\boldsymbol{R},\alpha}d^\dagger_{\boldsymbol{R},\beta}e^{-i\boldsymbol{q}\cdot\boldsymbol{R}}|g\rangle \tag{A12}$$

where $\chi_{\alpha\beta}$ for $2p \to 5d_{xz}$ is given by

$$\chi_{\uparrow\uparrow} = \chi^*_{\downarrow\downarrow} = |M_{xz}|^2\left((\hat{\epsilon}_f\cdot\hat{r}_1)^*(\hat{\epsilon}_i\cdot\hat{r}_1) + \frac{1}{3}(\hat{\epsilon}_f\cdot\hat{r}_{-1})^*(\hat{\epsilon}_i\cdot\hat{r}_{-1})\right) + \frac{2}{3}|M_{zx}|^2(\hat{\epsilon}_f\cdot\hat{r}_0)^*(\hat{\epsilon}_i\cdot\hat{r}_0),$$
$$\chi_{\uparrow\downarrow} = \chi^*_{\downarrow\uparrow} = \frac{\sqrt{2}}{3}(M_{xz}M^*_{zx}(\hat{\epsilon}_f\cdot\hat{r}_0)^*(\hat{\epsilon}_i\cdot\hat{r}_1) + M^*_{xz}M_{zx}(\hat{\epsilon}_f\cdot\hat{r}_1)^*(\hat{\epsilon}_i\cdot\hat{r}_0)). \tag{A13}$$

This $\chi_{\alpha,\beta}$ can be actually further recast into

$$\chi_{\alpha\beta} = m_{\mathrm{NSF}}\delta_{\alpha\beta}\hat{\epsilon}^*_f\cdot\hat{\epsilon}_i + m_{\mathrm{SF}}\vec{\sigma}_{\alpha\beta}\cdot(\hat{\epsilon}^*_f\times\hat{\epsilon}_i). \tag{A14}$$

where m_{NSF} and m_{SF} are the corresponding coefficients (which can be written out explicitly in terms of M_{xz} and M_{zx}) [9]. Hence, when $\hat{\epsilon}^*_f\times\hat{\epsilon}_i = 0$, only the non-spin-flip process will

be allowed. With this, we finally find

$$\mathcal{A}_{fi}(\boldsymbol{q},\omega) = \sum_{\boldsymbol{R}} \sum_{\alpha,\beta=\{\uparrow,\downarrow\}} g(\omega)\chi_{\alpha\beta}\langle f|d_{\boldsymbol{R},\alpha}d^{\dagger}_{\boldsymbol{R},\beta}e^{-i\boldsymbol{q}\cdot\boldsymbol{R}}|g\rangle$$

$$= \mathcal{C}(\omega)\sum_{\boldsymbol{R}}\sum_{\sigma}\langle f|d_{\boldsymbol{R},\sigma}d^{\dagger}_{\boldsymbol{R},\sigma}e^{-i\boldsymbol{q}\cdot\boldsymbol{R}}|g\rangle, \tag{A15}$$

where we have identified $g(\omega)\chi_{\alpha\beta} = g(\omega)m_{\mathrm{NSF}}\delta_{\alpha\beta}$ as $\mathcal{C}(\omega)$.

APPENDIX B: 1D SU-SCHRIEFFER-HEEGER (SSH) MODEL

1. Review of SSH model

Here, we present a brief review of the SSH model [32]. We will temporarily suppress the spin index because the model has the spin-rotational symmetry. The SSH Hamiltonian is given as

$$H_{\mathrm{SSH}} = -\sum_{x\in\mathbb{Z}}(t_1 c^{\dagger}_{x,1}c_{x,2} + t_2 c^{\dagger}_{x,2}c_{x+1,1} + \mathrm{H.c.}), \tag{B1}$$

where $t_1(t_2)$ is an intra(inter) site hopping parameter. $c^{\dagger}_{x,\alpha}$ creates electrons at $x_\alpha = x + d_\alpha$ with $d_{\alpha=1,2} = (-1)^\alpha d$. Hence, the unitcell size is normalized to be "1." Within a unitcell, there are two sublattices labeled by α, whose positions are $\mathbb{Z} \pm d$. The real-space position of the sublattices is not often discussed in detail because it does not affect the symmetry and topology of the model. However, the RIXS intensity depends on the distance between the sublattices and so we will need to keep track of this below.

Much of the important physics of the model can be well illustrated in momentum space. Hence, we proceed to the momentum space by performing the Fourier transformation

$$c_{x,\alpha} = \sum_k c_{k,\alpha}e^{ikx}. \tag{B2}$$

With this in hand, the Hamiltonian can be written as

$$H_{\mathrm{SSH}} = \sum_k \boldsymbol{c}^{\dagger}_k h_{\mathrm{SSH}}(k)\boldsymbol{c}_k, \tag{B3}$$

where

$$h_{\mathrm{SSH}}(k) = -\begin{pmatrix} 0 & t_1 + t_2 e^{-ik} \\ t_1 + t_2 e^{ik} & 0 \end{pmatrix} \tag{B4}$$

and $\boldsymbol{c}^T_k = (c_{k,1}, c_{k,2})$. Next, we diagonalize the Hamiltonian, $\gamma_{\eta,s}(k) = U_{\eta\alpha}c_{k,\alpha,s}$ such that

$$U^{\dagger} = [\psi_c(k)|\psi_v(k)], \tag{B5}$$

where $\psi_{c,v}(k)$ are the Bloch functions. With this, we obtain the standard results

$$H_{\mathrm{SSH}} = \sum_{k,\eta=c,v}\varepsilon_\eta(k)\gamma^{\dagger}_\eta(k)\gamma_\eta(k),$$

$$\varepsilon_{\eta=c,v}(k) = \pm\sqrt{t_1^2 + t_2^2 + 2t_1t_2\cos k}. \tag{B6}$$

2. Symmetry

There can be two symmetries in the model: the reflection symmetry and the chiral symmety. Among the two, we will use only the reflection symmetry to derive the RIXS intensity later. That is, although we discuss the chiral symmetry for completeness, our results apply to the systems without the chiral symmetry.

Let us start with the reflection symmetry, which is represented as $\hat{\mathcal{R}} \doteq \sigma^1$.

$$\mathcal{R} : \boldsymbol{c}_k \to \hat{\mathcal{R}}\cdot\boldsymbol{c}_{-k} = \sigma^1\cdot\boldsymbol{c}_{-k}. \tag{B7}$$

We will enforce the reflection symmetry, e.g., $\hat{\mathcal{R}}\cdot H_{\mathrm{SSH}}\cdot\hat{\mathcal{R}}^{-1} = H_{\mathrm{SSH}}$.

Secondly, the chiral symmetry is given by $\hat{\Pi} \doteq \sigma^3$, which is the unitary matrix part of the symmetry operation on the fermion fields

$$\Pi : \boldsymbol{c}_k \to \hat{\Pi}\cdot\boldsymbol{c}_k = \sigma^3\cdot\boldsymbol{c}_k. \tag{B8}$$

This is in fact one of the symmetries of the simplest SSH chain model as written above, i.e., $\hat{\Pi}\cdot H_{\mathrm{SSH}}\cdot\hat{\Pi}^{-1} = -H_{\mathrm{SSH}}$. However, we will always assume that *the chiral symmetry is explicitly broken by some perturbations*.

3. Four-band model: polarization per each filled band

In this section, we consider a four-band, nonchiral symmetric model and explicitly demonstrate the applicability of our protocol, which allows us to read off the band topology per each filled band. For the clarity and brevity of our discussion, we will temporarily omit the spin indices.

The model is basing on the two-leg ladder generalization of the SSH chain.

$$H_{\mathrm{ladder}} = H_{1,\mathrm{SSH}} + H_{2,\mathrm{SSH}} + H_{1,2},$$

$$H_{1,\mathrm{SSH}} = -\sum_{x\in\mathbb{Z}}(t_{1,1}c^{\dagger}_{x,1}c_{x,2} + t_{1,2}c^{\dagger}_{x,2}c_{x+1,1} + \mathrm{H.c.}),$$

$$H_{2,\mathrm{SSH}} = -\sum_{x\in\mathbb{Z}}(t_{2,1}c^{\dagger}_{x,3}c_{x,4} + t_{2,2}c^{\dagger}_{x,4}c_{x+1,3} + \mathrm{H.c.}),$$

$$H_{1,2} = -\sum_{x\in\mathbb{Z},i=1,2}(\lambda c^{\dagger}_{x,i}c_{x,i+2} + t_{3,1}c^{\dagger}_{x,i}c_{x,5-i}$$

$$+ t_{3,2}c^{\dagger}_{x,i}c_{x+1,5-i} + \mathrm{H.c.}), \tag{B9}$$

where $t_{a,1}(t_{a,2})$ is an intra(inter)-unitcell hopping parameter of the ath SSH chain. On the other hand, $(t_{3,1}, t_{3,2}, \lambda)$ are the interchain hopping parameters, see Fig. 9(a) for the pictorial representation of the model. Here, $c^{\dagger}_{x,\alpha}$ creates an electron, whose real-space position in x is given by $x_\alpha = x + d_\alpha$ with $d_{\alpha=1,2,3,4} = (-1)^\alpha d$. By performing Fourier transformation,

$$c_{x,\alpha} = \sum_k c_{k,\alpha}e^{ikx},$$

the ladder Hamiltonian is written as

$$H_{\text{ladder-SSH}} = \sum_k \boldsymbol{c}^{\dagger}_k h_{\mathrm{ladder}}(k)\boldsymbol{c}_k,$$

where

$$h_{a=1,2,\mathrm{SSH}}(k) = -\tfrac{1}{2}(\tau_0 - (-1)^a\tau_3)((t_{a,1} + t_{a,2}\cos k)\sigma_1 + t_{a,2}\sin k\sigma_2), \tag{B10}$$

$$h_{1,2}(k) = \lambda\tau_1\sigma_0 + (t_{3,1} + t_{3,2}\cos k)\tau_1\sigma_1 + t_{3,2}\sin k\tau_1\sigma_2, \tag{B11}$$

$$\begin{aligned} h_{\text{ladder-SSH}}(k) &= h_{1,\mathrm{SSH}}(k) + h_{2,\mathrm{SSH}}(k) + h_{1,2}(k) \\ &= -\begin{pmatrix} 0 & t_{1,1} + t_{1,2}e^{-ik} & \lambda & t_{3,1} + t_{3,2}e^{-ik} \\ t_{1,1} + t_{1,2}e^{ik} & 0 & t_{3,1} + t_{3,2}e^{-ik} & \lambda \\ \lambda & t_{3,1} + t_{3,2}e^{ik} & 0 & t_{2,1} + t_{2,2}e^{-ik} \\ t_{3,1} + t_{3,2}e^{ik} & \lambda & t_{2,1} + t_{2,2}e^{ik} & 0 \end{pmatrix}, \end{aligned} \tag{B12}$$

with $\boldsymbol{c}_k^T = (c_{k,1}, c_{k,2}, c_{k,3}, c_{k,4})$. Here, τ_a is the Pauli matrix acting on the chain index and σ_i acts on the sublattice index of each SSH chains. The $h_{\text{ladder}}(k)$ can be diagonalized via $\gamma_\eta(k) = U_{\eta\alpha}c_{k,\alpha}$, where

$$U^\dagger = \left[\psi_{c,1}(k)|\psi_{c,2}(k)|\psi_{v,1}(k)|\psi_{v,2}(k)\right].$$

Then, $\psi_{\eta=c,v,\alpha=1,2}(k)$ corresponds to the Bloch state of h_{ladder}. With this, we find the diagnonalized Hamiltonian

$$H_{\text{ladder}} = \sum_{k,\eta=1,2,3,4} \epsilon_\eta(k)\gamma_\eta^\dagger(k)\gamma_\eta(k).$$

The band structure with generic parameters can be found in Fig. 9(b). As obvious from the spectrum, the chiral symmetry is explicitly broken and there is no particle-hole symmetry. More explicitly, we can show that the chiral symmetry $\hat{\Pi}_{\text{chiral}} \doteq \tau_3\sigma_3$ is explicitly broken, because $\{\hat{\Pi}_{\text{chiral}}, H_{\text{ladder}}\} \neq 0$ when $t_{3,1}$ and $t_{3,2}$ are finite. We will assume that the two lowest bands are filled.

Here, we will show how the band topology for each filled band can be read off from the momentum oscillations of the RIXS intensity. The quantum amplitude with the momentum transfer q in this model can be obtained by

$$\mathcal{A}_f(q,\omega) = \mathcal{C}(\omega)\sum_{x\in\mathbb{Z},\alpha}\langle f|c_{x,\alpha}c_{x,\alpha}^\dagger e^{iqx_\alpha}|g\rangle.$$

By substituting $c_{x,\alpha} = \sum_k U_{\alpha\eta}^\dagger\gamma_\eta(k)e^{ikx}$, we obtain the amplitude in terms of the Bloch states,

$$\begin{aligned} \mathcal{A}_f(q,\omega) = \mathcal{C}(\omega)\sum_k \langle f|(U(k)\hat{\mathcal{M}}_{k+q,k}U^\dagger(k+q))_{\nu\mu}\gamma_\mu \\ \times(k+q)\gamma_\nu^\dagger(k)|g\rangle, \end{aligned} \tag{B13}$$

where $\hat{\mathcal{M}}_{k+q,k} = \cos(qd)1_{4\times4} + i\sin(qd)\hat{\Pi}_{\text{sub}}$ is generated from the spatial separation of the sublattices along x direction of the model. Here, $\hat{\Pi}_{\text{sub}} \doteq \tau_0\sigma_3$. Note that $\hat{\Pi}_{\text{sub}}$ anticommutes with the reflection symmetry operator $\hat{\mathcal{R}} \doteq \tau_0\sigma_1$ and also $\hat{\Pi}_{\text{sub}}$ is distinct from the chiral symmetry $\hat{\Pi}_{\text{chiral}} \doteq \tau_3\sigma_3$.

Implementing the Bloch functions explicitly, we find

$$\begin{aligned} \mathcal{A}_f(q,\omega_{fi}) = \mathcal{C}(\omega_{fi})(\psi_{\text{final}}^\dagger(k+q)\psi_{\text{initial}}(k)\cdot\cos(qd) \\ + i\psi_{\text{final}}^\dagger(k+q)\hat{\Pi}_{\text{sub}} \\ \times\psi_{\text{initial}}(k)\cdot\sin(qd)), \end{aligned} \tag{B14}$$

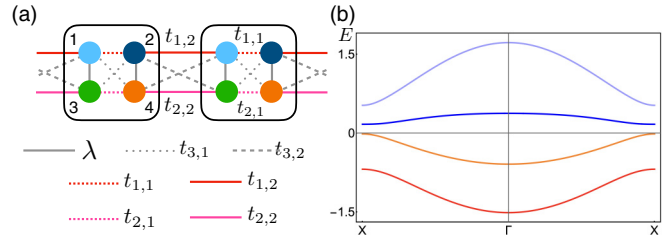

FIG. 9. (a) The hopping pattern of four-band ladder model (B9). Red (pink) dotted line represents the intra-unitcell hopping of the upper (lower) chain, $t_{1,1}(t_{2,1})$. Red (pink) solid line, on the other hand, represents the interunitcell hopping of the upper (lower) chain, $t_{1,2}(t_{2,2})$. Hopping between the two chains $(t_{3,1}, t_{3,2}, \lambda)$ are represented by the gray dotted, solid and dashed lines. (b) Generic band structure of the four-band ladder model (B9). In the plot, we used the arbitrarily-chosen values of the parameters, e.g., $(t_{1,1}, t_{1,2}, t_{2,1}, t_{2,2}, t_{3,1}, t_{3,2}, \lambda) = (1, 0.5, 0.4, 0.2, 0.1, 0.2, 0.2)$. Note that the particle-hole symmetry in the spectrum is absent.

in which $\psi_{\text{final/initial}}(p)$ is the Bloch function of the final and initial bands at the momentum p after/before the scattering, and $\omega_{f,i}$ is the energy transfer required to connect the two states. For example, we can consider the scattering processes like in Fig. 10. Below, we will be interested in the cases, where

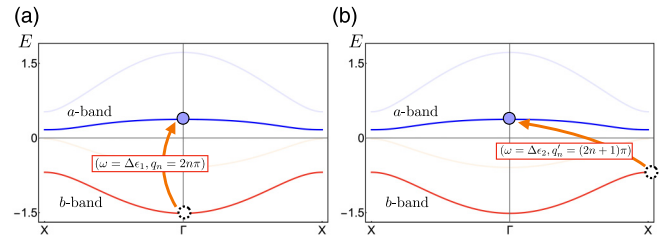

FIG. 10. Our protocol to read off the topological index of the b band from the RIXS intensities. There are two transitions for us to determine the band topology of the b band. (a) the RIXS transition with the energy transfer $\omega_1 = \Delta\epsilon_1 = \epsilon_a(\Gamma) - \epsilon_b(\Gamma)$ and momentum transfer $q_n = 2n\pi$ $(n \in \mathbb{Z})$ (a), which connects Γ point of the b band and Γ point of the a band. (b) Another transition with energy transfer $\omega_2 = \Delta\epsilon_2 = \epsilon_a(\Gamma) - \epsilon_b(X)$, and momentum transfer $q_n' = (2n+1)\pi$ (b), which connects X point of the b band and Γ point of the a band.

k and $k+q$ are both the reflection symmetric. That is, k will be either Γ or X, and $q = 2\pi n+\pi$ or $2\pi n$. These are exactly the processes in Fig. 10.

Given this expression, it is straightforward to show that if the RIXS intensity shows $\cos^2(qd)$-like oscillation, the product of reflection eigenvalues of the initial and final states that participate in the RIXS intensity is 1. That is,

$$I(q) \propto \cos^2(qd) \to \mathcal{R}(k)\mathcal{R}(k+q) = 1. \tag{B15}$$

Similarly,

$$I(q) \propto \sin^2(qd) \to \mathcal{R}(k)\mathcal{R}(k+q) = -1, \tag{B16}$$

because $\{\hat{\mathcal{R}}, \hat{\Pi}_{\text{sub}}\} = 0$. (Remind that k and $k+q$ are both the reflection symmetric.)

The proof for these is the following. For example, for the RIXS intensity with the $\cos^2(qd)$-like oscillations, we see that from Eq. (B14), $(|\psi^\dagger_{\text{final}}(k+q)\psi_{\text{initial}}(k)|, |\psi^\dagger_{\text{final}}(k+q)\hat{\Pi}_{\text{sub}}\psi_{\text{initial}}(k)|) = (1, 0)$. Then,

$$\begin{aligned}\psi^\dagger_{\text{final}}(k+q)\psi_{\text{initial}}(k) &= \psi^\dagger_{\text{final}}(k+q)\hat{\mathcal{R}}^\dagger\hat{\mathcal{R}}\psi_{\text{initial}}(k)\\ &= \mathcal{R}_{\text{final}}(k+q)\mathcal{R}_{\text{initial}}(k)\psi^\dagger_{\text{final}}\\ &\quad\times (k+q)\psi_{\text{initial}}(k) \neq 0.\end{aligned}$$

In the above, we have used the fact that k and $k+q$ are both the reflection symmetric, i.e., X or Γ. Hence, $\psi(k+q)$ and $\psi(k)$ are the eigenvectors of $\hat{\mathcal{R}}$ with the eigenvalues $\mathcal{R}_{\text{final}}(k+q)$ and $\mathcal{R}_{\text{initial}}(k)$. From the above expression, we note that $\mathcal{R}_{\text{final}}(k+q)\mathcal{R}_{\text{initial}}(k)$ is either $+1$ or -1. If it were -1, then $\psi^\dagger_{\text{final}}(k+q)\psi_{\text{initial}}(k)$ would have been zero. Hence, $\mathcal{R}_{\text{final}}(k+q)\mathcal{R}_{\text{initial}}(k)$ should be $+1$. Similarly, one can prove the case of $I(q) \propto \sin^2(qd)$.

Polarization per each filled band

With the above, we can read off the polarization of any filled band from the RIXS intensity via the two types of the momentum transfers, $q_n = 2n\pi$ and $q'_n = (2n+1)\pi$ $(n \in \mathbb{Z})$ (Fig. 10). For example, we will consider the b band in Fig. 10, while keeping the Γ point at the a band as the reference. Essentially, these two transitions will allow us to determine

$$\mathcal{R}_a(\Gamma)\mathcal{R}_b(\Gamma) \tag{B17}$$

from the energy-momentum transfer in Fig. 10(a), and

$$\mathcal{R}_a(\Gamma)\mathcal{R}_b(X) \tag{B18}$$

from the energy-momentum transfer in Fig. 10(b), from their momentum oscillations. With these, we can determine the polarization of the b band via

$$\exp(2\pi i\mathcal{P}_b) = \mathcal{R}_b(\Gamma)\mathcal{R}_b(X) = \mathcal{R}_a(\Gamma)\mathcal{R}_b(\Gamma)\cdot\mathcal{R}_a(\Gamma)\mathcal{R}_b(X), \tag{B19}$$

because $\mathcal{R}_a(\Gamma)^2 = 1$.

As a concrete illustration, we simulate a set of the RIXS intensities with the white noises taken from the uniform distribution, $[-0.1, 0.1] \times |\mathcal{C}(\Delta\epsilon)|^2$ (Fig. 11). As in the previous section, we can obtain RIXS intensity oscillations as a function of momentum transfer. For these, we try to fit the simulated RIXS intensity data into $A\sin^2(Bq_n) + C$, which

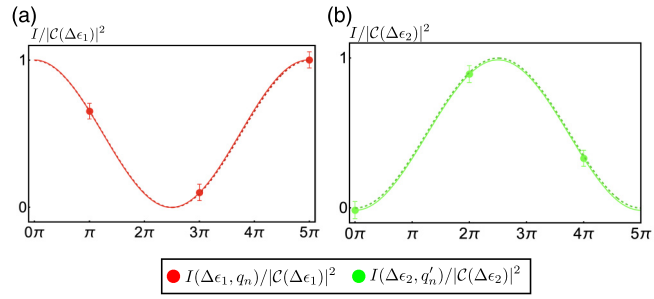

FIG. 11. RIXS intensity oscillation with respect to momentum transfer. Simulated RIXS intensity with noises as a function of $q_n = 2n\pi$ (a) and $q'_n = (2n+1)\pi$ (b) $(n \in \mathbb{Z})$. The simulated random noises taken from uniform distribution $[-0.1, 0.1] \times |\mathcal{C}(\Delta\epsilon_{1,2})|^2$. Dots with error bars show simulated RIXS data with momentum transfer and we try to fit with simulated data (solid lines) where ideal behaviors of RIXS intensity are dashed lines. Since functional forms contain information of $\mathcal{R}_a(\Gamma)\mathcal{R}_b(\Gamma)$ and $\mathcal{R}_a(\Gamma)\mathcal{R}_b(X)$, collecting a product of reflection eigenvalues determines polarization of the b band.

gives

$$\begin{aligned}\mathcal{I}(q_n = 2n\pi, \omega_1 = \Delta\epsilon_1)/|\mathcal{C}(\Delta\epsilon_1)|^2\\ = 1.00\sin^2(0.20q_n) + 0.00,\end{aligned} \tag{B20}$$

for $q_n = 2n\pi$ case with $\Delta\epsilon_1 = \epsilon_a(\Gamma) - \epsilon_b(\Gamma)$. This determines

$$\mathcal{R}_a(\Gamma)\mathcal{R}_b(\Gamma) = -1. \tag{B21}$$

On the other hand, for $q'_n = (2n+1)\pi$ case, we try to fit simulated RIXS intensity data into $A\cos^2(Bq'_n) + C$, which gives

$$\begin{aligned}\mathcal{I}(q'_n = (2n+1)\pi, \omega_2 = \Delta\epsilon_2)/|\mathcal{C}(\Delta\epsilon_2)|^2\\ = 1.01\cos^2(0.20q'_n) + 0.00,\end{aligned} \tag{B22}$$

where $\Delta\epsilon_2 = \epsilon_a(\Gamma) - \epsilon_b(X)$ [Fig. 11(b)]. This determines

$$\mathcal{R}_a(\Gamma)\mathcal{R}_b(X) = +1. \tag{B23}$$

Hence, we find

$$\begin{aligned}\exp(2\pi i\mathcal{P}_b) = \mathcal{R}_b(\Gamma)\mathcal{R}_b(X) = \mathcal{R}_a(\Gamma)\mathcal{R}_b(\Gamma)\\ \cdot\mathcal{R}_a(\Gamma)\mathcal{R}_b(X) = -1,\end{aligned} \tag{B24}$$

which is consistent with the fact that the b-band carries the polarization of $1/2$ mod 1.

Note that the above process can be repeated for the other filled band, and hence we can determine the band topology per each filled band. Next, here we used Γ point of the a-band as the reference, as an illustration. However, one can obviously choose other high-symmetric points in other bands as the reference. Finally, it is straightforward to generalize the above to other band topology and read off the bandwise topology, e.g., 3D topological band insulators, which we explicitly demonstrate in Appendix E.

4. Material candidates of SSH model and DFT calculation

We conduct DFT calculation for searching realistic materials that host SSH model. Specifically, a family of materials

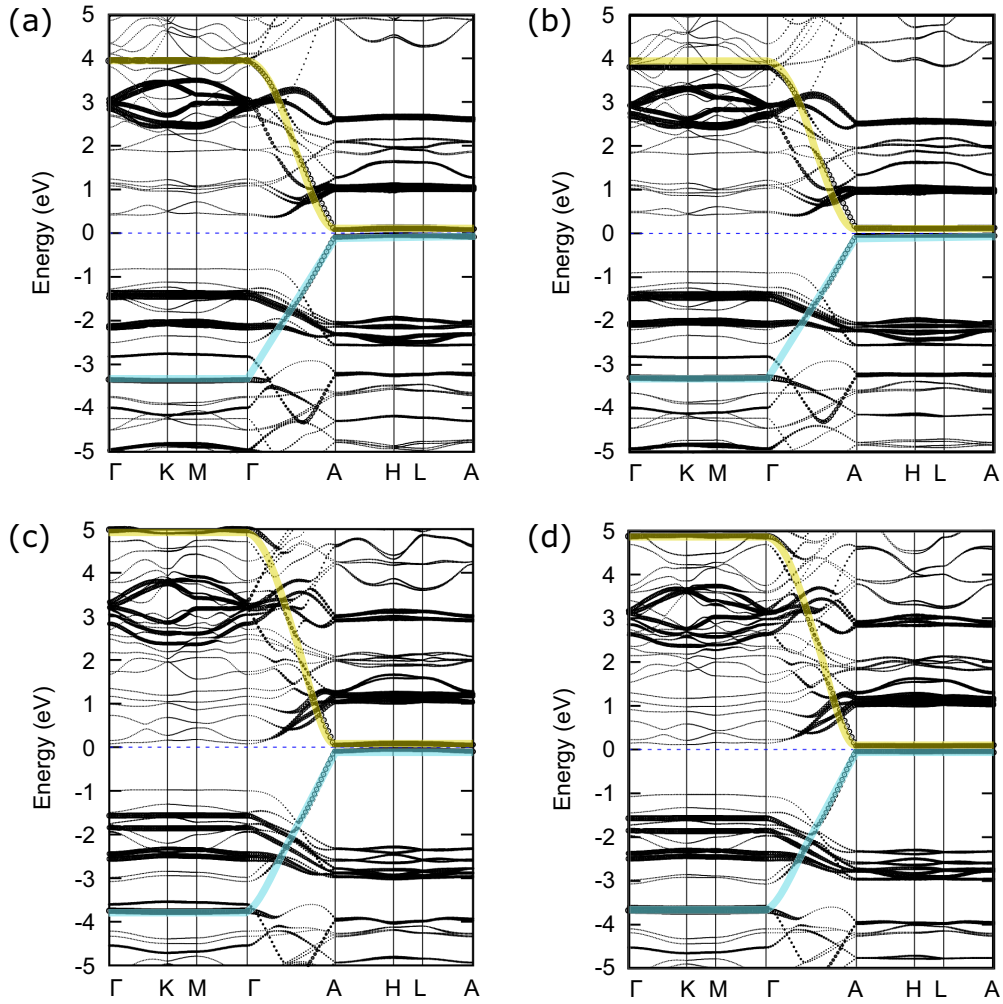

FIG. 12. DFT calculated band structure of (a) $Rb_2Mo_6S_6$, (b) $Cs_2Mo_6S_6$, (c) $Rb_2W_6S_6$, and (d) $Cs_2W_6S_6$. The size of the black circle represents the contribution of M d_{xz}, d_{yz} orbitals. The valence and conduction SSH bands are highlighted by blue and yellow colors, respectively.

with the formula $A_2M_6X_6$, where A = Na, K, Rb, Cs, In, Tl; M = Mo, W; and X = S, Se, Te can be a suitable material candidate. These compounds were experimentally synthesized via the reaction of the corresponding alkali metal tetrathiomolybdates with stoichiometric amounts of M and X. They share the same crystalline structure with the space group $P6_3/m$ (No. 176). The structure features close-packed one-dimensional M_6X_6 wires, consisting of face-sharing M_6 octahedra surrounded by X atoms. The M_6X_6 wires are oriented along the z direction with screw rotation symmetry, arranged in a trigonal lattice in the x-y plane. The A atoms are intercalated in the large holes between the M_6X_6 wires. The $A_2M_6X_6$ structure contains the twofold screw rotation symmetry S_{2z} and the time reversal symmetry T.

Figure 12 shows the calculated band structure of selected molybdenum and tungsten monochalcogenide compounds with dimerization whose unit cell size is 4.3–4.5 Å [33]. Without dimerization, one observes a nodal surface located at the $k_z = \pi$ plane, protected by the antiunitary symmetry TS_{2z}. The nodal surface is very flat due to the weak interwire hopping, and it sits almost exactly at the Fermi level. The spin-orbit coupling (for the valence electrons) is also relatively small, which we estimate to be $\mathcal{O}$(1–10) meV. Such a band structure would be ideal for realizing the SSH model and employing the RIXS experiment.

All the bands near the Fermi level are contributed from the d orbitals of the transition-metal (Mo or W) atoms. Especially, the flat nodal surface states mainly originate from d_{xz} and d_{yz} orbitals of Mo or W. When we allow the dimerization, there are two different M-M bonding distances along the chain axis. Due to the Peierls instability, the dimer formation of lower symmetry is found to be more energetically stable. This dimerization results in a structural deformation $d/a_0 \approx 0.24$. The dimerization also induces a gap at the nodal surface with the gap size of 0.16–0.2 eV. Depending on the unit cell construction, there are two different topologically distinct phases. One can consider the L edges of transition metal Mo (W), i.e., $2p \to 4d$ $(5d)$, the transition metal monochalcogenide compounds $A_2M_6X_6$ can be used to test our theory.

5. Few minor comments

Here we leave a few minor comments on our RIXS intensity formula, which are interesting to note.

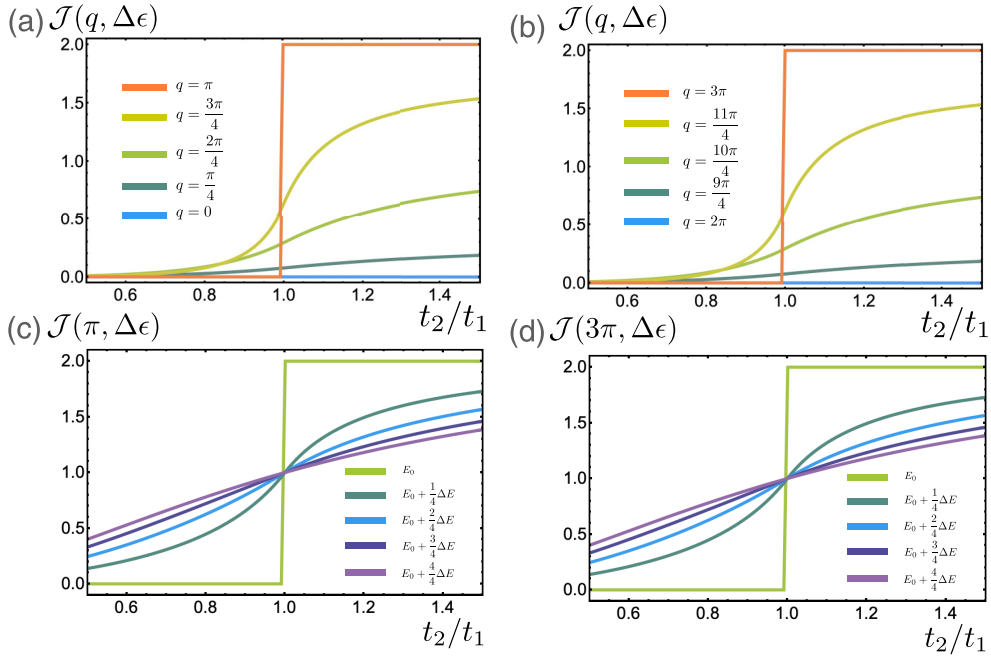

FIG. 13. Nontopological RIXS intensity of the SSH model with different energy and momentum transfer. [(a) and (b)] RIXS intensity with the fixed energy transfer $\Delta\epsilon = \epsilon_c(X) - \epsilon_v(\Gamma)$. Here we have changed the momentum transfers from $q = 0$ to $q = \pi$ (a), from $q = 2\pi$ to $q = 3\pi$ (b). [(c) and (d)] RIXS intensity with the fixed momentum transfer $q = \pi$ (c) and 3π (d), while we tune the energy transfer from $\Delta\epsilon = E_0 = \epsilon_c(X) - \epsilon_v(\Gamma)$ to $\Delta\epsilon = E_0 + \Delta E$. The increment in each step is $\frac{1}{4}\Delta E = \frac{1}{4}[\mathrm{Max}(\epsilon_c(k+\pi) - \epsilon_v(k)) - \mathrm{Min}(\epsilon_c(k+\pi) - \epsilon_v(k))]$.

a. Quantization of "normalized" RIXS intensity

Let us define the normalized RIXS intensity

$$\mathcal{J}(q,\omega) = \frac{\mathcal{I}(q,\omega)}{2|\mathcal{C}(\omega)|^2}, \tag{B25}$$

which essentially factors out the energy dependence from the usual RIXS intensity.

Using this, we can summarize the result of our RIXS intensity formula for the transition:

$$\mathcal{J}(q_n, \Delta\epsilon) = \sin^2(q_n d + \mathcal{P}\pi), \tag{B26}$$

which is entirely fixed by the topology $\mathcal{P}$, but not by the details of the Hamiltonian. For instance, even if one changes the detailed values of the tight-binding parameters, $\mathcal{J}(q_n, \Delta\epsilon)$ remains the same and forms the plateau.

See the orange lines in Figs. 13(a) and 13(b) for the normalized RIXS intensity at $q_n = \pi$ (a) and 3π (b). Here we took $d = 0$. We made this plot by numerically calculating the normalized RIXS intensity as we tune the ratio between the hopping parameters t_2/t_1. For $t_2/t_1 < 1$, the ground state is trivial, i.e., $\mathcal{P} = 0$. For $t_2/t_1 > 1$, the ground state is topological, i.e., $\mathcal{P} = 1/2$. Hence, this explains the steps at $t_2/t_1 = 1$.

Such "quantization" of this normalized RIXS intensity is unique to the particular energy and momentum transfers as depicted in Fig. 13. One can easily guess this from the main text, where the reflection symmetry and its relation to the polarization $\mathcal{P}$ have been essential in deriving our RIXS intensity formula (6) of the main text.

To check this, we numerically calculated the normalized RIXS intensity of different energy and momentum transfers while varying the ratio t_2/t_1. We set $d = 0$ for convenience (here the atomic unitcell size is $a_0 = 1$). We have performed the two following numerical experiments. First, we fix the energy transfer of the RIXS intensity at $\Delta\epsilon = \epsilon_c(X) - \epsilon_v(\Gamma)$ and vary the momentum transfer from $q = 0$ to π [Fig. 13(a)], $q = 2\pi$ to 3π [Fig. 13(b)]. One can clearly note that except the orange lines (which are precisely the channels that we studied in our manuscript), all the others smoothly evolve and thus depend on the details of the band structures. Secondly, we change the energy transfer from $\Delta\epsilon = E_0 = \epsilon_c(X) - \epsilon_v(\Gamma)$ to $\Delta\epsilon = \mathrm{Max}(\epsilon_c(k+\pi) - \epsilon_v(k))$ by $\frac{1}{4}\Delta E = \frac{1}{4}[\mathrm{Max}(\epsilon_c(k+\pi) - \epsilon_v(k)) - \mathrm{Min}(\epsilon_c(k+\pi) - \epsilon_v(k))]$, while we fixed the momentum transfer $q = \pi$ [Fig. 13(c)] and $q = 3\pi$ [Fig. 13(d)]. Again, except the green lines (which are the channels that we studied in our manuscript), every others smoothly evolve and depend on the detailed band structures. These clearly demonstrate that the RIXS intensity at all the other energy and momentum (except the channel in Fig. 13) are nontopological and depend on the details of the band structure.

b. Effect of redefining the unitcell

It is well known that in the SSH chain, the two distinct band topology $\mathcal{P} = 0$ and $\mathcal{P} = 1/2$ can be exchanged by simply redefining the unitcell. That is, if we redefine unit cell by shifting $d \to d - 1/2$, then polarizaiton $\mathcal{P}$ (mod 1) should also be shifted $\mathcal{P} \to \mathcal{P} - 1/2$. Motivated from this, one can ask if our RIXS intensity formula is consistent with this. In fact, it is so because we can rewrite it as

$$\mathcal{I}(q_n, \Delta\epsilon) = 2|\mathcal{C}(\Delta\epsilon)|^2 \sin^2(q_n d + \mathcal{P}\pi) = 2|\mathcal{C}(\Delta\epsilon)|^2 \times \sin^2\left(q_n\left(d - \tfrac{1}{2}\right) + \left(\mathcal{P} - \tfrac{1}{2}\right)\pi\right). \tag{B27}$$

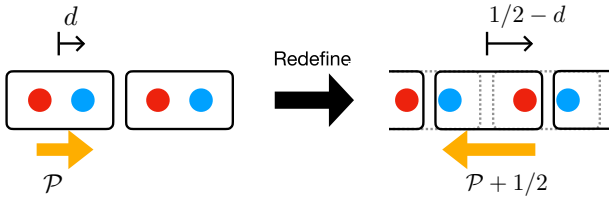

FIG. 14. Unitcell dependence of polarization. If we redefine the unitcell from the left panel to the right one by shifting the center of the unitcell by the half lattice constant $a_0 = 1$, $\mathcal{P}$ should also be shifted by the half. Such covariant transformation gives the exactly-same RIXS intensity.

Hence, the intensity remains the same under the redefinition of unit cells as it should be (because the RIXS intensity is physical, gauge-invariant). See Fig. 14 for an illustration.

c. Effect of spin-flip RIXS on the SSH materials

Here we will show that our conclusion remains the same even when the spin-flip RIXS is included. For example, when one cannot control the polarization of photons, then the spin-flip RIXS may occur simultaneously with the non-spin-flip RIXS. We will use Eq. (A14) [9] to calculate the intensity for the spin-flip RIXS. For example, one possible form of the spin-flip RIXS is

$$\mathcal{I}_{\text{spin-flip}}(q,\omega) = |\mathcal{C}_{\text{spin-flip}}(\omega)|^2 \sum_f{}' |\psi^\dagger_{c,s}(k+q)(\hat{\mathcal{M}}_{k+q,q}\otimes\sigma_0) \times (Id_{2\times 2}\otimes\sigma^\pm_{ss'})\psi_{v,s'}(k)|^2. \tag{B28}$$

Here, we note that $\hat{\mathcal{M}}_{k+q,q}$ is independent of the spin and that $\sigma^\pm_{s,s'}$ signifies the spin-flip process. Because of the spin-flip process, $\psi_{c,s}(k+q)$ and $\psi_{v,s'}(k)$ with $s \neq s'$ appear in the expression. However, the form of the Bloch function is independent of the spin state, this spin-flip RIXS intensity is the same as the non-spin-flip RIXS up to a multiplicative constant. That is,

$$\mathcal{I}_{\text{spin-flip}}(q,\omega) = \text{const.} \times \mathcal{I}_{\text{non-spin-flip}}(q,\omega). \tag{B29}$$

Hence, even with the spin-flip process, we can still use the same formula, i.e., Eq. (6) in our main text, to diagnose the band topology of the SSH materials.

APPENDIX C: 2D QUADRUPOLE INSULATOR

1. Review of quadrupole insulator model

In this Appendix, we will review some basics of the C_4-symmetric quadrupole insulator (QI). In this section, we will temporarily suppress the spin index, which we will recover later when we discuss the RIXS intensity.

Our starting point is the QI Hamiltonian [28],

$$\begin{aligned} H_{QI} = &-\sum_{\boldsymbol{r}\in\mathbb{Z}^2} t_1(c^\dagger_{\boldsymbol{r},1}c_{\boldsymbol{r},3} + c^\dagger_{\boldsymbol{r},2}c_{\boldsymbol{r},4} + c^\dagger_{\boldsymbol{r},1}c_{\boldsymbol{r},4} - c^\dagger_{\boldsymbol{r},2}c_{\boldsymbol{r},3}) + \text{H.c.} \\ &- \sum_{\boldsymbol{r}\in\mathbb{Z}^2} t_2(c^\dagger_{\boldsymbol{r},1}c_{\boldsymbol{r}+\hat{x},3} + c^\dagger_{\boldsymbol{r}+\hat{x},2}c_{\boldsymbol{r},4} + c^\dagger_{\boldsymbol{r},1}c_{\boldsymbol{r}+\hat{y},4} \\ &- c^\dagger_{\boldsymbol{r}+\hat{y},2}c_{\boldsymbol{r},3}) + \text{H.c.}, \end{aligned} \tag{C1}$$

where $c^\dagger_{\boldsymbol{r},\alpha}$ creates an electron at $\mathbf{r}_\alpha = \mathbf{r} + \boldsymbol{d}_\alpha$ with

$$\mathbf{r_1} = \mathbf{r} + (d,d), \quad \mathbf{r_2} = \mathbf{r} + (-d,-d), \quad \mathbf{r_3} = \mathbf{r} + (-d,d), \quad \mathbf{r_4} = \mathbf{r} + (d,-d). \tag{C2}$$

and $t_1(t_2)$ is an intra(inter)site hopping parameter. We move to the momentum space by performing Fourier transformation, $c_{\boldsymbol{r},\alpha} = \sum_{k,\alpha} c_{\boldsymbol{k},\alpha}e^{i\boldsymbol{k}\cdot\boldsymbol{r}}$

$$H_{QI} = \sum_{\mathbf{k}} \mathbf{c}^\dagger_{\mathbf{k}} h_{QI}(\mathbf{k})\mathbf{c}_{\mathbf{k}}, \tag{C3}$$

with

$$h_{QI}(\boldsymbol{k}) = \begin{pmatrix} 0 & 0 & (t_1+t_2e^{ik_x}) & (t_1+t_2e^{ik_y}) \\ 0 & 0 & -(t_1+t_2e^{-ik_y}) & (t_1+t_2e^{-ik_x}) \\ (t_1+t_2e^{-ik_x}) & -(t_1+t_2e^{ik_y}) & 0 & 0 \\ (t_1+t_2e^{-ik_y}) & (t_1+t_2e^{ik_x}) & 0 & 0 \end{pmatrix} \tag{C4}$$

and $\mathbf{c}^T_{\mathbf{k}} = (c_{\mathbf{k},1}, c_{\mathbf{k},2}, c_{\mathbf{k},3}, c_{\mathbf{k},4})$.

By diagonalizing the Hamiltonian, we finally find

$$H_{QI} = \sum_{k,\eta=c,v,\xi=1,2} \varepsilon_{\xi,\eta}(k)\gamma^\dagger_{\xi,\eta}(k)\gamma_{\xi,\eta}(k),$$
$$\varepsilon_{\xi=1,2,\eta=c,v}(k) = \pm\sqrt{2t_1^2 + 2t_2^2 + 2t_1t_2(\cos k_x + \cos k_y)}. \tag{C5}$$

2. Symmetry

There are two symmetries of the insulator, which we will often use: C_4 rotation symmetry and chiral symmetry. (In the QI, we assume that there are perturbations to the Hamiltonian, which break the chiral symmetry explicitly. Hence, although we discuss the chiral symmetry operator here, we do not impose it to the Hamiltonian.)

First, the C_4 rotation symmetry is given by the matrix $\hat{\mathcal{C}}_4$

$$\hat{\mathcal{C}}_4 \doteq \begin{pmatrix} 0 & \sigma_0 \\ -i\sigma_2 & 0 \end{pmatrix}. \tag{C6}$$

When the symmetry is applied to the fermion field, we find

$$C_4 : \boldsymbol{c}_k \to \hat{\mathcal{C}}_4 \cdot \boldsymbol{c}_{r_4[k]} = \begin{pmatrix} 0 & \sigma_0 \\ -i\sigma_2 & 0 \end{pmatrix} \cdot \boldsymbol{c}_{r_4[k]}, \tag{C7}$$

where $r_4 : (k_x, k_y) \to (-k_y, k_x)$.

Secondly, the chiral symmetry is given by the matrix

$$\hat{\Pi} \doteq \sigma_3 \otimes \sigma_0 = \begin{pmatrix} 1 & 0 & 0 & 0 \\ 0 & 1 & 0 & 0 \\ 0 & 0 & -1 & 0 \\ 0 & 0 & 0 & -1 \end{pmatrix}. \tag{C8}$$

When the chiral symmetry is applied to the fermion field, we find

$$\Pi : \boldsymbol{c}_k \to \hat{\Pi} \cdot \boldsymbol{c}_k = (\sigma_3 \otimes \sigma_0) \cdot \boldsymbol{c}_k. \tag{C9}$$

3. Topology

We present the C_4 rotation eigenvalues which are useful to calculate the RIXS intensity formula. See Table I of the main text. The quadrupole moment, $\mathcal{Q}_{xy}$ of the insulator, satisfies the relation Eq. (C10) [28]:

$$\exp\left(2\pi i \mathcal{Q}_{xy}\right) = r^{\xi}_{4,\eta}(\Gamma)^* r^{\xi}_{4,\eta}(M) = r^{\xi}_{4,\eta}(\Gamma)^* r^{\xi}_{4,\eta}(M). \tag{C10}$$

Here ($\xi = \pm$) is the index for the degenerate states at the high-symmetry points Γ and M, which can be resolved by the C_4 eigenvalues.

APPENDIX D: 2D C_4 SYMMETRIC HIGHER ORDER TOPOLOGICAL INSULATOR

1. Review of 2D C_4 symmetric higher order topological insulator

In this Appendix, we investigate another C_4 symmetric insulator $H^{(4)}_{1b}$ [48]. As in the quadrupolar insulator, we will suppress the spin index for the clarity. We will restore it back when we calculate the RIXS intensity. The real-space Hamiltonian is

$$\begin{aligned} H^{(4)}_{1b} = &- \sum_{\boldsymbol{r}\in\mathbb{Z}^2} t_1 (c^\dagger_{\boldsymbol{r},1} c_{\mathbf{r},3} + c^\dagger_{\mathbf{r},2} c_{\mathbf{r},4} + c^\dagger_{\mathbf{r},1} c_{\mathbf{r},4} + c^\dagger_{\mathbf{r},2} c_{\mathbf{r},3}) + \text{H.c.} \\ &- \sum_{\mathbf{r}\in\mathbb{Z}^2} t_2 (c^\dagger_{\mathbf{r},1} c_{\mathbf{r}+\mathbf{e}_x,3} + c^\dagger_{\mathbf{r}+\mathbf{e}_x,2} c_{\mathbf{r},4} + c^\dagger_{\mathbf{r},1} c_{\mathbf{r}+\mathbf{e}_y,4} \\ &\quad + c^\dagger_{\boldsymbol{r}+\boldsymbol{e}_y,2} c_{\mathbf{r},3}) + \text{H.c.}, \end{aligned} \tag{D1}$$

where $c^\dagger_{\boldsymbol{r},\alpha}$ creates an electron at $\boldsymbol{r}_{\boldsymbol{\alpha}}$ with

$$\begin{aligned} \boldsymbol{r_1} &= \boldsymbol{r} + (d, d), \quad \boldsymbol{r_2} = \boldsymbol{r} + (-d, -d), \\ \boldsymbol{r_3} &= \boldsymbol{r} + (-d, d), \quad \boldsymbol{r_4} = \boldsymbol{r} + (d, -d), \end{aligned} \tag{D2}$$

where $\boldsymbol{r} \in \mathbb{Z}^2$. See Fig. 5(a) for the real-space hopping patterns of $H^{(4)}_{1b}$.

By performing Fourier transformation, $c_{\boldsymbol{r},\alpha} = \sum_{k,\alpha} c_{\boldsymbol{k},\alpha} e^{i\boldsymbol{k}\cdot\boldsymbol{r}}$, the Hamiltonian is

$$H^{(4)}_{4b} = \sum_{\mathbf{k}} c^\dagger_{\mathbf{k}} h^{(4)}_{1b}(\mathbf{k}) c_{\mathbf{k}}, \tag{D3}$$

where

$$h^{(4)}_{1b}(\mathbf{k}) = -\begin{pmatrix} 0 & 0 & t_1 + t_2 e^{ik_x} & t_1 + t_2 e^{ik_y} \\ 0 & 0 & t_1 + t_2 e^{-ik_y} & t_1 + t_2 e^{-ik_x} \\ t_1 + t_2 e^{-ik_x} & t_1 + t_2 e^{ik_y} & 0 & 0 \\ t_1 + t_2 e^{-ik_y} & t_1 + t_2 e^{ik_x} & 0 & 0 \end{pmatrix}. \tag{D4}$$

We diagonalize the Hamiltonian via

$$H^{(1)}_{4b} = \sum_{\mathbf{k}, i=c/v,\ \eta=1,2} \epsilon_{i,\eta}(\mathbf{k}) \gamma^\dagger_{i,\eta}(\mathbf{k}) \gamma_{i=c/v,\eta}(\mathbf{k}), \tag{D5}$$

$$\epsilon_{i=c/v,1}(\mathbf{k}) = \pm\sqrt{t_1^2 + t_2^2 + t_1 t_2 (\cos k_x + \cos k_y) + \sqrt{\left(t_1^2 + t_2^2 + 2t_1 t_2 \cos k_x\right)\left(t_1^2 + t_2^2 + 2t_1 t_2 \cos k_y\right)}}, \tag{D6}$$

$$\epsilon_{i=c/v,2}(\mathbf{k}) = \pm\sqrt{t_1^2 + t_2^2 + t_1 t_2 (\cos k_x + \cos k_y) - \sqrt{\left(t_1^2 + t_2^2 + 2t_1 t_2 \cos k_x\right)\left(t_1^2 + t_2^2 + 2t_1 t_2 \cos k_y\right)}}, \tag{D7}$$

with the corresponding four eigenstates, $\psi_{i=c/v,\eta=1}(\mathbf{k})$ and $\psi_{i=c/v,\eta=2}(\mathbf{k})$, respectively. See Fig. 5(b) for the band dispersions of $H^{(4)}_{1b}$.

2. Symmetry

There are three symmetries in $H^{(4)}_{1b}$: C_4 rotation symmetry, and two mirror symmetries, and chiral symmetry. Although we discuss the mirror and chiral symmetries here, we do not impose them to be respected by the Hamiltonian, when we come to calculate the RIXS intensity. That is, we will assume that there are always small perturbations which break the symmetries explicitly.

First, let us discuss the C_4 rotation symmetry, which involves the matrix $\hat{\mathcal{C}}_4$. When it acts on the fermion,

$$C_4 : \boldsymbol{c}_k \to \hat{\mathcal{C}}_4 \cdot \boldsymbol{c}_{r_4[\boldsymbol{k}]} = \begin{pmatrix} 0 & \sigma_0 \\ \sigma_1 & 0 \end{pmatrix} \cdot \boldsymbol{c}_{r_4[\boldsymbol{k}]}, \tag{D8}$$

where $r_4 : (k_x, k_y) \to (-k_y, k_x)$.

Similarly, the $M_{x,y}$ mirror symmetries are given by the corresponding matrices $\hat{M}_{x,y}$ where x, y represents the mirror planes.

$$M_x : \boldsymbol{c}_k \to \hat{M}_x \cdot \boldsymbol{c}_{m_x[\boldsymbol{k}]} = \begin{pmatrix} 0 & \sigma_0 \\ \sigma_0 & 0 \end{pmatrix} \cdot \boldsymbol{c}_{m_x[\boldsymbol{k}]}, \tag{D9}$$

$$M_y : \boldsymbol{c}_k \to \hat{M}_y \cdot \boldsymbol{c}_{m_y[\boldsymbol{k}]} = \begin{pmatrix} 0 & \sigma_1 \\ \sigma_1 & 0 \end{pmatrix} \cdot \boldsymbol{c}_{m_y[\boldsymbol{k}]}, \tag{D10}$$

TABLE III. C_4 eigenvalue tables at high-symmetry points. We summarize rotation eigenvalues of $(c/v, 1)$ bands which is relevant band in the quarter filling. See the band dispersion [Fig. 5(b)]. When $|t_1| > |t_2|$, $\mathcal{C} = 0$ which is the trivial phase. When $|t_1| < |t_2|$, $\mathcal{C} = 1/2$, and $H_{1b}^{(4)}$, Eq. (D4) is in the topological phase.

C_4	$\Gamma(\boldsymbol{q} = (0,0))$	$M(\boldsymbol{q} = (\pi,\pi))$
v	$\text{sign}(t_1 + t_2)$	$\text{sign}(t_1 + t_2)\, e^{2\pi i \mathcal{C}}$
c	$-\text{sign}(t_1 + t_2)$	$-\text{sign}(t_1 + t_2)\, e^{2\pi i \mathcal{C}}$

where $m_x : (k_x, k_y) \to (-k_x, k_y)$, $m_y : (k_x, k_y) \to (k_x, -k_y)$. Lastly, the chiral symmetry is represented by $\Pi \doteq \sigma^3 \otimes \sigma^0$.

3. Topology

For Hamiltonian (D4), we summarize the C_4 rotation eigenvalues in Table III, which are useful in the next section. These eigenvalues determine $\mathcal{C}$, which is either 0 (trivial) or $1/2$ (topological).

APPENDIX E: 3D TOPOLOGICAL BAND INSULATOR

1. Review of 3D TBI

Here we will review the basics of the 3D topological band insulator (TBI) in a diamond lattice (see Ref. [30] for the details), which is consisted of two interpenetrating face-centered cubic lattices (FCC) with a displacement $\vec{d} = \frac{1}{8}(1,1,1)$. The tight-binding Hamiltonian is

$$H_{\text{TBI}} = t \sum_{\langle i,j \rangle} c_i^\dagger c_j + 8i\lambda_{\text{SO}} \sum_{\langle\langle i,j \rangle\rangle} c_i^\dagger \boldsymbol{s} \cdot \left(\boldsymbol{d}_{ij}^1 \times \boldsymbol{d}_{ij}^2\right) c_j + \text{H.c.}, \tag{E1}$$

where t is a hopping parameter and $\boldsymbol{d}_{ij}^{1,2}$ are the two nearest-neighbor bond vectors traverse between i and j. Here, λ_{SO} is the spin-orbit coupling strength. Under strain [111] direction, the hopping parameter along [111] direction t is changed by $t \to t + \delta t$ [30]. Incorporating this and performing the Fourier transformation, $\boldsymbol{c_r} = \sum_{\boldsymbol{k}} \boldsymbol{c_k} e^{i\boldsymbol{k}\cdot\boldsymbol{r}}$, we find

$$H_{\text{TBI}} = \sum_{\boldsymbol{k}} \boldsymbol{c}_{\boldsymbol{k}}^\dagger h_{\text{TBI}}(\boldsymbol{k}) \boldsymbol{c_k}, \tag{E2}$$

where $\boldsymbol{c_k} = (c_{\boldsymbol{k},1,\uparrow}, c_{\boldsymbol{k},1,\downarrow}, c_{\boldsymbol{k},2,\uparrow}, c_{\boldsymbol{k},2,\downarrow})$,

$$h_{\text{TBI}}(\boldsymbol{k}) = \sum_{a=1}^{5} d_a(\boldsymbol{k}) \Gamma^a, \tag{E3}$$

and

$$\begin{aligned}
x_1 &= \tfrac{1}{2}(k_y + k_z), \quad x_2 = \tfrac{1}{2}(k_x + k_z), \quad x_3 = \tfrac{1}{2}(k_y + k_x),\\
d_1(k) &= t + \delta t + t(\cos x_1 + \cos x_2 + \cos x_3),\\
d_2(k) &= t(\sin x_1 + \sin x_2 + \sin x_3),\\
d_3(k) &= \lambda_{\text{SO}}(\sin x_2 - \sin x_3 - \sin(x_2 - x_1) + \sin(x_3 - x_1)),\\
d_4(k) &= \lambda_{\text{SO}}(\sin x_3 - \sin x_1 - \sin(x_3 - x_2) + \sin(x_1 - x_2)),\\
d_5(k) &= \lambda_{\text{SO}}(\sin x_1 - \sin x_2 - \sin(x_1 - x_3) + \sin(x_2 - x_3)),\\
\Gamma^{a=1,2,3,4,5} &= (\tau^1\sigma^0, \tau^2\sigma^0, \tau^3\sigma^1, \tau^3\sigma^2, \tau^3\sigma^3),
\end{aligned}$$

and δt is the change of the hopping parameter along the [111] direction.

2. Symmetry and topology

The Hamiltonian $h_{\text{TBI}}(\boldsymbol{k})$ has the two crucial symmetries. The first is the inversion symmetry

$$\mathcal{I} : \boldsymbol{c}_k \to \hat{\mathcal{I}} \cdot \boldsymbol{c}_{-k} = \tau_1\sigma_0 \cdot \boldsymbol{c}_{-k}. \tag{E4}$$

The second symmetry is the (antiunitary) time-reversal symmetry

$$\mathcal{T} : \boldsymbol{c}_k \to \hat{\mathcal{T}} \cdot \boldsymbol{c}_{-k} = (i\tau_0\sigma_2)K \cdot \boldsymbol{c}_{-k}, \tag{E5}$$

where K is a complex conjugate operator.

The phase diagram of H_{TBI} is simple:

$$\delta t > 0 : \text{topological} \quad \delta t < 0 : \text{trivial}, \tag{E6}$$

where the $\mathbb{Z}_2$ topological band index can be calculated as [30,46]

$$(-1)^\nu = \Pi_{\boldsymbol{k}_* \in \text{TRIM}} \mathcal{I}_v(\boldsymbol{k}_*) = \Pi_{\boldsymbol{k}_* \in \text{TRIM} - \{\Gamma\}} \mathcal{I}_v(\Gamma) \mathcal{I}_v(\boldsymbol{k}_*), \tag{E7}$$

where the time-reversal invariant momentum (TRIM) points are given as

$$\begin{aligned}
&\Gamma(0,0,0), X_1(2\pi,0,0), X_2(0,2\pi,0), X_3(0,0,2\pi),\\
&\times L_1(\pi,\pi,\pi), L_2(\pi,-\pi,-\pi), L_3(-\pi,\pi,-\pi),\\
&\times L_4(-\pi,-\pi,\pi),
\end{aligned} \tag{E8}$$

and $\mathcal{I}_v(\boldsymbol{k}_* \in \text{TRIM}) = \pm 1$ is an inversion eigenvalue of the valence bands at the TRIM points. In the second equality of Eq. (E7), we have used $\mathcal{I}_v(\Gamma)^8 = 1$.

Let us present the inversion eigenvalues for a given value of the δt. When $\delta t > 0$ (topological), the eigenvalues are

$\boldsymbol{k}_*$	Γ	X_1	X_2	X_3	L_1	L_2	L_3	L_4
$\mathcal{I}_v(\boldsymbol{k}_*)$	-1	-1	-1	-1	1	-1	-1	-1

(E9)

which gives $(-1)^7 = (-1)^\nu$, i.e., $\nu = 1 \bmod 2$. On the other hand, when $\delta t < 0$ (trivial),

$\boldsymbol{k}_*$	Γ	X_1	X_2	X_3	L_1	L_2	L_3	L_4
$\mathcal{I}_v(\boldsymbol{k}_*)$	-1	1	1	1	1	-1	-1	-1

(E10)

which gives $(-1)^4 = (-1)^\nu$, i.e., $\nu = 0 \bmod 2$.

3. Another demonstration

In this section, we demonstrate how the RIXS data can be used to read off topological band index. Suppose a series of RIXS intensity that connects Γ and other TRIM points (X, L_1, L_2) by $\boldsymbol{q}_{i=1,2,3}$ is obtained. For example,

$$I_{\Gamma\to X(2\pi,0,0)}(\boldsymbol{q_1}, \Delta\epsilon_1) = |\mathcal{C}(\Delta\epsilon_1)|^2 \sum_\mu |\psi^\dagger_{c,\mu}(X)\hat{\mathcal{M}}_{\boldsymbol{q_1}}\psi_{v,\mu}(\Gamma)|^2 \propto \sin^2(\boldsymbol{q_1}\cdot\boldsymbol{d}), \tag{E11}$$

$$I_{\Gamma\to L_1(\pi,\pi,\pi)}(\boldsymbol{q_2}, \Delta\epsilon_2) = |\mathcal{C}(\Delta\epsilon_2)|^2 \sum_\mu |\psi^\dagger_{c,\mu}(L_1)\hat{\mathcal{M}}_{\boldsymbol{q_2}}\psi_{v,\mu}(\Gamma)|^2 \propto \cos^2(\boldsymbol{q_2}\cdot\boldsymbol{d}), \tag{E12}$$

$$I_{\Gamma\to L_2(\pi,-\pi,\pi)}(\boldsymbol{q_3}, \Delta\epsilon_3) = |\mathcal{C}(\Delta\epsilon_3)|^2 \sum_\mu |\psi^\dagger_{c,\mu}(L_2)\hat{\mathcal{M}}_{\boldsymbol{q_3}}\psi_{v,\mu}(\Gamma)|^2 \propto \sin^2(\boldsymbol{q_3}\cdot\boldsymbol{d}). \tag{E13}$$

From these results, we can reconstruct the inversion eigenvalues at $\boldsymbol{k} \in$ TRIM, see Table (E14).

$\mathbf{k}$	Γ	X_1	X_2	X_3	L_1	L_2	L_3	L_4
$\mathcal{I}_v(\boldsymbol{k})$	$\mathcal{I}_v(\Gamma)$	$\mathcal{I}_v(\Gamma)$	$\mathcal{I}_v(\Gamma)$	$\mathcal{I}_v(\Gamma)$	$-\mathcal{I}_v(\Gamma)$	$\mathcal{I}_v(\Gamma)$	$\mathcal{I}_v(\Gamma)$	$\mathcal{I}_v(\Gamma)$

(E14)

From the eigenvalues, we can also infer the $\mathbb{Z}_2$ topological index, i.e.,

$$(-1)^\nu = -(\mathcal{I}_v(\Gamma))^8 = -1 \quad \Rightarrow \nu \equiv 1 \bmod 2. \tag{E15}$$

This actually corresponds to $\delta t > 0$ case of $h_{\mathrm{TBI}}(\boldsymbol{k})$.

Note that the above protocol can be generalized to nonminimal models. For example, as a concrete illustration, we will consider the double copies of Eq. (E3) with different Hamiltonian parameters.

$$h_{\mathrm{TBI},8}(\boldsymbol{k}) = \begin{pmatrix} h_{\mathrm{TBI}}(t_1, \delta t_1, \lambda_{SO,1}; \boldsymbol{k}) + e_1\mathbb{I}_{4\times4} & e_3\mathbb{I}_{4\times4} \\ e_3\mathbb{I}_{4\times4} & h_{\mathrm{TBI}}(t_2, \delta t_2, \lambda_{SO,2}; \boldsymbol{k}) + e_2\mathbb{I}_{4\times4} \end{pmatrix}, \tag{E16}$$

Here, $h_{\mathrm{TBI}}(t_i, \delta t_i, \lambda_{SO,i}; \boldsymbol{k})$ $(i = 1, 2)$ is one of two copies of bloch Hamiltonian (E3) with a parameter set $(t_i, \delta t_i, \lambda_{SO,i})$ and $e_{a=1,2}\mathbb{I}_{4\times4}$ is for the constant energy shifts for each bands. Here, e_3 is the hybridizations between the two copies. The band dispersion of $h_{\mathrm{TBI},8}(\boldsymbol{k})$ is plotted in Fig. 15.

We note that this model shares the same structure factor $\hat{\mathcal{M}}_{\boldsymbol{q}}$ as before. That is, $\hat{\mathcal{M}}_{\boldsymbol{q},8} = \hat{\mathcal{M}}_{\boldsymbol{q}} \oplus \hat{\mathcal{M}}_{\boldsymbol{q}}$. We can explicitly write the RIXS intensity and quantum amplitudes out in terms of the Bloch functions:

$$\begin{aligned} \mathcal{A}^{\mu,\nu}_{i\to f}(\boldsymbol{q}_n, \Delta\epsilon) &= \mathcal{C}(\Delta\epsilon)\psi^\dagger_{f,\mu}(\boldsymbol{k}+\boldsymbol{q_n})\hat{\mathcal{M}}_{\boldsymbol{q}_n,8}\psi_{i,\nu}(\boldsymbol{k}), \\ &= \mathcal{C}(\Delta\epsilon)(\cos(\boldsymbol{q}_n\cdot\boldsymbol{d})\psi^\dagger_{f,\mu}(\boldsymbol{k}+\boldsymbol{q_n})\psi_{i,\nu}(\boldsymbol{k}) + i\sin(\boldsymbol{q}_n\cdot\boldsymbol{d})\psi^\dagger_{f,\mu}(\boldsymbol{k}+\boldsymbol{q_n})\hat{\Pi}_8\psi_{i,\nu}(\boldsymbol{k})), \end{aligned} \tag{E17}$$

where μ and ν are degeneracy indices for each bands. Finally, the inversion symmetry is $\hat{\mathcal{I}}_8 = \Gamma^1 \oplus \Gamma^1$, which implies that $\{\hat{\mathcal{I}}_8, \hat{\Pi}_8\} = 0$ still holds. Since all the algebra straightforwardly follows even in this case, we can easily show that

$$I(\boldsymbol{q}_n, \Delta\epsilon) = \begin{cases} 2|\mathcal{C}(\Delta\epsilon)|^2 \sin^2 \boldsymbol{q}_n\cdot\boldsymbol{d} & \text{for } \mathcal{I}_f(\boldsymbol{k}+\boldsymbol{q}_n)\mathcal{I}_i(\boldsymbol{k}) = 1, \\ 2|\mathcal{C}(\Delta\epsilon)|^2 \cos^2 \boldsymbol{q}_n\cdot\boldsymbol{d} & \text{for } \mathcal{I}_f(\boldsymbol{k}+\boldsymbol{q}_n)\mathcal{I}_i(\boldsymbol{k}) = -1, \end{cases} \tag{E18}$$

for $\boldsymbol{q}_n$ that connects TRIM points $\boldsymbol{k}$ and $\boldsymbol{k}+\boldsymbol{q}_n$. For example, $\boldsymbol{q}_n = 2\pi(n+1, n, n)$ as the momentum connecting Γ to X.

Below, we will work with the parameters,

$$(t_1, t_2, \delta t_1, \delta t_2, \lambda_{SO,1}, \lambda_{SO,2}, e_1, e_2, e_3) = (0.5, 0.6, -0.2, 0.25, 0.3, 0.3, 0.12, -0.15, 0.12),$$

which are arbitrarily chosen. We will label each twofold degenerate bands as in Fig. 15 and summarize their inversion eigenvalues at TRIM points in Table (E19).

$\mathbf{k}$	Γ	X_1	X_2	X_3	L_1	L_2	L_3	L_4
$\mathcal{I}_1(\boldsymbol{k})$	1	−1	−1	−1	−1	1	1	1
$\mathcal{I}_2(\boldsymbol{k})$	1	1	1	1	−1	1	1	1
$\mathcal{I}_3(\boldsymbol{k})$	−1	1	1	1	1	−1	−1	−1
$\mathcal{I}_4(\boldsymbol{k})$	−1	−1	−1	−1	1	−1	−1	−1

(E19)

Next, we demonstrate our protocol to read off the product of the inversion eigenvalues from the momentum oscillation of the RIXS intensity. From this, we will determine the topological $\mathbb{Z}_2$ band index at the end. As a concrete illustration, we will take the state at X of the 2-band as the reference and will attempt to read off the band topology of the 3-band. For this, we consider the two example transitions: (a) $\psi_{3,\mu}(\Gamma) \to \psi_{2,\mu}(X)$, which we can choose degeneracy index μ as before, by momentum transfer $\boldsymbol{q}_n = 2\pi(n+1, n, n)$ $(n \in \mathbb{Z})$ and (b) $\psi_{3,\mu}(X) \to \psi_{2,\mu}(X)$ by momentum transfer $\boldsymbol{q}'_n = 2\pi(n, n, n)$ [with $n \in \mathbb{Z}$, see Figs. 16(a) and 16(b)].

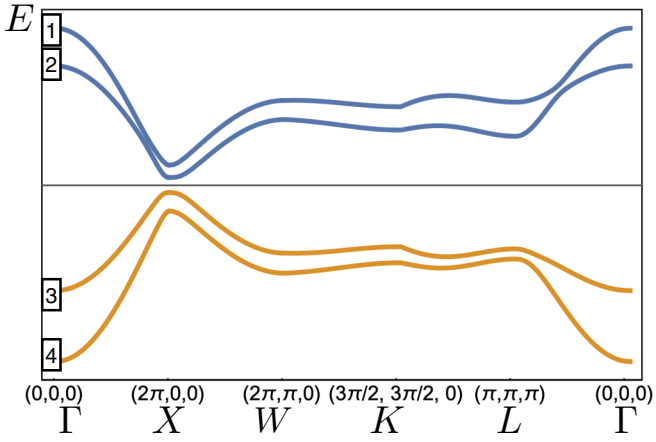

FIG. 15. The band dispersion of $h_{\mathrm{TBI},8}(\boldsymbol{k})$ with $(t_1, t_2, \delta t_1, \delta t_2, \lambda_{SO,1}, \lambda_{SO,2}, e_1, e_2, e_3)$=(0.5, 0.6, −0.2, 0.25, 0.3, 0.3, 0.12, −0.15, 0.12) along the high-symmetry cuts in the Brillouin zone.

We have numerically simulated those two RIXS transitions with noises taken from a random uniform distribution, $[-0.2, 0.2] \times |\mathcal{C}(\Delta\epsilon)|^2$ to mimic experimental situation. With the data, we try to fit $\mathcal{I}(\boldsymbol{q}_n)/|\mathcal{C}(\Delta\epsilon)|^2 = A\sin^2(\boldsymbol{q}_n \cdot \boldsymbol{d} + B) + C$ [cf. Eq. (18)] for (a). As before, B is the diagnostics of the band topology, $B = \frac{1}{4}(\mathcal{I}_3(\Gamma)\mathcal{I}_2(X) + 1)\pi$, where $\mathcal{I}_a(\boldsymbol{k})$ is an inversion eigenvalue of the a band at $\boldsymbol{k}$.

For the ideal limit of (a), clean signal of $\mathcal{I}_3(\Gamma)\mathcal{I}_2(X) = -1$ case (without the noise), we expect to find

$$A = 2.00,\ B = 0.00,\ \text{and}\ C = 0.00, \tag{E20}$$

which is the dotted red line in Fig. 17(a). As the result of the fitting (the solid red line in Fig. 17(a)], we found

$$A = 1.99,\ B = 0.01,\ \text{and}\ C = 0.00, \tag{E21}$$

which agrees well with ideal result. In particular, from B, we can correctly infer $\mathcal{I}_3(\Gamma)\mathcal{I}_2(X) = 4B/\pi - 1 \approx -1$.

For the ideal limit of (b), ideal signal of $\mathcal{I}_3(X)\mathcal{I}_2(X) = 1$ case (without the noise), we expect to find

$$A = 2.00,\ B = 1.58,\ \text{and}\ C = 0.00, \tag{E22}$$

which is the dotted green line in Fig. 16(b). As the result of the fitting [the solid green line in Fig. 16(b)], we found

$$A = 2.00,\ B = 1.58,\ \text{and}\ C = 0.00, \tag{E23}$$

which also agrees with ideal case. In particular, from $B \approx \pi/2$, we can correctly infer $\mathcal{I}_3(X)\mathcal{I}_2(X) \approx 1$.

This can be repeated for all the TRIM points of the 3-band, which allows us to determine $\mathcal{I}_3(X)\mathcal{I}_2(\mathbf{k}_*)$ with $\boldsymbol{k}_* \in$ TRIM. Then, we can determine the band-wise $\mathbb{Z}_2$ invariant ν_0(3-band) of the 3-band via

$$(-1)^{\nu_0(\text{3-band})} = \prod_{\boldsymbol{k}_* \in \text{TRIM}} \mathcal{I}_3(\boldsymbol{k}_*) = \prod_{\boldsymbol{k}_* \in \text{TRIM}} [\mathcal{I}_3(\boldsymbol{k}_*)\mathcal{I}_2(X)], \tag{E24}$$

since $\mathcal{I}_2(X)^8 = 1$. There are two remarks. The same can be repeated for the other filled band, i.e., 4-band, to completely determine the $\mathbb{Z}_2$ invariant. Next, in the above, we have selected the X point of the 2-band as the reference, but (if there is any preference) one can choose other high-symmetry point with other band as the reference.

APPENDIX F: 3D CHIRAL HINGE INSULATOR

1. Review of 3D chiral hinge insulator

Here, we will review the basics of 3D chiral hinge insulator (CHI) by following Ref. [31]. Its momentum-space Hamiltonian is

$$H_{\mathrm{CHI}} = \sum_{\boldsymbol{k}} \psi^\dagger(\boldsymbol{k}) h_{\mathrm{CHI}}(\boldsymbol{k}) \psi(\boldsymbol{k}),$$

$$h_{\mathrm{CHI}}(\boldsymbol{k}) = \left(M + t\sum_i \cos k_i\right)\tau_1\sigma_0 + \Delta_1 \sum_{i=x,y,z} \sin k_i \tau_3\sigma_i + \Delta_2(\cos k_x - \cos k_y)\tau_2\sigma_0, \tag{F1}$$

where $\psi^T(\boldsymbol{k}) = (c_{\alpha=0,\uparrow}(\boldsymbol{k}), c_{\alpha=0,\downarrow}(\boldsymbol{k}), c_{\alpha=1,\uparrow}(\boldsymbol{k}), c_{\alpha=1,\downarrow}(\boldsymbol{k}))$. Here, Δ_2 term is a C_4^z-symmetry-breaking term by external effect such as $[1\bar{1}0]$ strain. $\alpha = 0, 1$ is a sublattice index and $s = \uparrow, \downarrow$ is the spin index. Also $\boldsymbol{r}_\alpha = \boldsymbol{r} + (-1)^\alpha \boldsymbol{d} = \boldsymbol{r} - (-1)^\alpha(0, 0, d/2)$ with $\boldsymbol{r} \in \mathbb{Z}^3$ and $0 < d < \frac{1}{2}$ without loss of generality. Each eigenstates are twofold degenerate protected

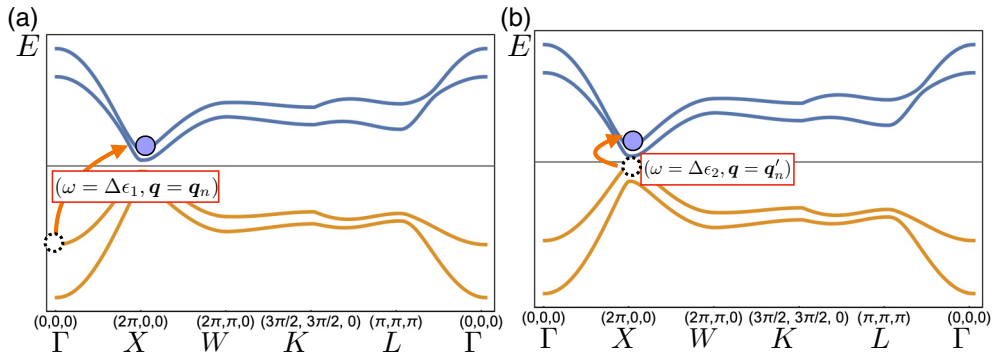

FIG. 16. The two RIXS transitions with appropriate energy-momentum transfers that we consider. (a) With energy-momentum transfer $(\Delta\epsilon_1 = \epsilon_2(X) - \epsilon_3(\Gamma), \boldsymbol{q}_n = 2\pi(n+1, n, n))$ $(n \in \mathbb{Z})$, this RIXS intensity is determined by the inversion eigenvalues $\mathcal{I}_2(X)$ and $\mathcal{I}_3(\Gamma)$. See Eq. (E18). (b) With energy-momentum transfer $(\Delta\epsilon_2 = \epsilon_2(X) - \epsilon_3(X), \boldsymbol{q}'_n = 2\pi(n, n, n))$ $(n \in \mathbb{Z})$, the RIXS intensity of this transition is determined by the $\mathcal{I}_2(X)$ and $\mathcal{I}_3(X)$. See Eq. (E18).

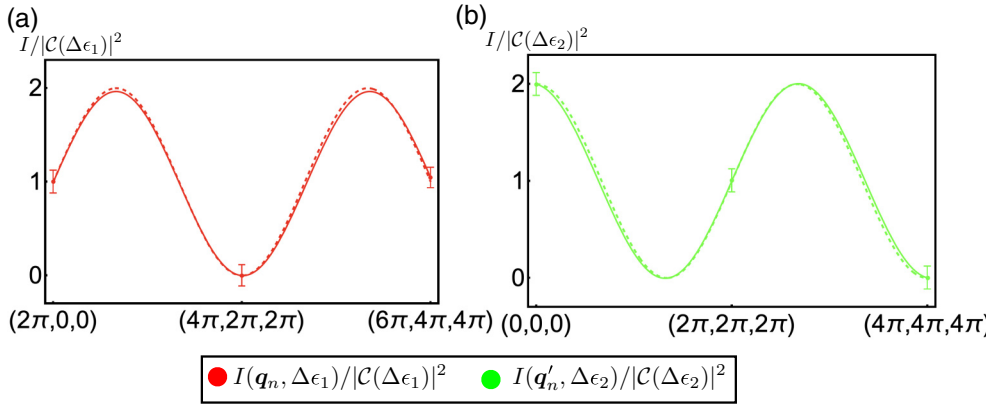

FIG. 17. The two RIXS intensities of $h_{\mathrm{TBI},8}(\boldsymbol{k})$ with appropriate energy and momentum transfers. Red (a) and green (b) dotted lines represent ideal results without noises and red (a) and green (b) solid lines are the result of the fitting from simulated data. For detailed procedure, see from Eqs. (E20) to (E23).

by the symmetries of the system, which we will explain in the next section.

2. Symmetry and topology

The remaining symmetries of the CHI Hamiltonian are $\hat{I}\hat{T}$ and $\hat{C}_4^z\hat{I}$. Each are represented as

$$\hat{C}_4^z = \tau_0 e^{-i\frac{\pi}{4}\sigma_z}, \quad \hat{I} = \tau_1\sigma_0, \quad \hat{T} = \tau_0\sigma_y K, \tag{F2}$$

when acting on the fermion fields. Here, $\hat{I}$ is an inversion operator and $\hat{T}$ is time-reversal operator with the complex conjugation operator K. They satisfy

$$\left(\hat{C}_4^z\hat{T}\right)^4 = -1, \quad \left(\hat{C}_4^z\hat{I}\right)^4 = -1, \quad \left[\hat{C}_4^z\hat{I}, \hat{I}\hat{T}\right] = 0,$$
$$\left\{\hat{C}_4^z\hat{I}, \hat{\Pi}\right\} = 0, \tag{F3}$$

where $\hat{\Pi} = \tau_3\sigma_0$ is a chiral-symmetry operator. As in the other models, we will in general assume that the chiral symmetry is explicitly broken by perturbations to the CHI Hamiltonian.

The topology of the CHI Hamiltoinan can be expressed as the inversion eigenvalues of some high-symmetry points in momentum space, namely, the rotoinversion symmetric points (RISP) such that $(C_4^z I)\boldsymbol{k} = \boldsymbol{k}$:

$$\mathrm{RISP} = \{(0,0,0), (0,0,\pi), (\pi,\pi,0), (\pi,\pi,\pi)\}. \tag{F4}$$

Note that because of Eq. (F3), $\hat{C}_4^z\hat{I}$ eigenvalues of the twofold degenerate eigenstates at RISP has to be complex conjugate pairs, $\{\mathcal{I}_v(\boldsymbol{k})e^{i\pi/4}, \mathcal{I}_v(\boldsymbol{k})e^{-i\pi/4}\}$ with $\mathcal{I}_v(\boldsymbol{k}) = \pm 1$ is an inversion eigenvalue of the band at $\boldsymbol{k}$.

The topological band index is given by the modified Fu-Kane formula [31]

$$(-1)^{\nu} = \Pi_{\boldsymbol{k}\in\mathrm{RISP}}\mathcal{I}_v(\boldsymbol{k}) = \Pi_{\boldsymbol{k}\in\mathrm{RISP}\text{-}\{\Gamma\}}\mathcal{I}_v(\boldsymbol{k})\mathcal{I}_v(\Gamma). \tag{F5}$$

Here $\mathcal{I}_v(\boldsymbol{k})$ is an inversion eigenvalue of *one* of the two filled band at $\boldsymbol{k}$. In the second equality, we used $\mathcal{I}_v^4(\Gamma) = 1$. When Δ_2 is finite, H_{CHI} becomes topological and hosts a chiral hinge state for $1 < |M/t| < 3$. Otherwise, it is trivial.

[1] L. J. P. Ament, M. van Veenendaal, T. P. Devereaux, J. P. Hill, and J. van den Brink, Resonant inelastic x-ray scattering studies of elementary excitations, Rev. Mod. Phys. **83**, 705 (2011).

[2] A. Kotani and S. Shin, Resonant inelastic x-ray scattering spectra for electrons in solids, Rev. Mod. Phys. **73**, 203 (2001).

[3] A. Rusydi, A. Goos, S. Binder, A. Eich, K. Botril, P. Abbamonte, X. Yu, M. B. H. Breese, H. Eisaki, Y. Fujimaki, S. Uchida, N. Guerassimova, R. Treusch, J. Feldhaus, R. Reininger, M. V. Klein, and M. Rübhausen, Electronic Screening-Enhanced Hole Pairing in Two-Leg Spin Ladders Studied by High-Resolution Resonant Inelastic X-Ray Scattering at Cu *M* Edges, Phys. Rev. Lett. **113**, 067001 (2014).

[4] P. Abbamonte, C. A. Burns, E. D. Isaacs, P. M. Platzman, L. L. Miller, S. W. Cheong, and M. V. Klein, Resonant Inelastic X-Ray Scattering from Valence Excitations in Insulating Copper Oxides, Phys. Rev. Lett. **83**, 860 (1999).

[5] B. J. Kim, H. Ohsumi, T. Komesu, S. Sakai, T. Morita, H. Takagi, and T. Arima, Phase-sensitive observation of a spin-orbital mott state in Sr_2IrO_4, Science **323**, 1329 (2009).

[6] B. J. Kim and G. Khaliullin, Resonant inelastic x-ray scattering operators for t_{2g} orbital systems, Phys. Rev. B **96**, 085108 (2017).

[7] J. Kim, M. Daghofer, A. H. Said, T. Gog, J. van den Brink, G. Khaliullin, and B. J. Kim, Excitonic quasiparticles in a spin–Orbit mott insulator, Nat. Commun. **5**, 4453 (2014).

[8] A. Revelli, M. Moretti Sala, G. Monaco, P. Becker, L. Bohatý, M. Hermanns, T. C. Koethe, T. Fröhlich, P. Warzanowski, T. Lorenz, S. V. Streltsov, P. H. M. van Loosdrecht, D. I. Khomskii, J. van den Brink, and M. Grüninger, Resonant inelastic x-ray incarnation of Young's double-slit experiment, Sci. Adv. **5**, eaav4020(2019).

[9] L. Savary and T. Senthil, Probing hidden orders with resonant inelastic x-ray scattering, arXiv:1506.04752.

[10] G. B. Halász, S. Kourtis, J. Knolle, and N. B. Perkins, Observing spin fractionalization in the Kitaev spin liquid via temperature evolution of indirect resonant inelastic x-ray scattering, Phys. Rev. B **99**, 184417 (2019).

[11] P. Marra, J. van den Brink, and S. Sykora, Theoretical approach to resonant inelastic x-ray scattering in iron-based superconductors at the energy scale of the superconducting gap, Sci. Rep. **6**, 25386 (2016).

[12] S. Kourtis, Bulk spectroscopic measurement of the topological charge of Weyl nodes with resonant x rays, Phys. Rev. B **94**, 125132 (2016).

[13] M. Z. Hasan and C. L. Kane, Colloquium: Topological insulators, Rev. Mod. Phys. **82**, 3045 (2010).

[14] X.-L. Qi and S.-C. Zhang, Topological insulators and superconductors, Rev. Mod. Phys. **83**, 1057 (2011).

[15] C.-K. Chiu, J. C. Y. Teo, A. P. Schnyder, and S. Ryu, Classification of topological quantum matter with symmetries, Rev. Mod. Phys. **88**, 035005 (2016).

[16] Y. L. Chen, J. G. Analytis, J.-H. Chu, Z. K. Liu, S.-K. Mo, X. L. Qi, H. J. Zhang, D. H. Lu, X. Dai, Z. Fang, S. C. Zhang, I. R. Fisher, Z. Hussain, and Z.-X. Shen, Experimental realization of a three-dimensional topological insulator, Bi_2Te_3, Science **325**, 178 (2009).

[17] Y. Xia, D. Qian, D. Hsieh, L. Wray, A. Pal, H. Lin, A. Bansil, D. Grauer, Y. S. Hor, R. J. Cava, and M. Z. Hasan, Observation of a large-gap topological-insulator class with a single Dirac cone on the surface, Nat. Phys. **5**, 398 (2009).

[18] D. Hsieh, Y. Xia, L. Wray, D. Qian, A. Pal, J. H. Dil, J. Osterwalder, F. Meier, G. Bihlmayer, C. L. Kane, Y. S. Hor, R. J. Cava, and M. Z. Hasan, Observation of unconventional quantum spin textures in topological insulators, Science **323**, 919 (2009).

[19] A. Nishide, A. A. Taskin, Y. Takeichi, T. Okuda, A. Kakizaki, T. Hirahara, K. Nakatsuji, F. Komori, Y. Ando, and I. Matsuda, Direct mapping of the spin-filtered surface bands of a three-dimensional quantum spin Hall insulator, Phys. Rev. B **81**, 041309(R) (2010).

[20] P. Roushan, J. Seo, C. V. Parker, Y. S. Hor, D. Hsieh, D. Qian, A. Richardella, M. Z. Hasan, R. J. Cava, and A. Yazdani, Topological surface states protected from backscattering by chiral spin texture, Nature (London) **460**, 1106 (2009).

[21] J. Seo, P. Roushan, H. Beidenkopf, Y. S. Hor, R. J. Cava, and A. Yazdani, Transmission of topological surface states through surface barriers, Nature (London) **466**, 343 (2010).

[22] H. Beidenkopf, P. Roushan, J. Seo, L. Gorman, I. Drozdov, Y. S. Hor, R. J. Cava, and A. Yazdani, Spatial fluctuations of helical Dirac fermions on the surface of topological insulators, Nat. Phys. **7**, 939 (2011).

[23] Z. Alpichshev, J. G. Analytis, J.-H. Chu, I. R. Fisher, Y. L. Chen, Z. X. Shen, A. Fang, and A. Kapitulnik, STM Imaging of Electronic Waves on the Surface of Bi_2Te_3: Topologically Protected Surface States and Hexagonal Warping Effects, Phys. Rev. Lett. **104**, 016401 (2010).

[24] S. Nadj-Perge, I. K. Drozdov, J. Li, H. Chen, S. Jeon, J. Seo, A. H. MacDonald, B. A. Bernevig, and A. Yazdani, Observation of Majorana fermions in ferromagnetic atomic chains on a superconductor, Science **346**, 602 (2014).

[25] M. Ruby, F. Pientka, Y. Peng, F. von Oppen, B. W. Heinrich, and K. J. Franke, End States and Subgap Structure in Proximity-Coupled Chains of Magnetic Adatoms, Phys. Rev. Lett. **115**, 197204 (2015).

[26] B. Jäck, Y. Xie, J. Li, S. Jeon, B. A. Bernevig, and A. Yazdani, Observation of a Majorana zero mode in a topologically protected edge channel, Science **364**, 1255 (2019).

[27] W. A. Benalcazar, B. A. Bernevig, and T. L. Hughes, Quantized electric multipole insulators, Science **357**, 61 (2017).

[28] W. A. Benalcazar, B. A. Bernevig, and T. L. Hughes, Electric multipole moments, topological multipole moment pumping, and chiral hinge states in crystalline insulators, Phys. Rev. B **96**, 245115 (2017).

[29] C. Fang, M. J. Gilbert, and B. A. Bernevig, Bulk topological invariants in noninteracting point group symmetric insulators, Phys. Rev. B **86**, 115112 (2012).

[30] L. Fu and C. L. Kane, Topological insulators with inversion symmetry, Phys. Rev. B **76**, 045302 (2007).

[31] F. Schindler, A. M. Cook, M. G. Vergniory, Z. Wang, S. S. P. Parkin, B. A. Bernevig, and T. Neupert, Higher order topological insulators, Sci. Adv. **4**, eaat0346 (2018).

[32] W. P. Su, J. R. Schrieffer, and A. J. Heeger, Solitons in Polyacetylene, Phys. Rev. Lett. **42**, 1698 (1979).

[33] K.-H. Jin and F. Liu, 1D topological phases in transition-metal monochalcogenide nanowires, Nanoscale **12**, 14661 (2020).

[34] M. Potel, R. Chevrel, M. Sergent, J. C. Armici, M. Decroux, and Ø. Fischer, New pseudo-one-dimensional metals: $M_2Mo_6Se_6 (M = \mathrm{Na, In, K, Tl})$, $M_2Mo_6S_6 (M = \mathrm{K, Rb, Cs})$, $M_2Mo_6Te_6 (M = \mathrm{In, Tl})$, J. Solid State Chem. **35**, 286 (1980).

[35] J. M. Tarascon, G. W. Hull, and F. J. DiSalvo, A facile synthesis of pseudo one-monodimensional ternary molybdenum chalcogenides $M_2Mo_6X_6 (X = \mathrm{Se, Te; M = Li, Na..Cs})$, Mater. Res. Bull. **19**, 915 (1984).

[36] P. H. Hor, W. C. Fan, L. S. Chou, R. L. Meng, C. W. Chu, J. M. Tarascon, and M. K. Wu, Study of the metal-semiconductor transition in $Rb_2Mo_6Se_6$, $Rb_2Mo_6Te_6$and$Cs_2Mo_6Te_6$ under pressures, Solid State Commun. **55**, 231 (1985).

[37] D. Hsieh, D. Qian, L. Wray, Y. Xia, Y. S. Hor, R. J. Cava, and M. Z. Hasan, A topological Dirac insulator in a quantum spin Hall phase, Nature (London) **452**, 970 (2008).

[38] A. A. Taskin and Y. Ando, Quantum oscillations in a topological insulator $Bi_{1-x}Sb_x$, Phys. Rev. B **80**, 085303 (2009).

[39] B. J. Wieder, Z. Wang, J. Cano, X. Dai, L. M. Schoop, B. Bradlyn, and B. A. Bernevig, Strong and fragile topological Dirac semimetals with higher-order Fermi arcs, Nat. Commun. **11**, 627 (2020).

[40] L. J. P. Ament, G. Khaliullin, and J. van den Brink, Theory of resonant inelastic x-ray scattering in iridium oxide compounds: Probing spin-orbit-entangled ground states and excitations, Phys. Rev. B **84**, 020403(R) (2011).

[41] L. J. P. Ament, F. Forte, and J. van den Brink, Ultrashort lifetime expansion for indirect resonant inelastic x-ray scattering, Phys. Rev. B **75**, 115118 (2007).

[42] M. W. Haverkort, Theory of Resonant Inelastic X-Ray Scattering by Collective Magnetic Excitations, Phys. Rev. Lett. **105**, 167404 (2010).

[43] D. Benjamin, I. Klich, and E. Demler, Single-Band Model of Resonant Inelastic X-Ray Scattering by Quasiparticles in High-T_c Cuprate Superconductors, Phys. Rev. Lett. **112**, 247002 (2014).

[44] R. D. King-Smith and D. Vanderbilt, Theory of polarization of crystalline solids, Phys. Rev. B **47**, 1651 (1993).

[45] R. Resta, Quantum-Mechanical Position Operator in Extended Systems, Phys. Rev. Lett. **80**, 1800 (1998).

[46] L. Fu, C. L. Kane, and E. J. Mele, Topological Insulators in Three Dimensions, Phys. Rev. Lett. **98**, 106803 (2007).

[47] M. Park, J. S. Choi, L. Yang, and H. Lee, Raman spectra shift of few-layer IV-VI 2D materials, Sci. Rep. **9**, 19826 (2019).

[48] W. A. Benalcazar, T. Li, and T. L. Hughes, Quantization of fractional corner charge in C_n-symmetric higher order topological crystalline insulators, Phys. Rev. B **99**, 245151 (2019).

[49] B. Bradlyn, L Elcoro, J. Cano, M. G. Vergniory, Z. Wang, C. Felser, M. I. Aroyo, and B. A. Bernevig, Topological quantum chemistry, Nature (London) **547**, 298 (2017).

[50] A. Kitaev, Periodic table for topological insulators and superconductors, AIP Conf. Proc. **1134**, 22 (2009).

[51] J. Kruthoff, J. de Boer, J. van Wezel, C. L. Kane, and R.-J. Slager, Topological Classification of Crystalline Insulators through Band Structure Combinatorics, Phys. Rev. X **7**, 041069 (2017).

[52] Z. Wang, B. J. Wieder, J. Li, B. Yan, and B. A. Bernevig, Higher-Order Topology, Monopole Nodal Lines, and the Origin of Large Fermi Arcs in Transition Metal Dichalcogenides XTe_2(X = Mo, W), Phys. Rev. Lett. **123**, 186401 (2019).

[53] Y.-B. Choi, Y. Xie, C.-Z. Chen, J. Park, S.-B. Song, J. Yoon, B. J. Kim, T. Taniguchi, K. Watanabe, J. Kim, K. C. Fong, M. N. Ali, K. T. Law, and G.-H. Lee, Evidence of higher-order topology in multilayer WTe_2 from Josephson coupling through anisotropic hinge states, Nat. Mater. **19**, 974 (2020).

[54] K. O. H. B. Hedman and J. E. Penner-Hahn, *In EXAFS and Near Edge Structurexs III* (Springer, 1984), Vol. 2.

[55] M. O. Krause and J. H. Oliver, Natural widths of atomic K and L levels, K X-ray lines and several KLL Auger lines, J. Phys. Chem. Ref. Data **8**, 329 (1979).

[56] N. Pakhira, J. K. Freericks, and A. M. Shvaika, Resonant inelastic x-ray scattering in a Mott insulator, Phys. Rev. B **86**, 125103 (2012).

[57] K. Gilmore, J. Pelliciari, Y. Huang, J. J. Kas, M. Dantz, V. N. Strocov, S. Kasahara, Y. Matsuda, T. Das, T. Shibauchi, and T. Schmitt, Description of Resonant Inelastic X-Ray Scattering in Correlated Metals, Phys. Rev. X **11**, 031013 (2021).